UNIVERSITY OF CALIFORNIA
IRVINE

Unstable Liquid-Liquid Dispersed Flows in Industrial Installations

DISSERTATION

Submitted in partial fulfillment of the requirements for the degree of

DOCTOR OF PHILOSOPHY

in Mechanical and Aerospace Engineering

by

Tsolag Apelian

Dissertation Committee:
Professor Derek Dunn-Rankin, Chair
Professor William A. Sirignano
Professor Said E. Elghobashi

2011

ProQuest LLC
789 East Eisenhower Parkway
P.O. Box 1346
Ann Arbor, MI 48106-1346

To my dear parents, of whom I am very proud.

"Trust in the LORD with all thine heart;

and lean not unto thine own understanding.

In all thy ways acknowledge Him,

and He shall direct thy paths."

Proverbs 3:5-6 *KJV*

ACKNOWLEDGEMENTS

Thanks to Siemens Power Corp. for supporting the Siemens Emulsion Generation and Characterization project financially, without which this dissertation could not completed. Many thanks to all my labmates at the Lasers, Flames and Aerosols Laboratory at UC Irvine, they have been an excellent company throughout the years. I am grateful to professor W.A. Sirignano for his supervision and guidance through the Siemens Emulsion Generation and Characterization project and beyond. I am also indebted to professor S. Elghobashi for the fruitful discussions and ideas he shared with me along the way. And finally, my full gratitude goes to my advisor, professor Derek Dunn-Rankin for being a source of inspiration and motivation as well as providing the scientific and technical insight without which this work would not have been possible.

TABLE OF CONTENTS

LIST OF FIGURES

Figure

LIST OF TABLES

Table

LIST OF APPENDICES

Appendix

LIST OF SYMBOLS

Greek Symbols

β	Contact angle between material and liquid
$\Delta\rho$	Difference between densities
δ_{ij}	The Kronecker delta function
ϵ_{ij}	Strain rate tensor
η_k	Kolmogoroff microscale
$\dot{\gamma}$	Shear strain rate
μ	Dynamic viscosity
Φ	Number of phases in thermodynamic equilibrium
ϕ	Volumetric ratio of the subscript to the total volume, no subscript indicates volumetric ratio of the dispersed phase to the total volume.
ϕ^{max}	Volumetric fraction of the maximum packing limit of undeformed spheres.
ρ	Density
σ	Interfacial tension
τ	Shear stress

τ_{ij} Stress tensor

θ Angle between pipe and the horizontal

υ Area viscosity

ξ Shear viscosity

ζ_1 Relaxation time (Equation 3.12c)

ζ_2 Retardation time (Equation 3.12d)

Roman Symbols

$\hat{k}$ Consistency index

$\hat{n}$ Flow behavior index

$\hat{t}$ Collision time constant

$\mathbf{g}$ Local gravitational acceleration

$\mathbb{C}$ Number of components in a thermodynamic system

$\mathbb{F}$ Number of thermodynamic degrees of freedom

$\mathbb{N}$ Number of non-compositional variables in a thermodynamic system

a Coefficient of the general form of the Blasius Equation (Equation 3.26)

B Defined in Equation 3.14b

b Exponent of the general form of the Blasius Equation (Equation 3.26)

Bo Bond number

Ca Capillary number

D Pipe diameter

d Droplet diameter

F Darcy-Weisbach friction factor

f Fanning friction factor

k_2 Shape factor of collision doublets

$K_{1,2and3}$ Various coefficients, see Equation 3.7

M Defined in Equation 3.15c

N Defined in Equation 3.15e

Oh Ohnesorge number

P Defined in Equation 3.15d

p Pressure

Q Volumetric flow rate

q Hydrodynamic interaction constant

r Radial position

r droplet radius

Re Reynolds number

We Weber number

Subscripts

′ Modified value for two phase flow

0 Limit of low shear rate

32 Sauter mean diameter

c	Continuous phase
d	Dispersed phase
m	Mixture
r	Relative (dispersed to continuous phase)
w	Water
Gen	Generalized
i	Intrinsic.

LIST OF ABBREVIATIONS

PDMS PolyDiMethylSiloxane

W/F Water-in-Fuel

W/O Water-in-Oil

O/W Oil-in-Water

Surfactants Surface Active Agents

CCD Charge Coupled Device

PVM Particle Vision Microscope

ABSTRACT OF THE DISSERTATION

Unstable Liquid-Liquid Dispersed Flows
in Industrial Installations

By

Tsolag Apelian

Doctor of Philosophy in Mechanical and Aerospace Engineering

University of California, Irvine, 2011

Professor Derek Dunn-Rankin, Chair

The flow of two immiscible liquids where one liquid forms a homogeneous dispersion of fine droplets in a continuous phase of the other, is studied under the conditions of an industrial installation. The pressure drop behavior of the dispersions is studied in straight, horizontal tube sections, and through a safety screen (a filter-like fitting) in a housing case. It is found that Water-in-Oil dispersions have a Newtonian behavior under laminar conditions with transition to turbulence taking place at higher Reynolds numbers for higher dispersed phase ratios. Oil-in-Water flows are found behave in a non-Newtonian way in both laminar and turbulent regimes, with transition properties qualitatively similar to Water-in-Oil dispersions. Pressure drop measurements across the safety screen housing, with no safety screen, showed that the loss coefficient is constant and independent of the dispersion type or level of turbulence. However, with the safety screen in place, laminar regime flows have loss coefficients that increase with the increasing concentration of the more viscous liquid, without depending on any other factors; while the loss coefficient remained constant for fully turbulent flows. A technique was developed to obtain instantaneous images of the fine droplets of the dispersion in the near-wall area. This technique helped determine the cause of the non-Newtonian behavior more likely to be the dynamic breakup and

coalescence of droplets rather than droplet deformation.

CHAPTER I

Motivation and Scope

Liquid-liquid flows are found in a wide range of engineering applications. In food, agriculture, paint, pharmaceutical, cosmetics and various chemical industries they appear in the form of emulsions. In petroleum production, wells usually yield complex mixtures of organic oils and an aqueous phase, which comes from naturally occurring sources or due to water pumped down the well to boost production. In petroleum transportation, adding water to high viscosity petroleum oils being pumped in pipes can reduce pumping losses dramatically (*Joseph and Renardy*, 1993). Despite the vast fields of application where liquid-liquid flows are present they are not fully understood, and many questions regarding their formation and flow remain unanswered. This is mostly due to the numerous factors that go into determining those flows, resulting in complex systems that are difficult not only to analyze and model but also to measure and characterize.

The general motivation of this dissertation is to contribute to a better understanding of a particular class of liquid-liquid flows, namely those in the fully dispersed regime that are not stabilized by surfactants, and on which buoyancy has a negligible effect. As will be shown in Chapter III flow resistance of liquid-liquid unstable flows is highly dependent on system parameters. Also the measurement of droplet size distribution in unstable liquid-liquid dispersed flows of practical importance has been a particularly challenging task, accomplished only at simplified conditions, which in most cases render the outcome of

little practical value.

The particular motivation for the present work comes from a combustion system. Water is added to the combustion process of diesel, kerosene or heavy fuel oils to curb emissions, in particular NO_x and soot (*Park et al.*, 2001; *Lif and Holmberg*, 2006). The NO_x reduction comes from lowering peak combustion temperatures, and possible modifications in kinetic pathways and other chemical effects, such as providing an abundance of OH^- radicals. Another benefit of adding water might take place under conditions when the fuel and water mixture undergoes a phenomenon known as microexplosions (*Law et al.*, 1980; *Mattiello et al.*, 1992; *Wang and Chen*, 1996; *Mizutani et al.*, 2001; *Fu et al.*, 2002; *Lif and Holmberg*, 2006; *Kadota et al.*, 2007; *Jeong et al.*, 2008) that causes secondary atomization and enhances the mixing of fuel and air. The microexplosion phenomenon is usually described as the disintegration of an atomized emulsion droplet when the aqueous phase reaches boiling temperature faster than the oil phase and thus 'explodes', shattering the droplet into smaller parts. The addition of water to the combustion process can be accomplished in several ways. Direct separate injection, and co-injection have been applied to reciprocating engines (*Tajima et al.*, 2001), while water injection at the compressor inlet has been used in gas turbines (*Chaker et al.*, 2004). Water can also be mixed with the fuel stream before the latter is injected into the combustion chamber; this method avoids the risk associated with generating thermal stresses at points of water injection, and does not affect the volumetric efficiency of the compressor. Moreover, when the mixture forms a well-dispersed emulsion it can enhance chances of microexplosions to occur and can inherently ensure better mixing and introduction of water into the combustion process when compared to direct or co-injection.

To be able to study the spraying and atomization in a system where water is mixed with fuel before injection, it is necessary to understand the mixing process and to characterize the mixture adequately. It has been shown that the properties of the atomized mist in this case will depend on the characteristics of the mixture before atomization (*Kufferath et al.*,

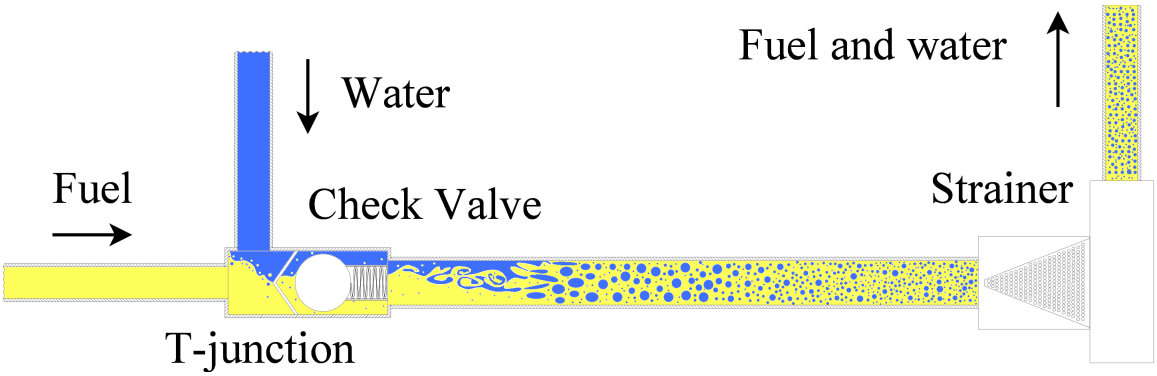

Figure 1.1: A simple layout for typical fuel-water supply lines in gas turbines.

1999; *Bolszo et al.*, 2009).

Therefore, the first objective of this work is to characterize the unstable (Water-in-Fuel (W/F)) emulsion that forms in the pipelines of a typical gas turbine fuel delivery system, from the point of mixing of the two liquids until the atomizers. A schematic diagram of such a system is shown in Figure 1.1, it consists of a T-type junction that introduces water to the fuel line; this junction is usually equipped with a check valve, after which the mixture passes through a mesh strainer before being distributed to the atomizers. The characterization will include the effects of mixing through the T-junction and passing through the strainer. The effect of change in pipe diameter as the mixture is being distributed to the atomizers is outside the scope of this work but based on the shear rates expected in modest pipe size change junctions, the major emulsification effects are likely to be in the T-junction and strainer. Once this mixture is properly characterized, it will help determine the properties of the atomized mist. The second objective follows from the first, and constitutes improving the understanding of the factors that affect the properties and behavior of unstable liquid-liquid dispersed flows in horizontal pipes, by expanding and properly generalizing the findings from the first objective. The results also shed light on the analyses currently found in the literature in order to improve and expand them.

This dissertation is organized as follows: The next chapter will include a brief introduction to the basics of liquid-liquid flows and direct the focus to fully dispersed liquid-liquid

flows. The subsequent chapter will demonstrate the state of the literature on unstable fully dispersed liquid-liuqid flows and summarize the missing parts of the formed picture. The next chapter will describe the experimental setup of the system used in this work and relevant calibration and adjustment issues. Results will be shown and discussed in the chapter after and conclusions will appear in the final chapter.

CHAPTER II

Introduction

2.1 Introduction

2.1.1 Nomenclature and Definitions

When two or more mutually insoluble (immiscible) liquids travel together in the same conduit, the flow is called a liquid-liquid flow. The common literature reference to liquid-liquid flows as "multiphase flows" should be interpreted with caution. Thermodynamically, two immiscible liquids are two distinct phases according to the Gibbs Phase Rule [1]. A "phase" according to the Merriam-Webster dictionary is "*a homogeneous, physically distinct, and (often) mechanically separable portion of matter present in a non-homogeneous macroscopic physicochemical system*", and according to the Cambridge dictionary of science and technology "*the sum of all those portions of a material system which are identical in chemical composition and physical state, and are separated from the rest of the system by a distinct interface called the* `phase boundary`". Therefore, there is no doubt that two immiscible liquids in the same conduit can be considered as separate phases, linguistically. However, in a more specific notion, "phase" refers to the internal molecular (or atomic) structure of system constituents. In this sense, the three common states of matter are differ-

[1] According to the Gibbs Phase Rule, the total number of phases in thermodynamic equilibrium, Φ, is given by $\mathbb{F} = \mathbb{C} + \mathbb{N} - \Phi$
where $\mathbb{F}$ is the number of thermodynamic degrees of freedom, $\mathbb{C}$ is the number of components and $\mathbb{N}$ is the number of non-compositional variables. For incompressible systems $\mathbb{N} = 1$.

ent phases with respect to each other, also different solids can form different phases if their molecular structures (lattices) are different. But different liquids, regardless of their miscibility, cannot be different phases because their molecular structures are similar, despite their immiscibility. To make this point clear, this dissertation uses the expression "liquid-liquid flows" as a general reference, but for convenience, it follows the literature convention in referring to the constituent liquids as phases.

The spatial structure of liquid-liquid flows can assume a variety of different configurations due to the deformable boundaries between the immiscible liquids. These different configurations are known as flow patterns or regimes. The two extremes of flow patterns are the fully separated/segregated pattern, and the fully dispersed pattern. Separated flows can be stratified when buoyancy effects are relatively important; they can also be annular when certain conditions of density similarity between the liquids, as well as other conditions are satisfied (*Joseph and Renardy*, 1993). Dispersed flows are characterized by one liquid forming pockets or enclosures, within a continuous region of the other liquid. These pockets can be in the form of spherical drops or randomly shaped droplets in a variety of sizes and shapes. The liquid that forms the continuous region is called the continuous phase and the other is known as the dispersed phase. When the size of the pockets is large compared to the conduit size, or the flow forms intermittent packets of either liquid, then it is called a slug or a plug flow respectively. When the dispersed phase forms packets that are relatively small compared to the size of the conduit, the flow is known as fully dispersed. Generally, a liquid-liquid flow may assume a large variety of combinations of the distinct cases just mentioned. It can be stratified, or plugs of continuous phases with dispersed phases within them, or fully dispersed with the dispersed phase distributed either homogeneously, or annularly or be stratified. Figure 2.1 shows a cartoon representation of some of the main configurations.

Many liquid-liquid dispersed flows of practical relevance, are composed of one aqueous phase (usually a polar liquid, like water) and a non-polar, oil phase (e.g. a petroleum

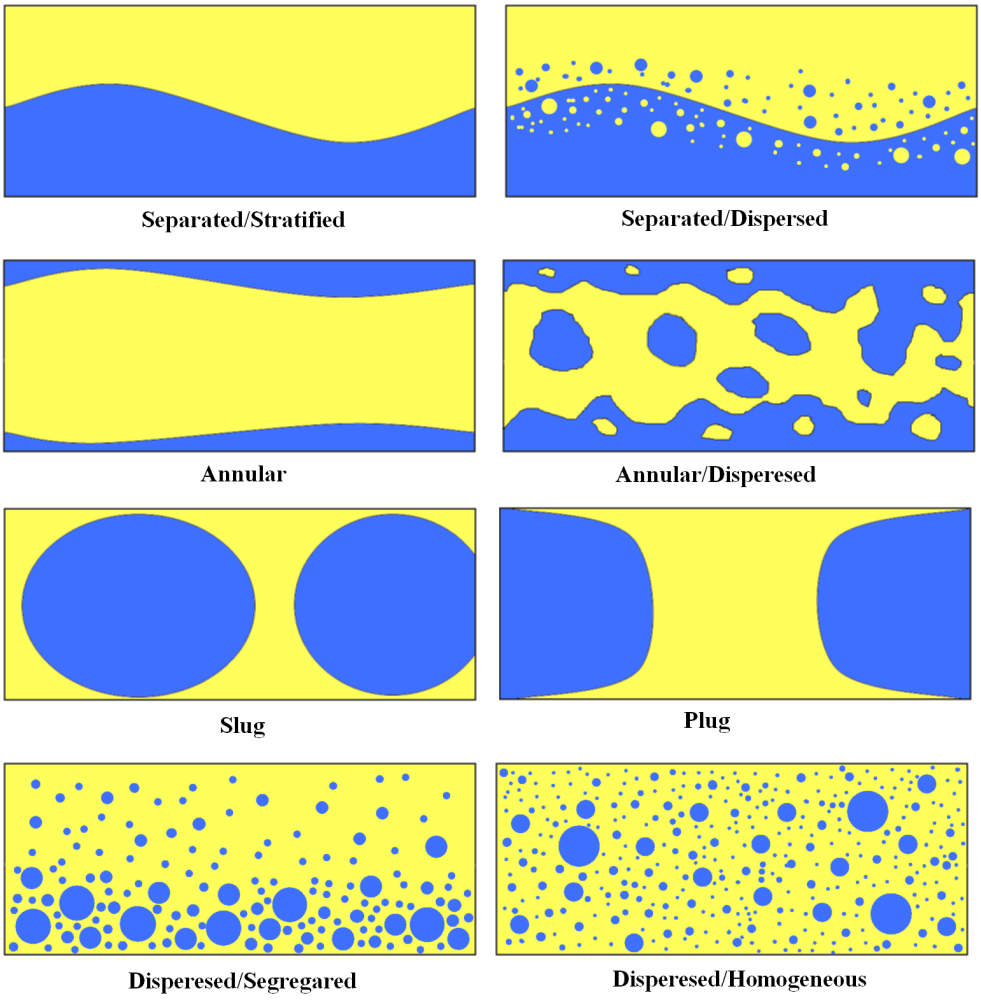

Figure 2.1: Major types of liquid-liquid flow patterns.

product). Hence, when water is the continuous phase the dispersion is known as Oil-in-Water (O/W), and when oil is the continuous phase it is known as Water-in-Oil (W/O). When it is of interest to stabilize a dispersion after its formation, chemical compounds known as Surface Active Agents (Surfactants) are added to either or both phases. Surfactants migrate to the interfaces between the phases, reduce the interfacial tension across the interface, and prevent the dispersed drops from merging together in a process known as coalescence; the dispersion in this case is known as a "stable" [2] dispersion or a "stabilized" emulsion[3]. In the absence of surfactants the breakup and coalescence of droplets will be determined purely through the laws of fluid mechanics and depend on the properties of the fluids themselves, without external effects on their surface chemistry; in this case the dispersions are known as being "unstable". These unstable dispersions are the primary subject of this dissertation.

2.1.2 Liquid-Liquid Flow Maps

The main factors that govern flow patterns and subsequently all properties[4], and behavior of a liquid-liquid flow, are summarized in Table 2.1. The four active forces in these flows- namely inertial, viscous, interfacial and gravitational- can be combined into the following non-dimensional groups:

[2] This does not indicate thermodynamic stability, but merely that separation time is much longer compared to unstable emulsions/dispersions; for even with surfactants, an emulsion will still be thermodynamically unstable, and given enough time will separate. An exception to this are microemulsions that are thermodynamically stable (*Prince*, 1977).

[3] An emulsion usually indicates small droplet diameters, on the order of 10 μm, while a dispersion does not indicate diameter limits. In this dissertation, the two terms are used interchangeably.

[4] Temperature is not an independent parameter, its effect is through changing the viscosities, densities and interfacial tension.

Table 2.1: Parameters governing liquid-liquid flows in pipes.

Fluid Properties	Viscosities of the liquids	μ_1, μ_2
	Densities of the liquids	ρ_1, ρ_2
	Interfacial tension between the two liquids	σ
Setup & Operational Properties	Conduit size (pipe diameter)	D
	Preferential wetting of conduit wall material (angle of contact)	β_1, β_2
	Conduit orientation: Pipe axis angle with the horizon	θ
	The superficial mixture velocity: Total flow rate of the mixture divided by the flow area	$U = \frac{Q_1+Q_2}{A}$
	Percent of constituting liquids	$\phi_1 = \frac{Q_1}{Q_1+Q_2}$

$$Re = \frac{\mathbf{U}D\rho}{\mu} \qquad \text{Reynolds number} \left(\frac{Inertia\ Forces}{Viscous\ Forces}\right) \tag{2.1a}$$

$$Ca = \frac{\mu_c \dot{\gamma} d}{\sigma} \qquad \text{Capillary number} \left(\frac{Viscous\ Forces}{Interfacial\ Forces}\right) \tag{2.1b}$$

$$We = \frac{\rho_c \mathbf{U}^2 D}{\sigma} \qquad \text{Weber number} \left(\frac{Inertia\ Forces}{Interfacial\ Forces}\right) \tag{2.1c}$$

$$Bo = \frac{\Delta\rho \mathbf{g} D^2}{8\sigma} \qquad \text{Bond number} \left(\frac{Buoyancy\ Forces}{Interfacial\ Forces}\right) \tag{2.1d}$$

Where $\dot{\gamma}$ is the shear strain rate, d is the droplet diameter, $\Delta\rho$ is the difference between the densities of the two liquids, $\mathbf{g}$ is the local gravitational acceleration and the subscript c refers to the continuous phase. Only three of these non-dimensional groups are independent. Either the Capillary or the Weber number would be of importance, depending on whether viscous or inertial forces dominate field of importance at the length-scales being considered.

Mapping flow patterns of liquid-liquid flows has been frequently addressed in the literature, although not as extensively as flow patterns in gas-liquid flows. Some of the most relevant works, in the scope of this dissertation, include *Govier and Aziz* (1972); *Nadler and Mewes* (1997); *Angeli and Hewitt* (2000b); *Fairuzov et al.* (2000); *Elseth* (2001); *Weg-*

mann and von Rohr (2006); *Mandal et al.* (2007) and a review by *Xu* (2007). Example maps are shown in Figures 2.2, 2.3, 2.4, 2.5 and 2.6. As can be seen from those maps, separated flow patterns appear at low mixture velocities in general. Increasing the level of turbulence results in more mixedness of the flow toward homogeneity, where fully and homogeneously dispersed flows appear at the highest levels of turbulence in the maps. The transition boundaries from separated to dispersed patterns is of high importance, since pressure drop behavior as well as other factors of engineering interest like drop size distribution, change dramatically across these boundaries. A unified theory that can predict the flow pattern given a determined set of the parameters mentioned in Table 2.1 does not exist yet, but with the amount of data that has accumulated in the literature some models that predict flow patterns with moderate success (e.g. *Torres-Monzon* (2006)) have appeared. Other advances have been made in predicting the transition boundaries, where *Brauner* (2001) has presented two models for such prediction. The first involves modifications to the Kolmogorov-Hinze model (*Kolmogorov*, 1949; *Hinze*, 1955) for emulsification in a turbulent flow that predicts the maximum droplet size. It applies for a Bond number range $Bo > 5$. The second model is a modified version of the Hughmark model (*Hughmark*, 1971) for predicting emulsification, that allows its application for a Bond number range of $Bo < 5$. However, predictions for liquid-liquid flows are limited to the transition boundaries; they cannot make reliable estimates for the maximum droplet size once the flow is in the dispersed regime.

Examination of flow pattern maps from the literature as well as preliminary experimental investigations on the fuel-water supply pipeline system as mentioned in Chapter I and described in detail in Chapter IV, showed that the flow regime for the entire range of flow rates of industrial interest is in the fully dispersed flow regime. Hence, this dissertation focuses only on the fully dispersed regime in horizontal pipes. The engineering interest here encompasses two main topics, namely the **flow resistance** in different parts of the pipeline and the **drop size distribution** of the dispersion; the former being important in

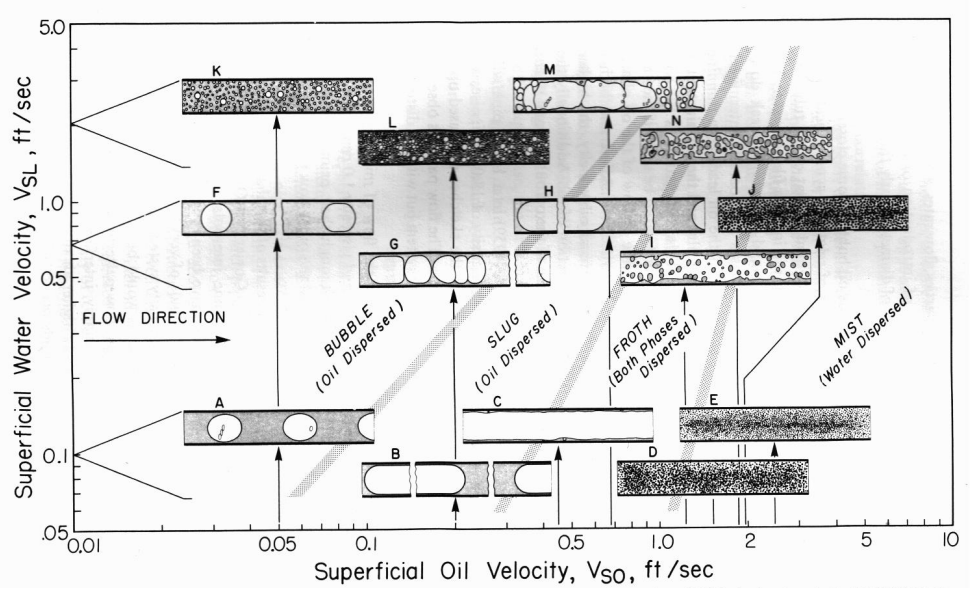

Figure 2.2: Flow pattern map after *Govier and Aziz* (1972), oil specific gravity is 0.998 and viscosity 0.0168 $kg/(m.s)$, pipe diameter 26.4 *mm*. In this figure, "Bubble" refers to a large droplet rather than a gas-in-liquid pocket.

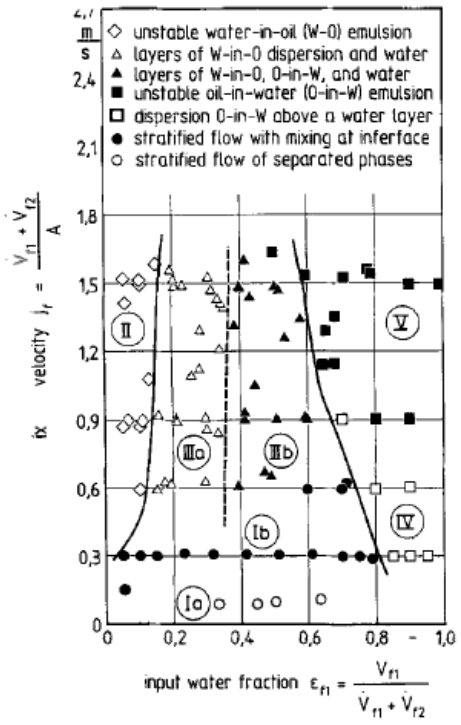

Figure 2.3: Flow pattern map by *Nadler and Mewes* (1997). Pipe diameter 59 *mm*.

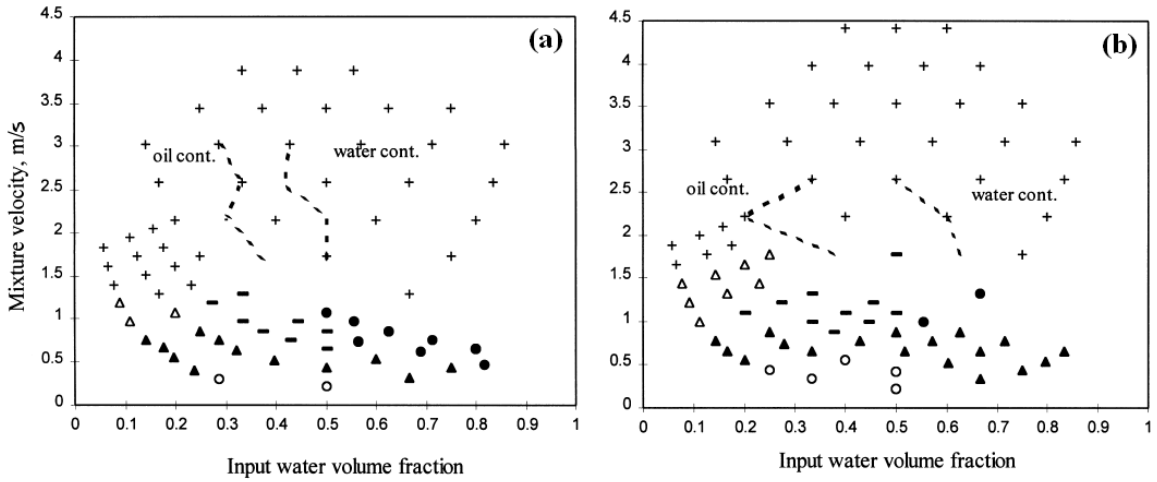

Figure 2.4: Flow pattern map by *Angeli and Hewitt* (2000b). Oil density 801 kg/m^3, viscosity 0.016 $kg/(m.s)$, interfacial tension with water 0.017 N/m.(a) Stainless steel pipe, diameter 24.3 *mm* (b) Acrylic pipe, diameter 24 *mm*. ○ stratified wavy, - three layers, △ stratified dispersed/oil, ▲ stratified wavy/drops, ● stratified/dispersed water, + dispersed, - - - phase boundaries.

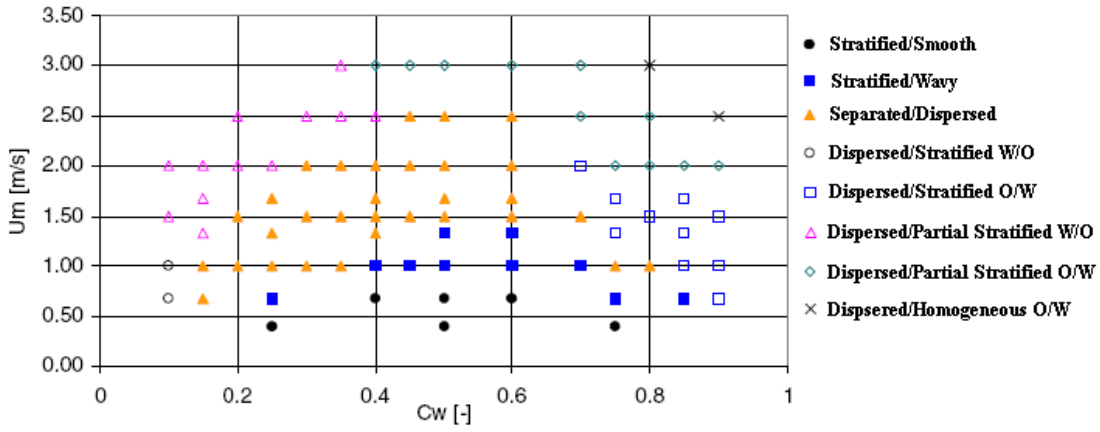

Figure 2.5: Flow pattern map by *Elseth* (2001). The horizontal axis is ϕ_{water}, and the vertical axis is the mixture velocity. Oil density 790 kg/m^3, viscosity 0.0164 $kg/(m.s)$, interfacial tension with water 0.043 N/m. Pipe diameter 50.8 *mm*.

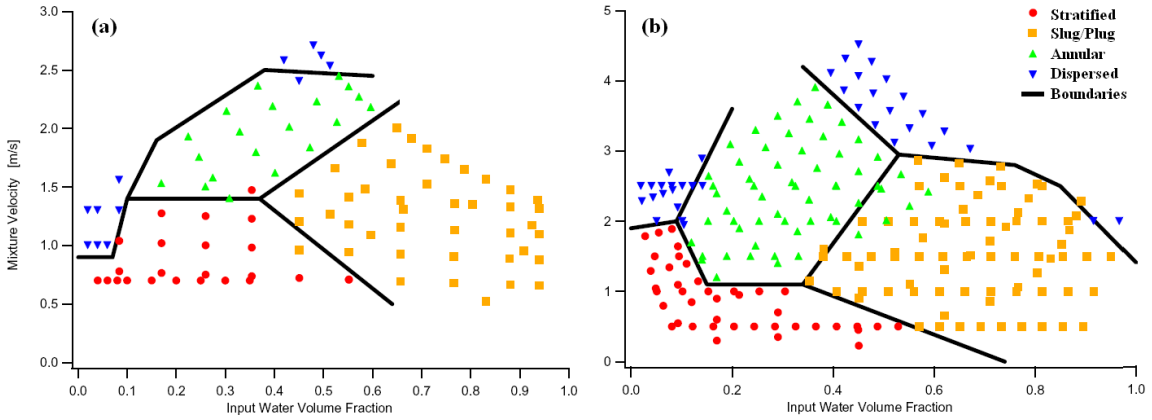

Figure 2.6: Flow pattern map by *Wegmann and von Rohr* (2006). The horizontal axis is ϕ_{water}, Oil density 819 kg/m^3, viscosity 0.043 to 0.052 $kg/(m.s)$, interfacial tension with water 0.0622 N/m. Pipe diameter (a) 7 mm, (b) 5.6 mm.

designing pipelines and the latter is important for chemical engineering applications where static mixers are employed, and in the combustion application mentioned in Chapter II. In combustion applications, emulsion fluid mechanics can affect the properties and behavior of the mist being atomized into the combustion chamber. As it turns out, these two aspects are not only of engineering importance, but also pose fundamental scientific questions that have not been fully answered; the literature review will demonstrate this in the next chapter.

CHAPTER III

Dispersed Liquid-Liquid Flows in the Literature

A literature survey of two main areas pertinent to liquid-liquid dispersed flows includes the pressure drop along a pipe and the methods of droplet size distribution measurement. This gives enough background to tackle the objectives of this work as stated in Chapter II.

3.1 Pressure Drop in Pipe Flows

Various approaches have been used to represent pressure drop behavior of unstable dispersed flows. A comprehensive review of these approaches is given by *Vielma* (2006). Dispersed flows of two Newtonian liquids can exhibit either a Newtonian or non-Newtonian behavior. The degree of departure from Newtonian behavior depends on: the level of turbulence, the dispersed phase ratio, the pipe diameter, the viscosity ratio of the liquids, and the size, shape and behavior of droplets, as well as other factors of less importance. Generally, no physically meaningful viscosity that can be ascribed to the flow.

3.1.1 Apparent Viscosity Representation

Treating a fully and homogeneously dispersed, liquid-liquid flow as a pseudo-single fluid with averaged properties seems, by intuition, convenient and plausible . A criterion to determine the applicability limits of this idea was suggested by *Baron et al.* (1953), by comparing inertia forces to drag forces that act on the dispersed phase, as expressed in

Relation 3.1.

$$\frac{d^2\rho_d U_m^2}{\mu_c U_d D} = \frac{\rho_c U_m D}{\mu_c}\left(\frac{d}{D}\right)^2 \frac{\rho_d}{\rho_c} \leq 1 \tag{3.1}$$

where the subscripts d and m denote the dispersed phase and the mixture respectively. d is a representative diameter of the dispersed phase droplets, which should be according to the model smaller than the Kolmogrov microscale ($d < \eta_k$). However, this condition was found not to be strictly forbidding, and even with droplets larger than the Kolmogorov scale (within a certain limit) the dispersed flow can be considered pseudo-single fluid. This was shown by *Ward and Knudsen* (1967), where they applied the criterion to their experimental observations. Using the Sauter mean diameter (d_{32}) of their particles as representative, and the mixture density ρ_m and apparent viscosity μ_m instead of the continuous phase values in the denominator. They obtained homogeneous, Newtonian behavior for dispersions that satisfied Relationship 3.2.

$$\frac{\rho_c U_m D}{\mu_c}\left(\frac{d_{32}}{D}\right)^2 \frac{\rho_d}{\rho_m} \leq 2 \tag{3.2}$$

$$\rho_m = \phi\rho_d + (1-\phi)\rho_c \tag{3.3}$$

According to this criterion many liquid-liquid systems, including the ones studied in this dissertation, can be considered behaving as pseudo-single fluids.

The concept of "apparent viscosity" facilitates the pseudo-single phase treatment. The definition of apparent (or mixture) viscosity as given in Equation 3.4 (*Brauner*, 2003) relies on the concept of viscosity (the ratio of shear stress to strain rate), however, physically it

cannot be equated to Newtonian viscosity.

$$\mu_m = \frac{\tau_m}{\dot{\gamma}} \qquad \text{Apparent Viscosity} \tag{3.4}$$

where τ_m is the shear stress of the multiphase flow.

3.1.1.1 Theoretical and Semi-Theoretical Apparent Viscosity Models for Liquid-Liquid Dispersions

The concept of apparent viscosity was first introduced by Einstein in the form of Equation 3.5 (*Einstein*, 1906) for solid spheres in fluid, in the infinitely dilute limit where $\phi << 0.1$. This condition makes the effects of interaction of spheres with each other negligible.

$$\frac{\mu_m}{\mu_c} = 1 + 2.5\phi \tag{3.5}$$

Since then numerous forms of apparent viscosity have appeared. They are, unfortunately, mostly model specific, relying on empirical constants and data fits. Some of the most relevant ones to this dissertation will be mentioned.

Taylor (1932) extended Einstein's formula of dilute solid-liquid systems to dilute liquid-liquid systems by taking into account the viscosity of the dispersed phase. He suggested the form given in Equation 3.6a. In the limit of $\mu_r \rightarrow \infty$ this relation reduces back to Equation 3.5.

$$\frac{\mu_m}{\mu_c} = 1 + 2.5\left(\frac{\mu_d + \frac{2}{5}\mu_c}{\mu_d + \mu_c}\right)\phi \tag{3.6a}$$

$$\mu_r = \frac{\mu_d}{\mu_c} \tag{3.6b}$$

Polynomial forms of different orders (Equation 3.7) allow the extension of Taylor's formula to higher ϕ limits.

$$\frac{\mu_m}{\mu_c} = 1 + K_1\phi + K_2\phi^2 + K_3\phi^3... \tag{3.7}$$

where K_1 is the Einstein shape factor for single spheres. The value of K_1 depends on μ_d. At higher ϕ (up to 0.2) the effect of the hydrodynamic interaction between dispersed droplets is expressed in K_2; and for even higher ϕ, the coefficient K_3 accounts for higher order interaction effects. Similar polynomial forms have been suggested by, among others, *Kunitz* (1926) for solutions, on an empirical basis; and by *Vand* (1948) for solid spheres on a semi-theoretical basis. The model of *Vand* (1948) can be cast in the form of Equation 3.8, for which the resulting coefficients obtained by Vand reduce to Equation 3.9.

$$\frac{\mu_m}{\mu_c} = 1 + K_1\phi + \left[\frac{1}{2}K_1(k_2 + 2q) + \hat{t}(k_2 - K_1)\right]\phi^2... \tag{3.8}$$

where k_2 is the shape factor of collision doublets, q is the hydrodynamic interaction constant, and $\hat{t}$ is the collision time constant.

$$\frac{\mu_m}{\mu_c} = 1 + 2.5\phi + 7.349\phi^2... \tag{3.9}$$

Another semi-theoretical model for colloidal suspensions of solid spheres (Equation 3.10) is that of *Krieger and Dougherty* (1959). This model has been applied successfully in some general liquid-liquid experimental studies as will be shown subsequently. Two key factors in this model are the ϕ^{max}, the maximum volumetric fraction of sphere packing, and the intrinsic viscosity μ_i, which *Krieger and Dougherty* (1959) found to be almost equal to 2.5, the value of K_1 first obtained by Einstein.

$$\frac{\mu_m}{\mu_c} = \left(1 - \frac{\phi_d}{\phi^{max}}\right)^{-\mu_i \phi^{max}} \tag{3.10}$$

Leviton and Leighton (1936) gave the relationship in Equation 3.11 for higher ϕ based on experimental data from milk suspensions. This relationship can be reduced back to Equation 3.6a for small ϕ.

$$\frac{\mu_m}{\mu_c} = exp\left[2.5\left(\frac{\mu_d + \frac{2}{5}\mu_c}{\mu_d + \mu_c}\right)\left(\phi + \phi^{\frac{5}{3}} + \phi^{\frac{11}{8}}\right)\right] \tag{3.11}$$

Oldroyd (1953) derived a constitutive relationship, Equation 3.12a, that took into account the effect of droplet size (assuming monodispersity), interfacial tension, and the rate of shear, which would allow the consideration of non-Newtonian dispersions. The ϕ limits are somewhat higher than the infinitely dilute limit, and the relationship reduces to Equation 3.6a as $\phi \to 0$.

$$\left(1 + \zeta_1 \frac{\mathbf{D}}{\mathbf{D}t}\right)\left(\tau_{ij} + p\delta_{ij}\right) = 2\mu_0 \left(1 + \zeta_2 \frac{\mathbf{D}}{\mathbf{D}t}\right)\epsilon_{ij} \tag{3.12a}$$

$$\frac{\mu_{m0}}{\mu_c} = \left(1 + 2.5\frac{\mu_d + \frac{2}{5}\mu_c}{\mu_d + \mu_c}\phi + O\left(\phi^2\right)\right) \tag{3.12b}$$

$$\zeta_1 = \frac{(16\mu_c + 19\mu_d)\, d}{40\,(\mu_c + \mu_d)\,\sigma}\left[3\mu_c + 2\mu_d + \frac{\mu_c\,(16\mu_c + 19\mu_d)\,\phi}{5\,(\mu_c + \mu_d)} + O\left(\mu_c \phi^2\right)\right] \tag{3.12c}$$

$$\zeta_2 = \frac{(16\mu_c + 19\mu_d)\, d}{40\,(\mu_c + \mu_d)\,\sigma}\left[3\mu_c + 2\mu_d - \frac{3\mu_c\,(16\mu_c + 19\mu_d)\,\phi}{10\,(\mu_c + \mu_d)} + O\left(\mu_c\phi^2\right)\right] \tag{3.12d}$$

where τ_{ij} is the stress tensor, p is the pressure, ϵ_{ij} is the strain rate tensor, ζ_1 is the relaxation time, ζ_2 is the retardation time, and μ_0 is the viscosity in the limit of infinitesimally small shear rate. The coefficients of the second order ϕ terms in this model have no physical significance. And due to the limitations of the the perturbation method used in the derivation, those coefficients cannot be obtained reliably. Physically, this could be justified by the dilute assumption in the model, since second order ϕ terms express the interaction of droplets, which becomes significant only at high concentrations. *Oldroyd* (1955) took into account the effect of having an interfacial film between the dispersed and continuous phases on the constitutive relationship of Equation 3.12a. When this interfacial film offers only viscous resistance (no elasticity effects), Oldroyd derived Equation 3.13 for apparent viscosity.

$$\frac{\mu_m}{\mu_c} = \left(1 + 2.5\frac{\mu_d + \frac{4}{5}\,(2\xi + 3\upsilon)\,/d + \frac{2}{5}\mu_c}{\mu_d + \frac{4}{5}\,(2\xi + 3\upsilon)\,/d + \mu_c}\phi\right) \tag{3.13}$$

where ξ and υ are coefficients related to the interfacial film. ξ is known as the shear viscosity and υ is an analogue of the bulk viscosity in two dimensions, hence known as the area viscosity. The effect of the film appears as an increase in the dispersed phase viscosity by the amount $\frac{4}{5}\,(2\xi + 3\upsilon)\,/d$.

An even more general constitutive equation was derived by *Frankel and Acrivos* (1970), for liquid-liquid systems in the infinitely dilute limit, with the condition of no colloidal-sized droplets, allowing slight deviations from spherical particle shape. *Choi and Schowalter* (1975) expanded the constitutive equation of Frankel and Acrivos to somewhat higher ϕ using a "cell-model". However, even this improvement was lacking due to the arbitrari-

ness involved in selecting some of the model-specific parameters. A somewhat similar relationship was obtained by *Yaron and Gal-Or* (1972) using also a cell-model approach.

Barnea and Mizrahi (1975) developed a model for dispersions of solid particles in liquid and extended it to apply for liquid-liquid systems (Equation 3.14a) with spherical droplets that interact with each other only hydrodynamically (through the fluid).

$$\frac{\mu_m}{\mu_c} = B\left(\frac{\frac{2}{3}B + \mu_r}{B + \mu_r}\right) \tag{3.14a}$$

$$B = exp\left[\frac{5}{3}\frac{\phi}{(1-\phi)}\left(\frac{\mu_d + \frac{2}{5}\mu_c}{\mu_d + \mu_c}\right)\right] \tag{3.14b}$$

Pal (2003) introduced two new relationships that are valid for large ϕ, Equations 3.15a and 3.15b, which will be referred to as Pal Model II and Pal Model III respectively.

$$\frac{\mu_m}{\mu_c}\left(\frac{M - P + 32\mu_m/\mu_c}{M - P + 32}\right)^{N-1.25}\left(\frac{M + P - 32}{M + P - 32\mu_m/\mu_c}\right)^{N+1.25} = exp\left(\frac{2.5\phi}{1 - \phi/\phi^{max}}\right) \tag{3.15a}$$

$$\frac{\mu_m}{\mu_c}\left(\frac{M - P + 32\mu_m/\mu_c}{M - P + 32}\right)^{N-1.25}\left(\frac{M + P - 32}{M + P - 32\mu_m/\mu_c}\right)^{N+1.25} = \left(1 - \frac{\phi}{\phi^{max}}\right)^{-2.5\phi^{max}} \tag{3.15b}$$

where

$$M = \sqrt{\frac{64}{Ca^2} + 1225\mu_r^2 + 1232\frac{\mu_r}{Ca}} \tag{3.15c}$$

$$P = \frac{8}{Ca} - 3\mu_r \tag{3.15d}$$

$$N = \frac{22/Ca + 43.75\mu_r}{M} \tag{3.15e}$$

Both Pal Model II & III are obtained by applying the Brinkman-Roscoe differential scheme to Equation 3.16a, which Pal suggested as an analogy to a model of the shear modulus of viscoelastic emulsions derived by *Palierne* (1990) for infinitesimally small ϕ, in order to expand to higher ϕ.

$$\frac{\mu_m}{\mu_c} = 1 + 5I\phi \tag{3.16a}$$

$$I = \frac{4(2 + 5\mu_r)/Ca + (\mu_r - 1)(16 + 19\mu_r)}{40(1 + \mu_r)/Ca + (2\mu_r)(16 + 19\mu_r)} \tag{3.16b}$$

The difference between Pal Model II & III lies in the assumption about how ϕ_d changes when the number of the dispersed particles changes by an infinitesimal amount. In the derivation of Pal Model II this change is assumed to be $\mathbf{d}[\frac{\phi}{1-\phi/\phi^{max}}]$, while for Pal Model III it is assumed to be $\frac{\mathbf{d}\phi}{1-\phi/\phi^{max}}$, where ϕ^{max} is the maximum packing volume fraction of undeformed droplets. The value of ϕ^{max} is not fixed, and it depends on the packing form (for a simple cubic packing $\phi^{max} = \frac{\pi}{6}$, for cubic close and hexagonal close $\phi^{max} = \frac{\pi}{3\sqrt{2}}$ and for random packing $\phi^{max} \approx 0.64$ (*Jaeger and Nagel*, 1992)). *Derkach* (2009) argued that ϕ^{max} is simply a fitting factor with a physical meaning. By comparing both models with literature data on stabilized emulsions of different kinds, (*Pal*, 2003) found Pal Model III in close agreement with the data, while Pal Model II agreed only for very small values of ϕ_d but deviated significantly at higher ϕ_d.

3.1.1.2 Experimental Determination of Apparent Viscosity in The Laminar Regime

For $Ca << 1$, all the apparent viscosity relationships mentioned in 3.1.1.1 predict an increase of μ_m with increasing ϕ_d, until the point of phase inversion where the continuous phase becomes dispersed and the dispersed phase continuous. It should be noted that the phase inversion point is system specific, depends on the nature of the liquids being mixed, the method of mixing and other factors, and may suffer significant hysteresis (*Vassen and Stein*, 1995; *Ioannou et al.*, 2005). The trend of increasing μ_m with increasing ϕ is verified experimentally for unstable dispersions, where small Ca can be achieved through laminar flows, as the following examples have shown.

Cengel et al. (1962) determined μ_m in laminar pipe flows indirectly by measuring bleeding flow rates and corresponding pressure drops through capillary tubes attached to the pipe. μ_m was calculated using a modified version of Hagen-Pouseuillle's law that accounts for the rather significant entrance and exit losses in capillary tubes. Results indicated an increase in μ_m with increasing ϕ_d but were inconclusive due to shortcomings in the measurement method.

Barnea and Mizrahi (1976) measured the apparent viscosity of dispersions prepared in a batch process, using a viscometer in the preparation device, immediately after preparation. Results were in agreement with both Equation 3.11 and Equation 3.17 which is an extension of Equation 3.13 to high ϕ_d as suggested in *Barnea and Mizrahi* (1976).

$$\frac{\mu_m}{\mu_c} = exp\left[2.5\frac{\mu_d + \frac{4}{5}(2\xi + 3\upsilon)/d + \frac{2}{5}\mu_c}{\mu_d + \frac{4}{5}(2\xi + 3\upsilon)/d + \mu_c}\left(\frac{\phi}{1-\phi}\right)\right] \tag{3.17}$$

As a more practical approach for pipe flows, *Pal* (1987, 1993) measured apparent viscosity indirectly in the laminar range, by fitting pressure drop data over portions of the laminar regime. The value of μ_m that gives the "best fit" of measured pressure drop data to the Hagen-Poiseuille law (see Appendix A) in Equation 3.18 is selected as the apparent

viscosity of a mixture at some constant ϕ. *Omer* (2009) also used a similar method in determining μ_m. This method, although convenient, cannot reliably distinguish any possible non-Newtonian behavior in the laminar regime.

$$f = \frac{16}{Re_m} \tag{3.18}$$

where

$$Re_m = \frac{\rho_m U D}{\mu_m} \tag{3.19}$$

$$\tag{3.20}$$

It has been shown that many surfactant-stabilized dispersions in the laminar regime, when at dispersed phase concentrations of $\phi < 0.5$, behave as Newtonian fluids. Non-Newtonian effects appear only in the approximate concentration range of $0.5 \sim 0.55 < \phi < 0.6 \sim 0.65$, and intensify in the very high (or jammed) concentration limit of $\phi > 0.6 \sim 0.65$ (see *Pal* (2000); *Krynke and Sek* (2004)). The results of *Pal* (1987, 1993); *Omer* (2009) for unstable dispersions were in line with these findings. However, as will be discussed soon, Pal and Omer's systems in the turbulent regime showed strong non-Newtonian behavior, which suggests that not all systems are fully Newtonian in the laminar regime, especially close to the transition zone. *Pouplin et al.* (2010) demonstrated this possibility. Their results for dispersions of $\phi_d < 0.5$ showed a deviation from Newtonian behavior in the final portion of the laminar region and before the inception of the transition region (will be shown in 3.1.2.2). They determined μ_m using the model of *Krieger and Dougherty* (1959) (Equation 3.10). It gave a close fit to μ_m calculated using Equation 3.18 (assuming $\phi^{max} = 0.74$), but giving a more consistent basis for comparison.

3.1.1.3 Apparent Viscosity of Unstable Dispersions in The Turbulent Regime

The effect of *Re* on apparent viscosity shows in many of the published data of turbulent unstable dispersed flows. However, not many of the theoretical and semi-theoretical relationships of apparent viscosity account for the effect of *Re*. Apart from the constitutive relationships mentioned in 3.1.1.1, which are difficult for direct application, the Pal Model II & III are the only ones that give any indication of turbulence. *Pal* (2007) argued that the $Ca \rightarrow 0$ limit would be indicative of laminar flows because, according to him, the Newtonian behavior of dispersed flows in the laminar regime results from undeformed droplets. *Pal* (2007) supported his argument by demonstrating the good fit of experimental data from the laminar regime with the $Ca \rightarrow 0$ limit of Pal Model II, given in Equation 3.21 (and the same limit for Pal Model III is given in Equation 3.22).

$$\frac{\mu_m}{\mu_c}\left(\frac{2\mu_m/\mu_c + 5\mu_r}{2 + 5\mu_r}\right)^{3/2} = exp\left(\frac{2.5\phi_d}{1 - \phi_d/\phi^{max}}\right) \tag{3.21}$$

$$\frac{\mu_m}{\mu_c}\left(\frac{2\mu_m/\mu_c + 5\mu_r}{2 + 5\mu_r}\right)^{3/2} = \left(1 - \frac{\phi_d}{\phi^{max}}\right)^{-2.5\phi^{max}} \tag{3.22}$$

On the other hand, Pal suggested that the $Ca \rightarrow \infty$ limit of Pal Model II, as given in Equation 3.23 (and the same limit for Pal Model III is given in Equation 3.24), would be representative of turbulent flows, since the high shear rates in the near-wall region would result in highly deformed droplets according to *Pal* (2007). Pal offered some experimental data fits to Equation 3.23, but the match was not as good as that for Equation 3.21 of the laminar regime. Furthermore, the non-Newtonian behavior in the turbulent regime makes determining apparent viscosity without specifying the *Re* inaccurate in the best case. The photographic evidence of *Collins and Knudsen* (1970) for droplet deformation cited

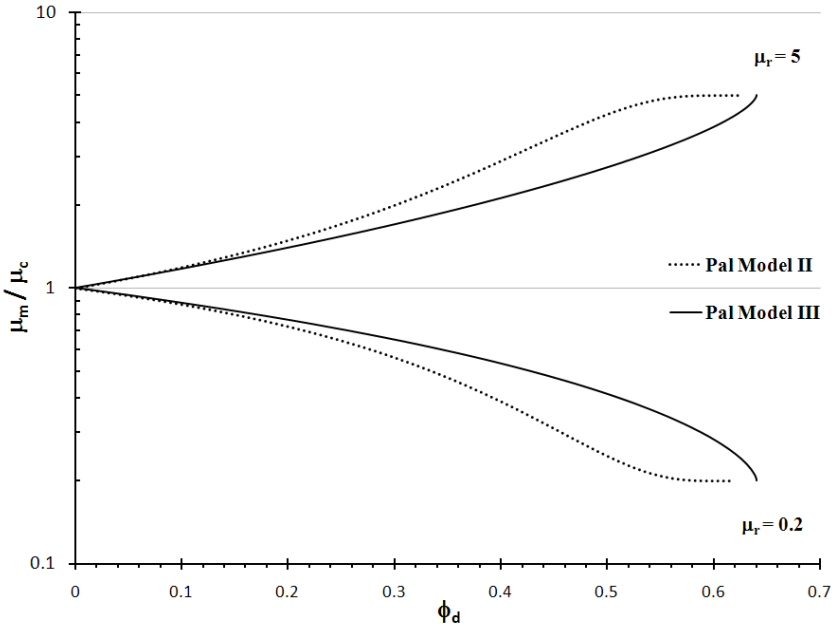

Figure 3.1: Apparent viscosity as a function of ϕ_d according to the $Ca \rightarrow \infty$ limit of Pal Model II and Pal Model III when $\mu_r > 1$ and when $\mu_r < 1$. $\phi^{max} = 0.64$.

by *Pal* (2007) was under flow conditions not typical for fully dispersed flows in that the setup allowed for the two phases to mix only due to pipe turbulence, and there was no droplet formation in a high-shear region before the pipe flow section, as is typical for fully dispersed flows. Figure 3.1 shows the trends of Equations 3.23 & 3.24; it can be seen that they allow the transition of μ_m between μ_c and μ_d, and the limit when $\phi_d = \phi^{max}$ is not physical because it predicts $\mu_m = \mu_d$ at that point. Nevertheless, the model is significant for allowing the decrease of apparent viscosity with increasing ϕ_d when $\mu_r < 1$.

$$\frac{\mu_m}{\mu_c}\left(\frac{\mu_r - \mu_m/\mu_c}{\mu_r - 1}\right)^{-2.5} = exp\left(\frac{2.5\phi_d}{1 - \frac{\phi_d}{\phi^{max}}}\right) \tag{3.23}$$

$$\frac{\mu_m}{\mu_c}\left(\frac{\mu_r - \frac{\mu_m}{\mu_c}}{\mu_r - 1}\right)^{-2.5} = \left(1 - \frac{\phi_d}{\phi^{max}}\right)^{-2.5\phi^{max}} \tag{3.24}$$

Cengel et al. (1962) obtained apparent viscosity in the turbulent regime by comparing the Blasius equation (Equation A.11) as a function of Re_m to their pipe-flow friction factor data, as a function of Re_c (defined in Equation 3.25), fitted to the general form of the Blasius Equation (Equation 3.26).

$$Re_c = \frac{\rho_m U_m D}{\mu_c} \tag{3.25}$$

$$f = aRe_c^{-b} \tag{3.26}$$

where μ_m can be determined through Equation 3.27[1], and b will determine the dependence of μ_m on Re_c; for $b = 0$ the dispersion will be Newtonian. *Cengel et al.* (1962) found that dispersions in the vertical portion of their test section behaved as Newtonian, and had increasing μ_m with ϕ_d, while in the horizontal section, which followed the vertical, the dispersion behaved as non-Newtonian. They speculated partial coalescence and change in the structure of the dispersion as a possible reason, with no further evidence. As mentioned above, their work was inconclusive with regards to asserting the behavior of fully dispersed flows in pipes.

$$\mu_m = \mu_c \left(\frac{a}{0.079} Re_c^{0.25-b} \right)^4 \tag{3.27}$$

Faruqui and J. (1962); *Ward* (1964) used velocity profile data to determine μ_m. They measured the pipe cross-sectional velocity profile using stagnation pressure probes, and used the data to calculate μ_m from the Law of the Wall as explained in Appendix A. They

[1]This is not a theoretical model that links μ_m to Re because the Blasius equation is an experimental relationship.

found increasing μ_m with increasing ϕ_d. While *Ward and Knudsen* (1967), using pressure drop data, found that high μ_r (on the order of 200) lead to decreasing μ_m with increasing ϕ_d. Ward ascribed this exceptional behavior to an anomalous droplet size distribution observed in the high μ_r dispersion (few large droplets containing the bulk of dispersed phase, surrounded by much smaller droplets). Commenting on this result, *Pal* (1993) argued that high μ_r would have caused significantly higher modification of turbulence compared to the other cases of low μ_r, resulting in the reduction of μ_m with increasing ϕ_d.

Pal (1993); *Omer* (2009) and *Pouplin et al.* (2010) followed the method of *Cengel et al.* (1962) for determining μ_m. *Pal* (1993) and *Omer* (2009) had dispersions exhibiting various non-Newtonian effects. *Pal* (1993) found decreasing μ_m with increasing ϕ_d in turbulent flows reported at constant Re_c, while *Omer* (2009) reported decreasing μ_m with increasing ϕ_d for promptly unstable dispersions, and increasing μ_m with increasing ϕ_d for dispersions that did not separate as fast, all without specifying a Reynolds number. *Pouplin et al.* (2010) found increasing μ_m with increasing ϕ_d. From the foregoing discussion it can be seen that the change of apparent viscosity with dispersed phase ratio does not have a clear trend in the turbulent regime, and more investigation is needed to enable the prediction of the behavior to be expected.

3.1.2 Friction Factor of Fully Dispersed Flows

3.1.2.1 Representation of The Friction Factor

The non-dimensionalization of the resistance of liquid-liquid dispersed flows in pipes has followed a similar path to single-phase Newtonian fluids. Wall friction is the dominant cause of pressure loss in these flows, hence the friction factor, as described in Appendix A, is the most utilized method of non-dimensionalizing pressure drop. The friction factor for liquid-liquid dispersed flows is generally not measured directly, but calculated through Equation A.9 using average flow properties of ρ_m and U_m. However, the choice of the flow-condition parameter (the abscissa) against which to represent the friction factor

(ordinates) has not been as clear a choice. For single phase fluids, the friction factor is plotted against the Reynolds number when the fluid is Newtonian, and against the generalized Reynolds number (Equation A.14) when the fluid is non-Newtonian, neither of these parameters can be easily determined for unstable liquid-liquid dispersed flows. The non-uniqueness of and the general difficulties in determining an apparent viscosity as outlined in 3.1.1.2 and 3.1.1.3, and the reliance of many of the approaches for determining apparent viscosity on the friction factor further complicate the choice of the abscissa parameter. A commonly used choice is Re_c. The viscosity of the continuous phase provides an appropriate and logical first-guess, especially when ϕ_d is small. Comparing the resulting plots to familiar single-phase, Newtonian $f-Re$ curves and diagrams like the Blasius or the Moody diagram (see Appendix A) gives an estimate of how close the dispersion is to Newtonian behavior and if it is close, an evaluation of its apparent viscosity. *Cengel et al.* (1962), and *Pal* (1987) used this method. Figure 3.2 shows some of their results. The slopes of the least square fits (not shown) for the highest concentrations (50% and 44.98%) are very close to the slope of the Blasius equation, indicating fairly close behavior to Newtonian, while the other concentrations are close to Newtonian, but to a lesser degree. As mentioned in 3.1.1.3 *Cengel et al.* (1962) used this proximity to assign an apparent viscosity to the dispersion.

Using Re_m instead of Re_c brings the abscissa range across which transition from laminar to turbulent flow happens into the transition range of single phase Newtonian fluids. This can help identify non-Newtonian behavior and quantify the effects of different parameters on the stability of the dispersion flow. The choice of μ_m can be based on the laminar or the turbulent portion of the data, so long as the selection is maintained throughout the analysis. Figure 3.3 shows this effect on the data obtained by *Pal* (1987) and *Pal* (1993) with μ_m based on laminar data.

Other methods of presenting flow resistance include scaling the two-phase pressure drop with the pressure drop of one of the phases at the same volumetric or mass flow rate, or simply presenting the pressure drop per unit length of pipe as a function of the ratio of

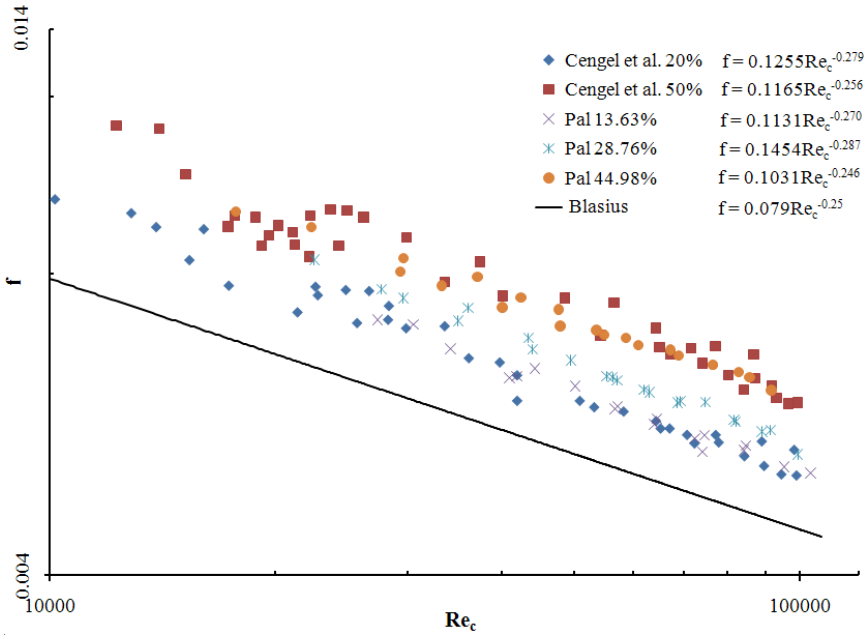

Figure 3.2: The friction factor of O/W dispersions at different concentrations as obtained by *Cengel et al.* (1962) in vertical pipes and by *Pal* (1987) in horizontal pipes.

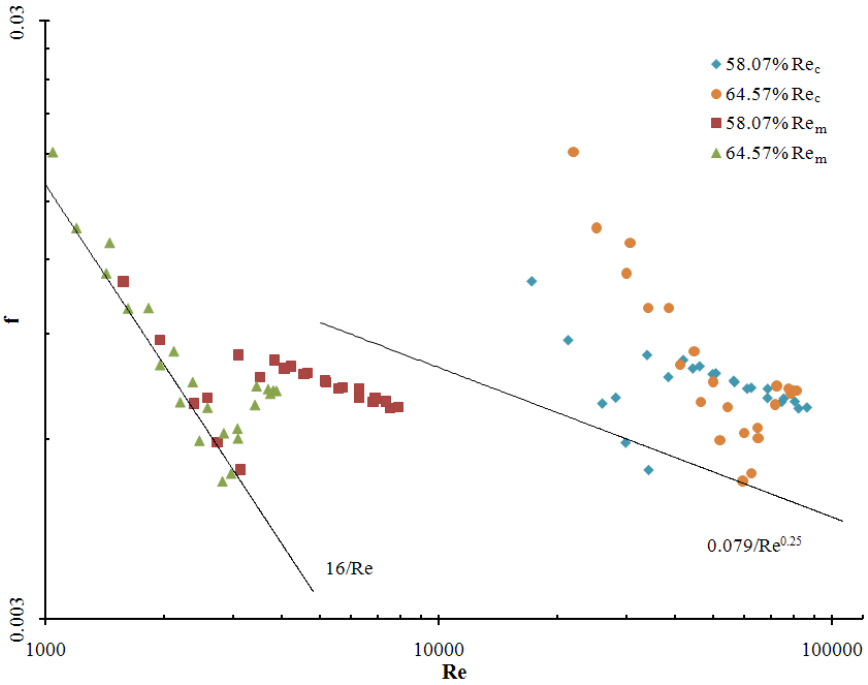

Figure 3.3: Friction factor of O/W dispersions obtained by *Pal* (1987). μ_m = 9.8713 mPa.s for ϕ_d = 0.5807 and μ_m = 19 mPa.s for ϕ_d = 0.6457. The Hagen-Pouseuillle line and the Blasius line are also shown.

one of the phases and volumetric flow rate.

In this dissertation both Re_c and Re_m will be used. We will demonstrate that using Re_m is essential in distinguishing laminar, turbulent and transition regimes, as they might not always be as clear as it looks in Figure 3.3, especially when the amount of data available is limited. We will also offer analysis of pressure drop data completely independent of the concept of apparent viscosity.

3.1.2.2 Friction Factor of Dispersions as Found in The Literature

The main literature works that have reported the friction factor of fully dispersed unstable liquid-liquid flows are summarized in Table 3.1. They all use oils of fossil origins, usually fuels, and mixing is done in an agitated vessel and/or through the pump. Only *Ward* (1964) has included an in-situ droplet size measurement and analysis that is directly linked to the unstable dispersion.

The findings on the behavior of the friction factor are summarized here. *Faruqui and J.* (1962) found that their dispersions would fit the curve of the Blasius equation for Re_m, with a steady, positive average shift of about 4% which they attributed to possible errors in measuring the pipe diameter, their results are shown in Figure 3.4. All the examined disperions seem to demonstrate Newtonian behavior.

Table 3.1: Literature summary of fully dispersed liquid-liquid flows in pipes

Reference	Oil phase Viscosity $[mPa.s]$	Oil phase Density $[kg/m^3]$	Aqueous phase Viscosity $[mPa.s]$	Aqueous phase Density $[kg/m^3]$	σ $[mN/m]$	T_{ref} $[^\circ C]$	Dispersion type	Flow regime	U_m range $[m/s]$	Pipe ID $[mm]$	Pipe material	Pipe orientation	Mixing method
Cengel et al. (1962)	Shell Solv 360 0.976	781.7	Water 0.967	998	49	21.66	O/W	Turbulent and laminar		18.923	Copper	Vertical then horizontal	Mixing in an agitated tank
Faruqui and J. (1962)	Shell Solv 360 0.976	781.7	Water 1.015	998	49	19.44	O/W	Turbulent	1.35 to 4.23	18.923	Copper	Vertical	Mixing in an agitated tank
Ward (1964)	Shell Solv 360, California White Oil Number One, White Oil Heavy 1.005, 15.6, 214	783.6, 869, 884.5	Water 1.003	998	49, 52, 48	20	O/W	Turbulent	1.00 to 5.35	21.082	Copper	Vertical	Mixing in an agitated tank
Pal (1987)	Bayol 35 (a mineral oil) 2.41	780	Tap water 0.891	997	na	25	W/O and O/W	Laminar and turbulent	1.00 to 5.35	8.89, 12.6, 15.8	Seamless stainless steel	Horizontal	Mixing in an agitated tank
Omer (2009)	Shell Pella oil, EDM Monarch, EDM 244 oil 5.4, 6, 2.5	816, 785, 753	Tap water 0.891	997	11.3, 37.8, 40.5	25	W/O	Laminar and turbulent	0.13 to 7.76	8.9, 12.6, 15.8, 26.5, 26.5	Stainless steel (first 4), PVC (5th)	Horizontal	Mixing in an agitated tank
Pouplin et al. (2010)	n-Heptane 0.4	684	A mixture of water and glycerin (43% vol.) 3.2	1102	31	29	O/W	Laminar and turbulent	0.28 to 1.20	50	PolyMethyl MethAcrylate	Horizontal	Mixing through the centrifugal pump

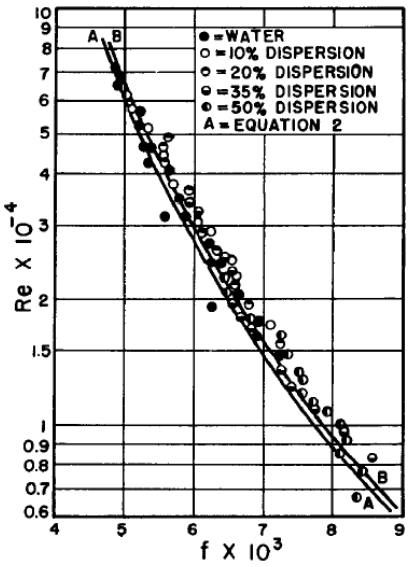

Figure 3.4: The friction factor of the dispersed flows in vertical pipes examined by *Faruqui and J.* (1962). ($Re_m vs f$), at different ϕ_d.

Ward (1964) found similar Newtonian behavior in the California White Oil Number One O/W dispersions he examined in vertical flow. This is shown in Figure 3.5. Heavy White Oil O/W dispersions (Figure 3.6) also behaved Newtonian except at $\phi_d = 0.27$. Ward attributed this anomalous behavior to the "inhomogeneous" structure of this particular dispersion; the main volume of the oil phase was concentrated in a few, relatively large droplets with a large number of smaller droplets that made up a small portion of the volume. This strong bimodal distribution disqualified $\phi_d = 0.27$ dispersions from being classified as pseudo-single fluid according to the criterion of Inequality 3.2.

Pal (1993) investigated both O/W and W/O dispersions, as well as the pipe diameter effect where larger pipe diameters resulted in higher friction factors at the same Re_m. Some of his findings are shown in Figure 3.7. Most dispersions investigated by Pal showed non-Newtonian behavior in the turbulent regime.

Omer (2009) examined three different oils in W/O dispersions, flowing in different diameter horizontal pipes. Figure 3.8 shows results for two different concentrations. The pipe diameter effect was similar to that of *Pal* (1993). The EDM 244 oil showed non-Newtonian turbulent behavior for almost all concentrations. The EDM Monarch oil had

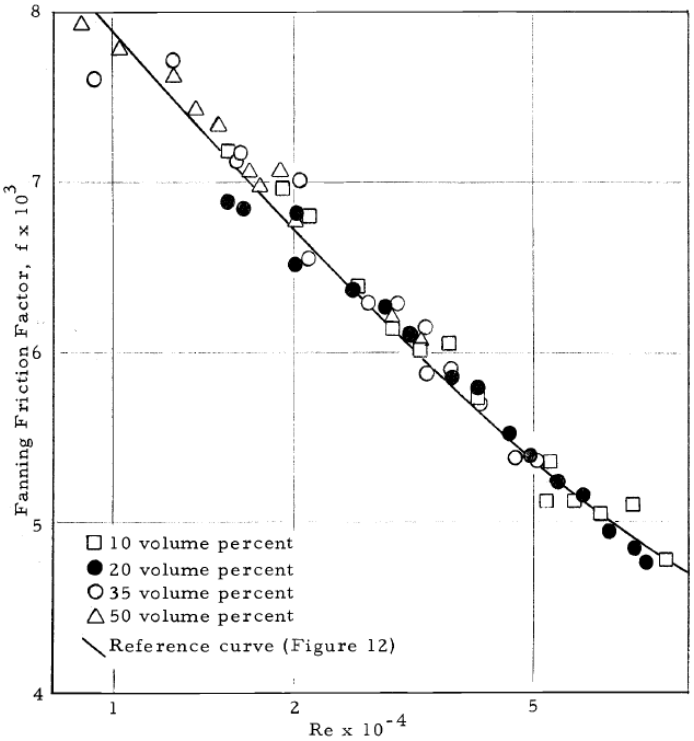

Figure 3.5: The friction factor of California White Oil Number One O/W dispersions in vertical pipes, where μ_m values are obtained from velocity profile data *Ward* (1964).

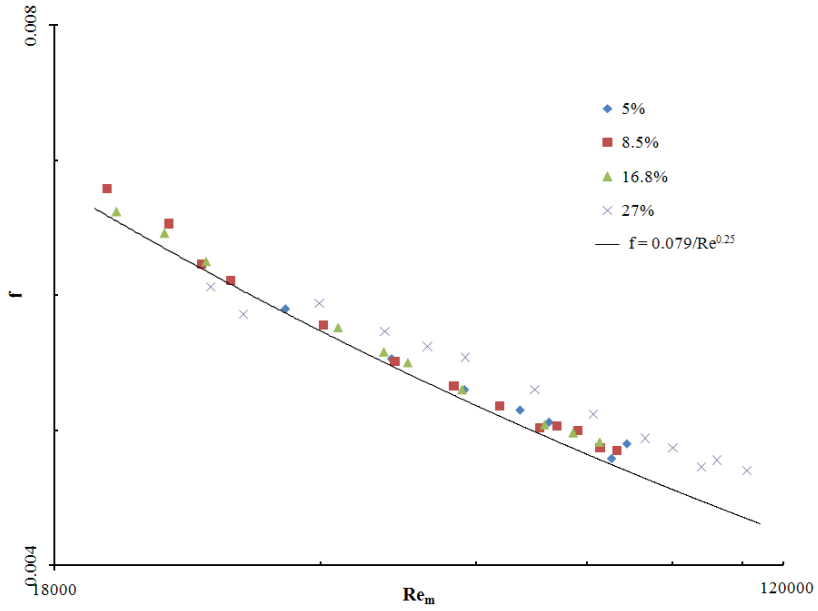

Figure 3.6: The friction factor of Heavy While Oil O/W dispersions in vertical pipes at different ϕ *Ward* (1964). μ_m values from *Ward and Knudsen* (1967).

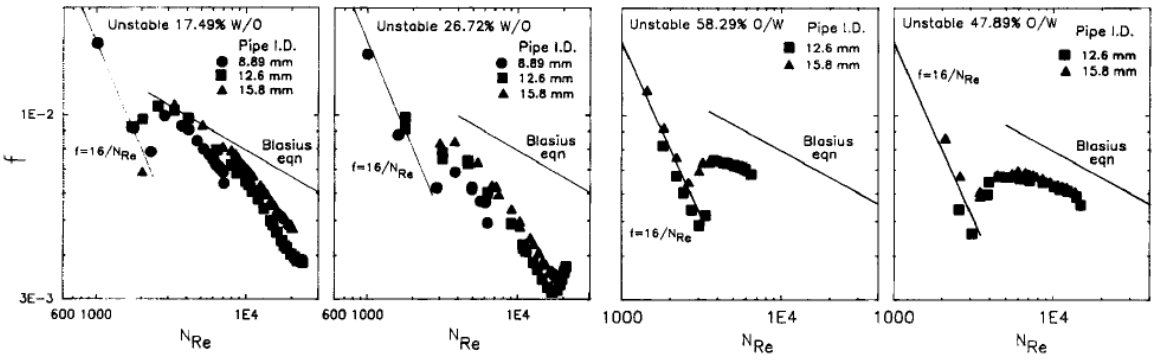

Figure 3.7: The friction factor of W/O and O/W dispersions in horizontal pipes by *Pal* (1993). μ_m is based on the laminar regime.

somewhat more Newtonian behavior in both regimes, but with a very suppressed transition region. While the Shell Pella oil had a Newtonian turbulent behavior, and clear transition regions, its laminar behavior was not strictly Newtonian. This non-Newtonianness was manifested by deviations from the Hagen-Pouseuillle's law, with a dependence on pipe diameter (Figure 3.8 C and F).

Pouplin et al. (2010) used a refractive-index-matching mixture forming an O/W dispersion. Their results are shown in Figure 3.9. Data in both low and high *Re* limits ($1500 < Re$ and $Re > 5000$) align well with single phase, Newtonian behavior. The slight departure from laminar Newtonian data in the $1500 < Re < 3000$ range was explained by higher measured velocity fluctuations compared to those at lower *Re*, and although these fluctuations didn't destabilize the flow, they increased energy dissipation; no explanation was given for the elevated magnitude of these velocity fluctuations. In the transition regime, increasing ϕ_d delayed transition to turbulence (increased the critical Reynolds number), and increased the width of the *Re* range of the transition regime.

3.1.2.3 Other Forms of Pressure Drop Representation

Some of the works that have investigated various unstable liquid-liquid flows in which the fully dispersed configuration formed a significant portion are summarized in Table 3.2.

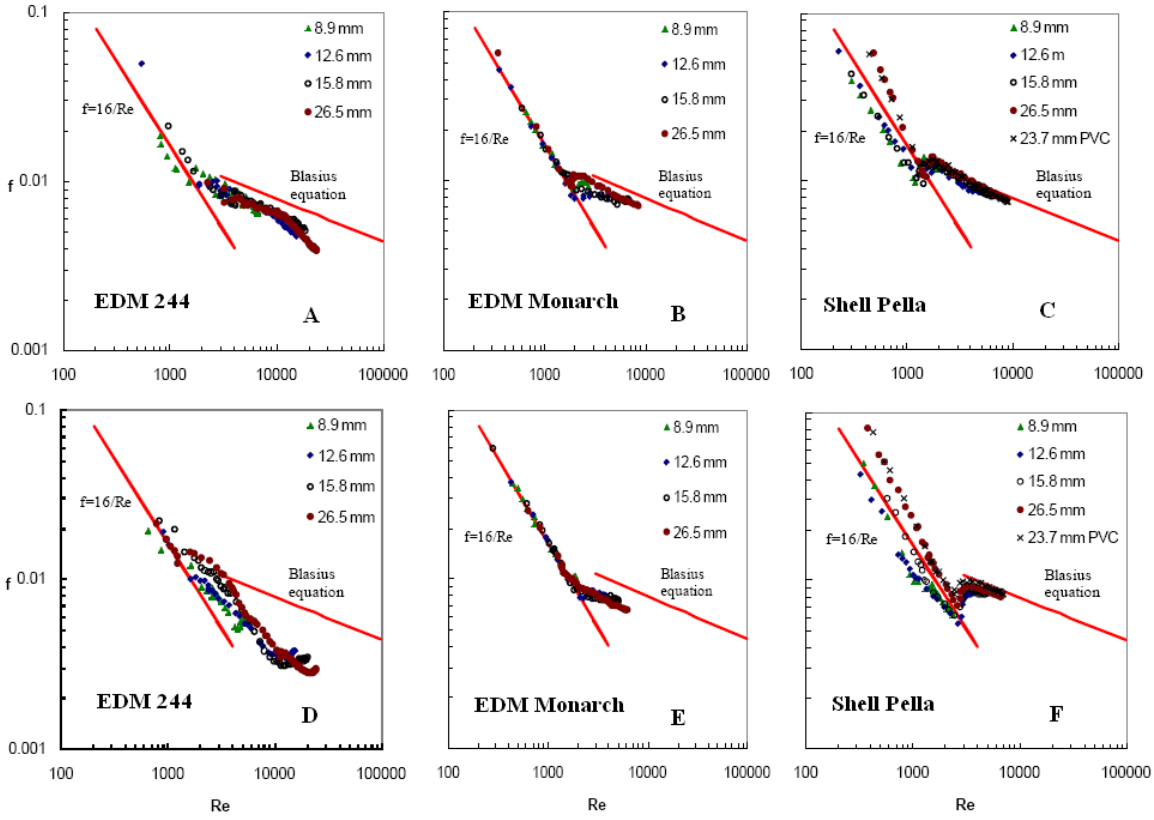

Figure 3.8: The friction factor of W/O dispersions in horizontal pipes by *Omer* (2009). μ_m is based on the laminar regime. ϕ_d = 0.1 A, B and C; ϕ_d = 0.35 D, E and F.

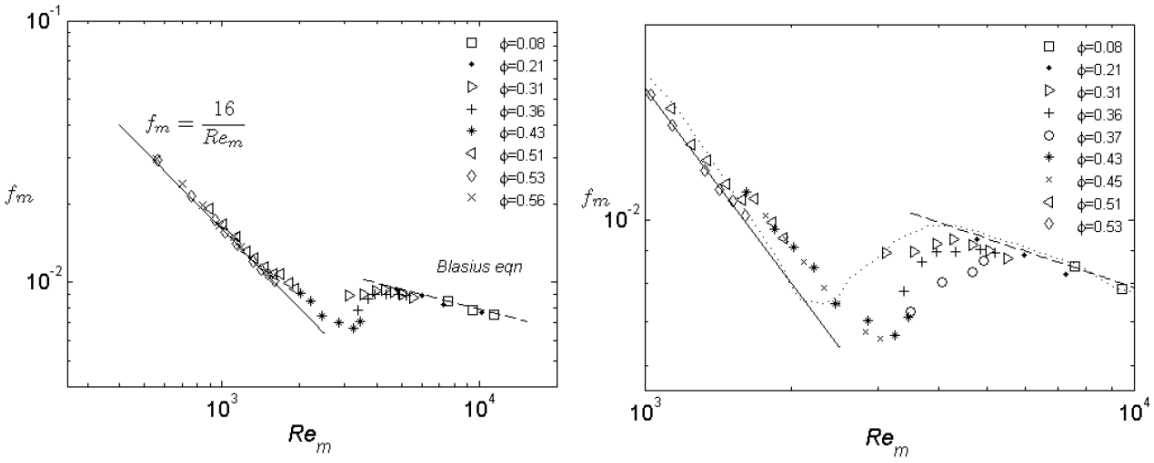

Figure 3.9: The friction factor of O/W dispersions in horizontal pipes by *Pouplin et al.* (2010). μ_m is based on Equation 3.10. Right plot is a zoom into the transition region.

Table 3.2: Literature summary of unstable liquid-liquid pipe-flows that include fully dispersed flows

Reference	Oil phase Viscosity [$mPa.s$]	Oil phase Density [kg/m^3]	Aqueous phase Viscosity [$mPa.s$]	Aqueous phase Density [kg/m^3]	σ [mN/m]	T_{ref} [$^\circ C$]	Dispersion type	Flow regime	U_m range [m/s]	Pipe ID [mm]	Pipe material	Pipe orientation	Mixing method
Nadler and Mewes (1997)	Shell Ondina 17 (a white mineral oil) 22, 27, 35	na	Water 1	1000	na	18, 25, 30	W/O and O/W	Turbulent	0.10 to 1.60	59	PolyMethyl MethAcrylate	Horizontal	Initially stratified streams mixing due to turbulence
Angeli and Hewitt (1998)	EXXSOL D80 1.6	801	Tap water		17		W/O and O/W	Turbulent	0.11 to 2.65	24.3, 24	Stainless steel, Acrylic	Horizontal	Oil introduced into water stream through a T-junction
Elseth (2001)	A mixture of two different diesel oils 3.6	842	A mixture of Dimethylsulfoxid and water 3.2	1101	na	20	W/O and O/W	Turbulent	0.75 to 3.00	56.3	Stainless steel with a glass section about 11% of the length	Horizontal	Mixing in an agitated tank

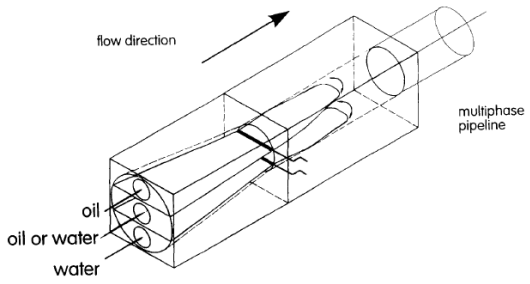

Figure 3.10: Stratified entrance section of *Nadler and Mewes* (1997)

Nadler and Mewes (1997) measured pressure drop in liquid-liquid flows that underwent emulsification as a result of pipe-flow turbulence alone, where the different phases were introduced through a stratified arrangement (shown in Figure 3.10) without any enhanced mixing or shear. A sample result of pressure drop per unit pipe length is shown in Figure 3.11 as a function of ϕ_{water}. The fully dispersed points can be seen by referring to Figure 2.3. *Nadler and Mewes* (1997) found that for all investigated cases of fully dispersed flows pressure drop per unit pipe length increased with increasing ϕ_d.

Angeli and Hewitt (1998) compared pressure drop of dispersed oil-and-water flows in acrylic and stainless steel pipes, where the oil phase was introduced into the water phase through a T-junction. Results of normalized pressure drop to single-phase oil flow are shown in Figure 3.12 for two different U_m. Increasing ϕ_d results in a decrease in pressure drop for both O/W and W/O flows, for both pipe materials, although each at a different degree. There is one exception where a relative increase takes place in the stainless steel pipe O/W flow before the phase inversion point.

Elseth (2001) used a special formulation of refractive-index-matching liquids. The range of flows investigated was not entirely fully dispersed, only those of $U_m > 1.5\ m/s$ were. Figure 3.13 shows the pressure drop results normalized by the pressure drop of oil at the same U_m. For $\phi_{water} > 0.5$ and $\phi_{water} < 0.2$ of the fully dispersed flows, the pressure drop at each ϕ_{water} and for all U_m seems to be scaling pretty linearly with the corresponding pressure drop of single phase oil. This indicates a Newtonian behavior, and increasing μ_m with increasing ϕ_d. However, for $0.2 < \phi_{water} < 0.5$, which includes the phase inversion

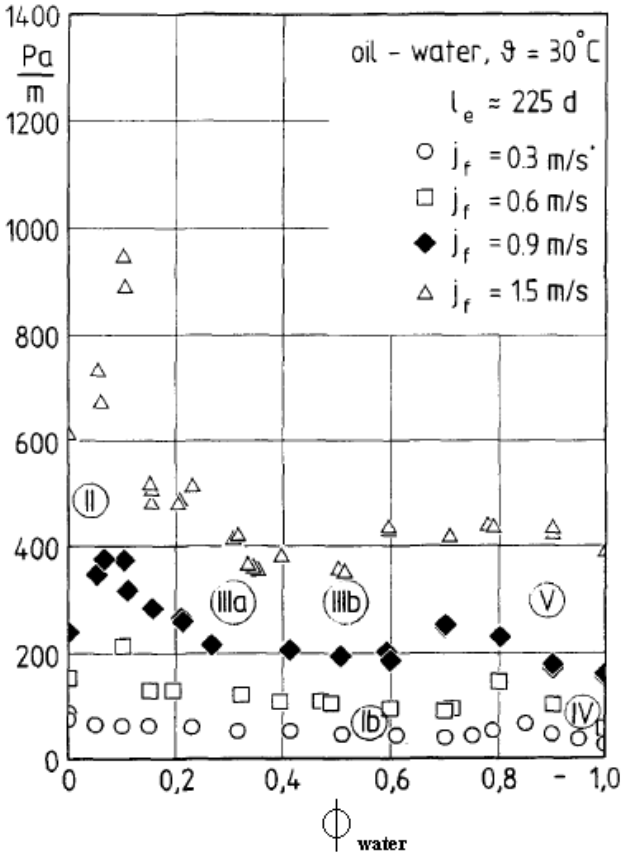

Figure 3.11: Pressure drop per unit length as a function of ϕ_{water} at different U_m by *Nadler and Mewes* (1997).

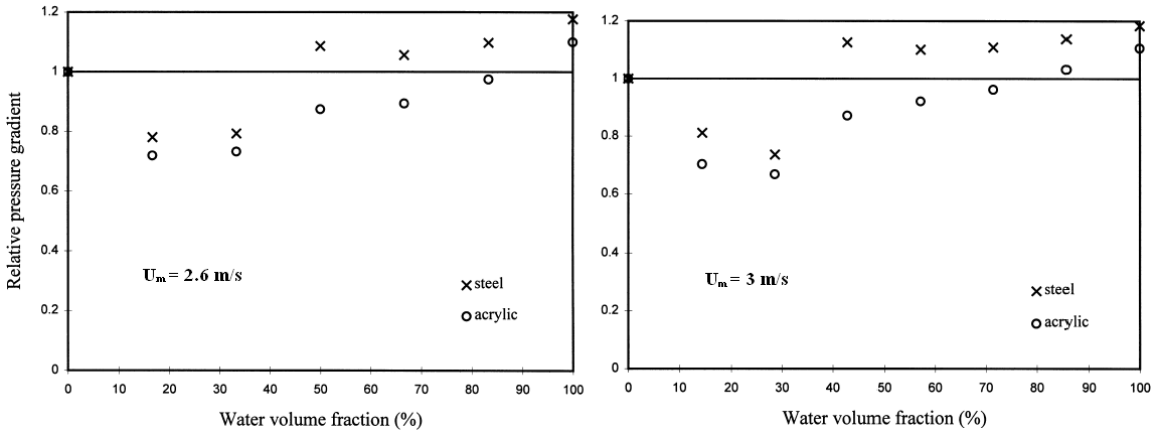

Figure 3.12: Normalized pressure drop for fully dispersed flows as a function of ϕ_{water} by *Angeli and Hewitt* (1998).

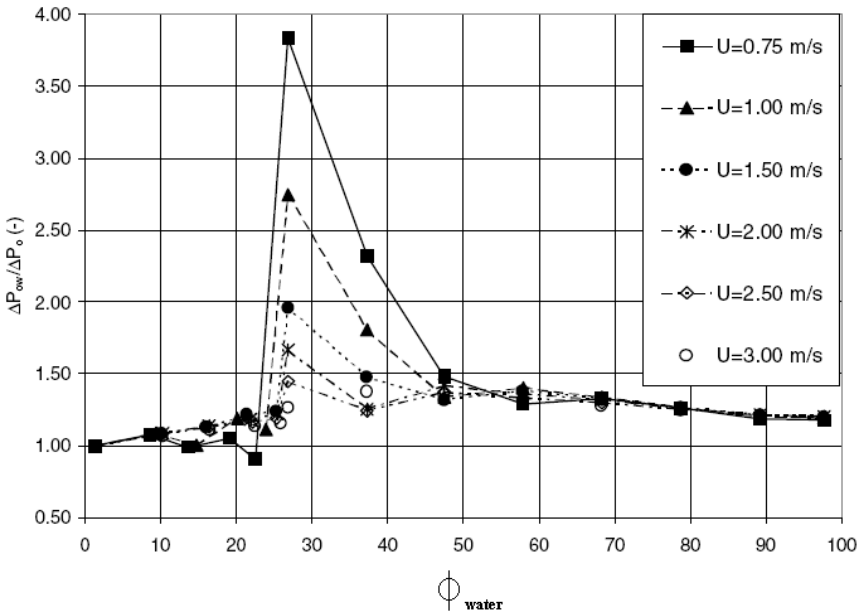

Figure 3.13: Relative pressure drop of dispersions in horizontal pipes as a function of ϕ_{water} and U_m by *Elseth* (2001).

point, it seems that some non-Newtonian effects might be present. However, it is difficult to pinpoint this, because the flow in that region is less homogeneous in its dispersiveness according to *Elseth* (2001).

3.1.3 Summary of Literature on Pressure Drop

In this section a body of relevant experimental works were examined on their findings of friction factor, and the methods they utilized to determine apparent viscosity. Notable difference in data analysis exist between different works.

Faruqui and J. (1962); *Cengel et al.* (1962); *Ward* (1964) analyzed turbulent flows of dispersions and assigned apparent viscosities without reference to the laminar regime of those dispersions. Comparison was made to the Blasius equation. They all found an increase in apparent viscosity with increasing dispersed phase ratio (except for a non-homogeneous flow by *Ward* (1964)), with all friction factors of dispersions being higher than the friction factors of the continuous phase when compared at Re_c.

Pal (1987); *Omer* (2009) compared both laminar and turbulent regimes simultaneously. They both found increasing friction factors compared to the continuous phase on the basis of Re_c for laminar flows. *Pal* (1987) found decreasing friction factors for W/O turbulent flows, and increasing for O/W turbulent flows, again compared to the single phase flow on the basis of Re_c, which *Omer* (2009) found both increasing and decreasing friction factors for W/O flows, depending on the type of oil. Their analysis assigned the apparent viscosity based on comparing the laminar regime to the Hagen-Pouseuillle law to both the laminar and turbulent regimes.

Pouplin et al. (2010) found increasing friction factor for both laminar and turbulent flows. The apparent viscosity obtained from velocity profile measurements matched the model of *Krieger and Dougherty* (1959).

A number of other investigators examined flows under a range of different conditions that would create liquid-liquid dispersed flows, but not necessarily pseudo-homogeneous in structure, and without covering full flow ranges, as the flows shift from fully dispersed to other types depending on flow conditions. These less consistent conditions from the point of view of liquid-liquid dispersed flows, gave results that were also rather difficult to fit to a basis of comparison.

In conclusion, we can state that the majority of flows in the laminar regime behaved Newtonian, always with increased friction factors compared to the single phase case. However, non-Newtonian behavior as well as decreasing friction factors were observed in the turbulent regime.

3.1.4 Turbulent Drag Reduction

As mentioned earlier, the drag behavior of dispersions has been attributed in some cases to both static and dynamic characteristics of the dispersed phase. It is important, therefore, to try and determine the size and shape of the droplets of dispersed fluid. After putting in perspective the findings of different investigators, it is appropriate in this light to introduce

the concept of turbulent drag reduction. The definition of drag reduction varies depending on the application. It is encountered in polymer chain additives that reduce the drag of solvents, in mass injection in boundary layers, in gas-liquid flows and other applications. Literature does not provide a clear and direct definition of drag reduction for liquid-liquid flows. The concept most widely adopted is that presented by *Pal* (1993), where he describes turbulent drag reduction in liquid-liquid dispersed flows to happen when the friction factor of the turbulent liquid-liquid flow at a certain Re_m, calculated at an apparent viscosity based on the laminar flow of the same liquid-liquid flow, is smaller than the single phase friction factor at a Reynolds number $Re = Re_m$. This definition does not make comparison on the basis of required work to obtain a certain mass flow rate, as many of the other common definitions do (*Kane*, 1990), mainly because of the engineering interest in liquid-liquid dispersed flows in pipes and tubes which are usually not engineered for drag reduction at high dispersed phase ratios. However, a comparison on the basis of Re_c would be close to a mass flow rate based comparison, especially when ρ_c and ρ_d have close values. In ChapterVI the mechanisms of drag reduction will be discussed for an Re_m based comparison.

3.2 Drop Size Measurement in Pipe Flows

Different methods have been utilized for the drop size distribution measurement of unstable liquid-liquid dispersions. The majority of those measurements have been made in stirred vessel studies. Reviews of these techniques are given by *Rajapakse* (2007) and *Maass et al.* (2008).

Indirect measurement techniques usually utilize the transmittance or the scattering of waves (ultrasound or electromagnetic). Ultrasonic waves for the determination of emulsion droplet sizing have been used since the 1970s. An outline of the theory is given by *McClements and Coupland* (1996). Some of the limitations of the method come from the spherical droplet, and no droplet-to-droplet interaction assumptions in the theory, which limits the applicability to low shear rates and rather low concentration limits (rarely reaches

a maximum of ϕ_d between 0.2 and 0.3 but usually limited to a few percent, see *Richter et al.* (2007)).

Light transmittance methods rely on the attenuation of a light beam caused by the reflection, refraction or diffraction by the particles. These methods are versatile for different liquid-liquid systems but are limited to drops larger than 0.1 mm in diameter due to excessive scattering of light by smaller particles (*Eckert et al.*, 1985). Laser diffraction methods for particle sizing (based on the Fraunhofer diffraction) are limited to a few percent dispersed phase concentration, some of the commercially available units have been tested against other methods and found to give varying results (*Simmons et al.*, 2000).

Laser light backscattering is one of the few techniques that has been shown to give a droplet size distribution in dispersed liquid-liquid pipe flows over a varying range of droplet sizes, from tens of microns to more than one millimeter, and high concentrations of up to $\phi_d = 0.42$ (*Simmons and Azzopardi*, 2001). The technique gathers laser light that is backscattered from particles, where laser light passes through a circular rotating eccentric lens, and then focuses the collected light in front of a final lens/window that separates the measurement system from the a dispersed flow (Figure 3.14). As the eccentric lens rotates at a known rate, the focused beam spot rotates and when it intercepts a droplet, the backscattered signal is detected back in the probe; since the beam may intercept droplets at any angle only a chord length can be calculated by measuring the duration of the backscattered signal. The details of the system's optical setup arrangement are described in the patents by *Schwartz and Braun* (1999) and *Hamann* (2002). The random droplet chord length measurements require significant processing to yield droplet diameter distributions. *Simmons et al.* (1999) provides some of the mathematical basis for solving the inverse problem of obtaining a droplet size distribution from a known distribution of a large number of chord length measurements. The devices that utilize laser backscattering are commercially developed, and the software they use to obtain distributions is proprietary.

The methods that rely on surfactants or dispersion stabilizers are not suitable for our

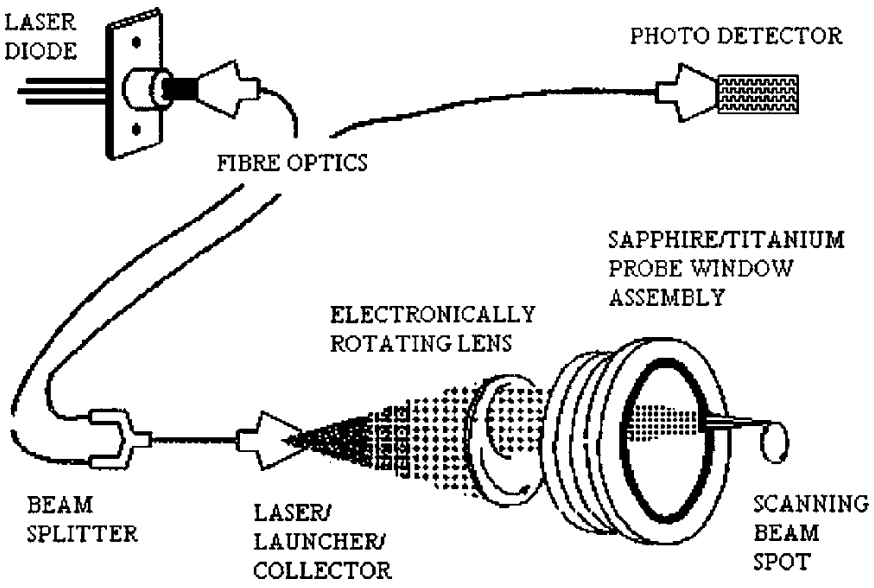

Figure 3.14: Setup of the laser backscatter particle detection technique from *Simmons et al.* (2000).

purposes since the system of our interest is fully unstable and no surfactants can be used. The methods that depend on sampling are not suitable either. Sampling methods have yielded good results for very low ϕ_d (*Karabelas*, 1978) where coalescence is negligible during the flow. However for $\phi_d \geq 0.1$ the sample extraction process, no matter how carefully done will result in coalescence and an alteration in the droplet size distribution when applied to a fully unstable liquid-liquid system. Also, any surfactant or stabilizing agent used on the sample, to freeze the sample can cause further breakup or can be very difficult to apply rapidly enough to prevent coalescence. Therefore, these methods will not be reviewed here.

3.2.1 Photographic Imaging

The direct and most accurate way of obtaining droplet size information is through photography, where an image of the droplets can be obtained that can be approximated as instantaneous. Results will be confined to the region of the flow where the images are taken. The main condition for achieving accurate size information is the correct interpretation of images. The challenge of photographing unstable liquid-liquid flows resides in the fact that

photographs of fairly small droplets, on the order of few microns need to be taken when the mixture velocity is on the order of a few meters per second. This means that at the high magnification rates required, the imaging system should be able to collect all the necessary information in durations on the order of a few microseconds or hundreds of nanoseconds. For instance, a spherical drop 10 microns in diameter moving at a speed of 3 m/s will move 10 microns within 3.33 microseconds. Therefore to freeze the motion of such a droplet (i.e. not get a blurred image) either the camera exposure time or the flash duration should be less than 3.33 microseconds. This requires high-power, short duration flash lights. The high magnification of the optical system is not the only reason for high intensity light; in addition the presence of a large number of droplets in the dispersion creates a highly light dispersive system, which gives the direction of the illuminating flux with respect to the camera aperture a special importance. Below are summarized relevant literature cases on the photographic (direct) imaging of unstable liquid-liquid flows.

One of the most relevant cases is by Ward (*Ward*, 1964; *Ward and Knudsen*, 1967). Figure 3.15 shows the portion of the pipe that was modified to accommodate the photographic setup, including a microscope with a camera focused right behind the window on the pipe wall. Illumination was provided through a flash light channeled through a glass rod that penetrated the pipe up to 2 to 5 mm from the opposite wall, thus providing enough path length through the opaque dispersion to have an effective illumination.

Droplets were photographed for total concentrations up to $\phi_d = 0.492$ (with the near wall concentration being about 99% of the total bulk). Figure 3.16 shows sample pictures obtained by Ward. The setup was able to measure droplets as small as few microns in diameter. The main disadvantage of this setup is the intrusive rod with a diameter on the order of the pipe diameter. Ward cross checked the results obtained through this setup with another that had a contracting cross section such that its thin neck allows enough light to transmit across, without any bluff intrusive elements. Naturally, a necking flow of this kind accelerates and shears the flow. The comparision results had some discrepancy.

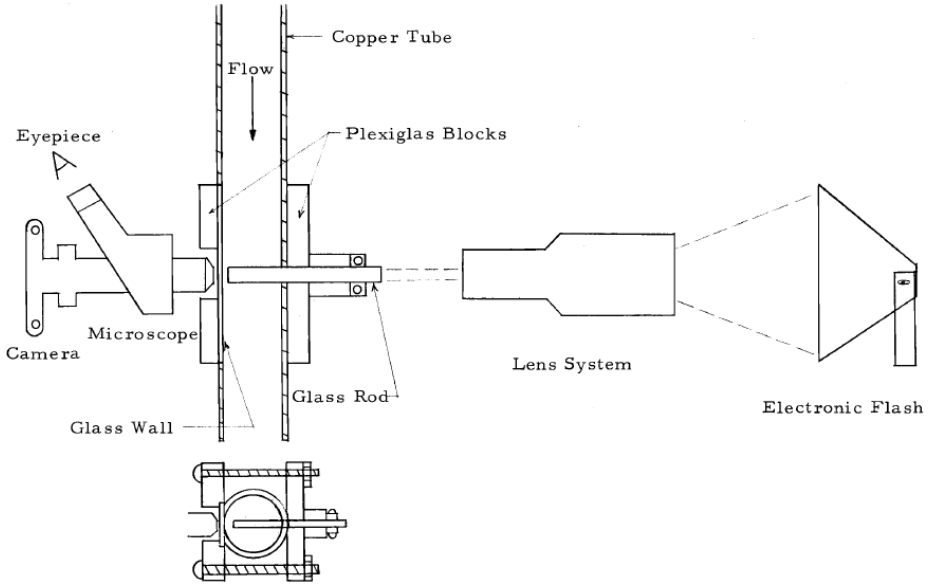

Figure 3.15: Photographic setup of *Ward* (1964).

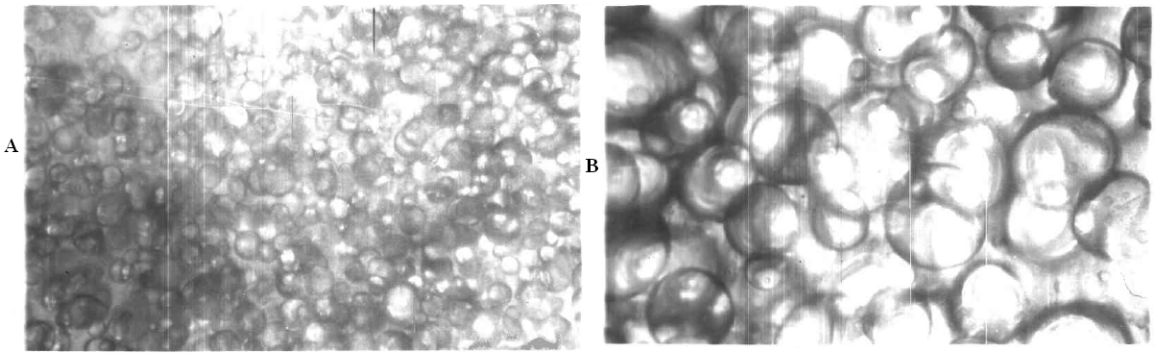

Figure 3.16: Droplet images of Shell Solve 360-in-water obtained by *Ward* (1964). (A) U_m = 1.77 m/s, ϕ_d = 0.196; (B) U_m = 3.44 m/s, ϕ_d = 0.492.

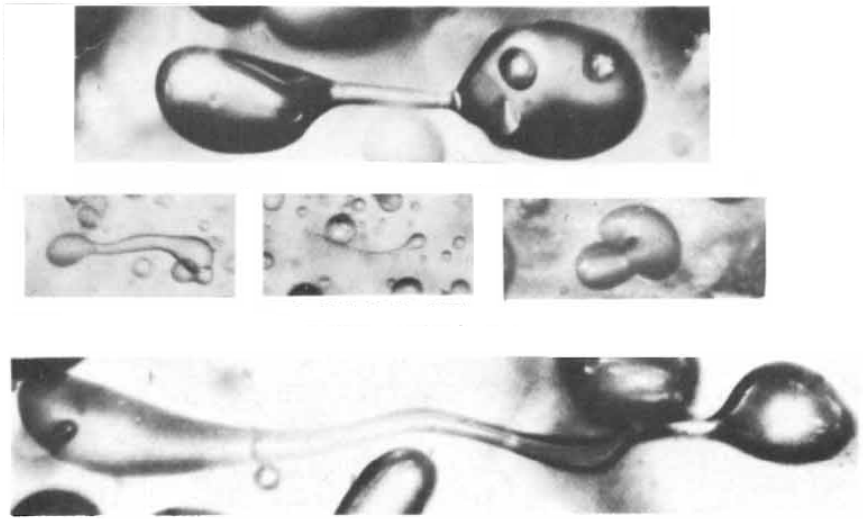

Figure 3.17: Droplet images obtained by *Collins and Knudsen* (1970).

Collins and Knudsen (1970) measured droplet size in turbulent flow. The experiment was set up such that the major mechanism of droplet breakup was turbulent flow and not a high shear region like a pump or nozzle. The dispersed phase was introduced through a jet nozzle into the pipe-flow of the continuous phase, the dynamics of the jet breakup was the initial mechanism of generating the drops which were then subsequently broken up due to pipe turbulence in the 19.05 mm ID pipe. Imaging the droplets was done through the walls of the pipe which were fitted with transparent sections of glass. The low dispersed phase concentration $\phi_d \leq 0.1$ allowed probing different depths of the pipe through the window by changing the depth of the focal plane. A flash of a duration on the order of 1 microsecond was able to freeze droplets moving with velocities up to $U_m = 6.096\ m/s$. Figure 3.17 shows some of the photographs obtained by *Collins and Knudsen* (1970). The smallest measured droplets were on the order of 20 microns.

Karabelas (1978) employed a photographic setup and a test facility similar to *Collins and Knudsen* (1970) with a pipe ID of 50.4 mm. Karabelas used a sampling method in conjunction with the in-line photographic technique. The sampling method was concluded to give more reproducible and better fitting results, possibly due to difficulties in interpreting and measuring all the droplets in the photographs of the non-sampled method. The

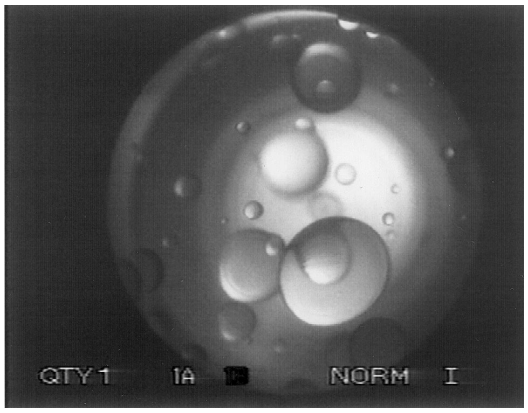

Figure 3.18: Droplets from an O/W flow in an acrylic pipe by *Angeli and Hewitt* (2000a).

smallest and largest observed droplets (0.1 to 5 mm) by Karabelas were respectively an order of magnitude larger than the smallest and largest droplets observed by Collins and Knudsen (10 to 800 microns). *Karabelas* (1978) found that the droplet size distribution at a sufficiently far downstream location (about 600 pipe diameters) could be described by an upper-limit log-normal or a Rosin-Rammler distribution function. Karebelas showed that presenting the drop side data of *Collins and Knudsen* (1970) like his data, in cumulative volume fraction, would allow it to be described by similar distribution functions.

Angeli and Hewitt (2000a) used an endoscope to measure drop sizes in the same facility of *Angeli and Hewitt* (1998) mentioned above. The 7.9 mm diameter endoscope was mounted at 45° to the flow, and could traverse the radius of the pipe. The endoscope window was positioned to the side (had a 90° direction of view). Illumination was provided from the opposite direction of the endoscope window, and the focal distance was a maximum of 4.3 mm. Only dispersions of very low dispersed phase ratios (ϕ_d = 0.034 to 0.091) were examined. Figure 3.18 shows a sample photograph, recorded using a video camera installed at the eyepiece of the endoscope. The measured droplet sizes fitted a Rosin-Rammler distribution.

The monitoring of unstable liquid-liquid dispersions in stirred vessels faces challenges that are similar to those in monitoring unstable dispersed flows in pipes. It is instructive, therefore, to include some of the related significant findings in the stirred vessel literature.

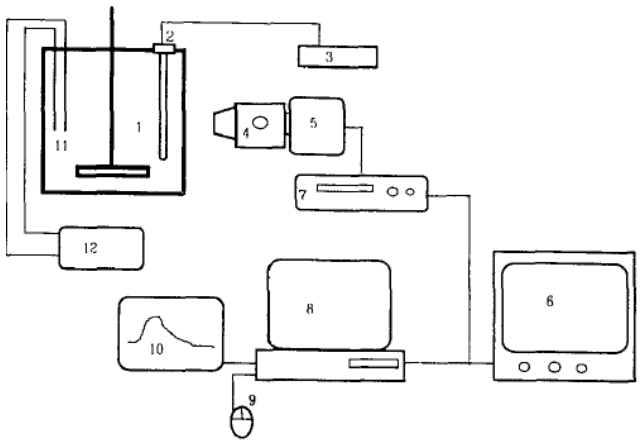

Figure 3.19: Stirred vessel imaging setup of *Pacek et al.* (1994a).

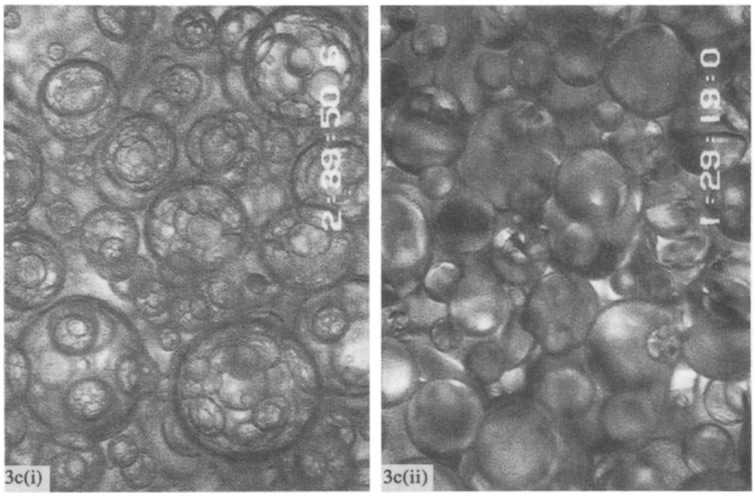

Figure 3.20: Droplet images at $\phi_d = 0.45$ by *Pacek et al.* (1994b). 3c(i) O/W/O, 3c(ii) O/W.

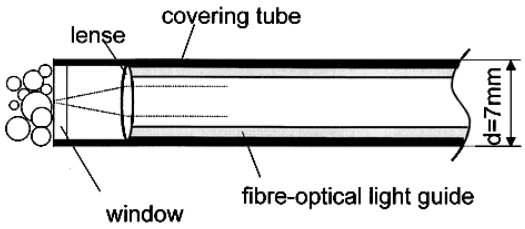

Figure 3.21: Endoscope setup of *Ritter and Kraume* (2000).

Pacek et al. (1994a) used a stereo microscope-video camera combination to obtain photos through the walls of a stirred vessel. The microscope was focused into the dispersion around 4 mm from the vessel wall. The setup is shown in Figure 3.19. Light from a strobing flash was delivered into the dispersion, behind the wall facing the microscope-camera combination, though a glass well. The distance between the glass well and the wall was varied from 2 to 8 mm. Freezing the flow was achieved through the short flash, but its duration was not mentioned. The smallest drops analyzed were about 40 microns. The setup was remarkable for its ability to operate under any dispersed phase ratio. Sample images from this setup as published in *Pacek et al.* (1994b) are shown in Figure 3.20.

Ritter and Kraume (2000) used an endoscope with a straight view direction. Illumination was provided through a light guide surrounding the endoscope, and the whole assembly was housed in a 7 mm tube to provide a transparent distance between the endoscope lens and the focal plane. The assembly is shown in Figure 3.21. Images were captured by a Charge Coupled Device (CCD) camera. The smallest measurable droplet was claimed to be 30 microns, but measured results in plots showed droplets down to only 100 microns. The flash speed was 5 microseconds, allowing the freezing of up to 1 m/s flows with less than 10% blurring. Dispersed phase concentrations of up to $\phi_d = 0.5$ were able to be photographed. Figure 3.22 shows a sample photograph of droplets. An important source of error was the endoscope's relatively high depth of focus, which results in about ±10% descrepancy of the measured drop diameter, depending on its position within the depth of focus.

Lovick et al. (2005) also used an endoscope-camera combination with lighting from the

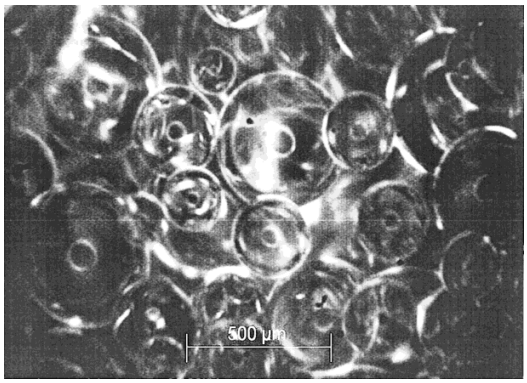

Figure 3.22: Droplets photographed at $\phi_d = 0.5$ by *Ritter and Kraume* (2000).The center circles are optical reflections of the light source.

opposite end of the viewing window, but their system was limited to $\phi_d = 0.1$.

The commercially developed device described in *Reed et al.* (1998) has been, to date, the most successful method of in-situ imaging of multiphase systems. The success of the device is manifested in image resolution/quality, smallest measurable droplets, and dispersed phase concentration at which a photograph can be taken. The device consists of an imaging probe connected to a camera and a light source. Figure 3.23 shows a schematic diagram that describes the concept of the probe. The focal point of the system is at or near the window (1), which is in contact with the multiphase flow. Illumination is provided from the inside periphery of the probe delivered through fiber optic cables from diode laser (or other sources). Backscattered light from droplets at the focal point is transmitted through a system of lenses, in the center of the probe, that magnify the image and project it onto a sensing device like a CCD camera. Figures 3.24 and 3.25 show sample images photographed using the Particle Vision Microscope (PVM)®, a commercial version of the probe, manufactured by Mettler Toledo®. Although this system is superior to the other imaging methods reviewed above, it still suffers some drawbacks. The outer diameter of the probe is 19 mm, and it has to be immersed in the conduit, with the window facing the incoming flow at an angle (*Reed et al.*, 1998). This means that it cannot be used in relatively small conduits nor in cases where disrupting the flow is not an option. Another drawback is the reflection of the illuminating light sources on the droplets. These reflections show up

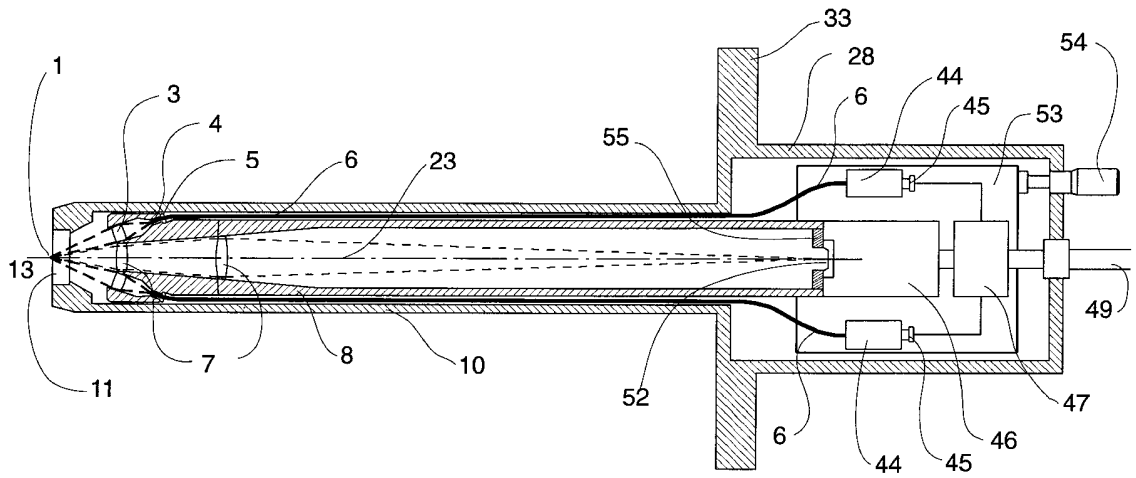

Figure 3.23: A diagram describing the principle of the PVM® probe (*Reed et al.*, 1998).

as concentric circles and can create difficulties for image processing; the proposed solution to this problem is using a reflecting Teflon surface situated 4 to 6 mm from the end of the probe. Unfortunately, this solution creates further intrusion into the flow. The photograph in Figure 3.24 is taken with the reflecting Teflon surface, and the photographs in Figure 3.25 are taken without it.

3.2.2 Conclusion

A review of the methods used to obtain the size distribution of droplets in liquid-liquid dispersed flows has shown that a few have been only relatively successful. Laser light scattering and direct imaging have been able to provide droplet size measurements with varying accuracy at high dispersed phase concentrations, with small droplets and in fast flows. Direct imaging is more accurate than the light scattering method, and can give comprehensive description of the droplets. However, many challenges remain in obtaining high-quality, high-resolution images at high dispersed phase concentrations of drops smaller than 50 microns moving at process speeds of a few meters per second or more, all without causing disruption to the flow conditions. Later in this dissertation are shown representative photographic images obtained using the best practices described above in a flow without disruptions.

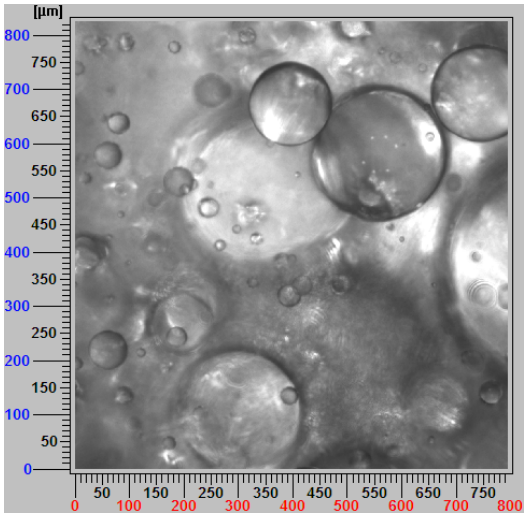

Figure 3.24: A sample photograph of droplets in an agitated vessel obtained using the PVM® with the reflector cap (Image from Mettler Toledo® brochure).

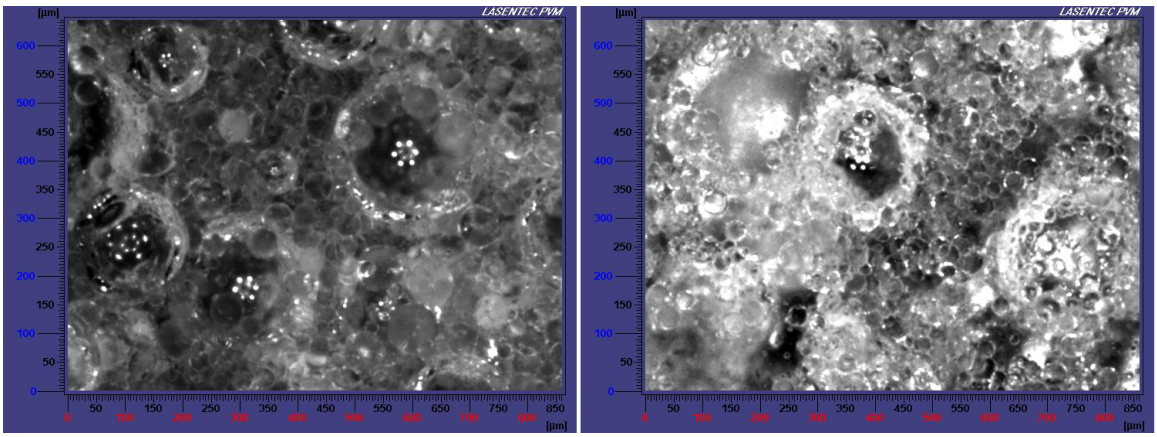

Figure 3.25: Droplets of Polystyrene emulsion in an agitated vessel, after different mixing durations; photographed using the PVM® (Image from Mettler Toledo® brochure). The dots of circular pattern on the droplets are reflections of the light sources.

Figure 3.26: The reflector cap of the PVM® for reducing light reflectance from droplets (Image from Mettler Toledo® brochure).

CHAPTER IV

Experimental Setup

The experimental setup described in this chapter includes the flow rig which was designed and constructed at the University of California, Irvine to simulate part of the fuel supply line of a gas turbine engine that uses water mixing with fuel for the reduction of pollutant emissions. This chapter will also describe a photographic arrangement that enables in-situ droplet size measurement in the experimental rig.

4.1 Liquids of Experimentation

Silicon oil and tap water were used as the two liquid phases. Tap water was chosen as the aqueous phase instead of deionized water. Both are used in industrial setups, but tap water is less corrosive and has lower impact on pumps, valves and sensors in the system. Silicon oil was chosen to mimic kerosene which was not used for safety reasons. The silicon oil was a PolyDiMethylSiloxane (PDMS) manufactured by Clearco®. The molecular structure of PDMS is shown in Figure 4.1. The longer the chain, the more viscous the oil. The viscosity of the oil specified by the manufacturer was 5 centiStokes.

Table 4.1: Physical properties of the experimental liquids

	Density $[\frac{Kg}{m^3}]$	Viscosity $[mPa.s]$	Interfacia tension $[\frac{mN}{m}]$	Temperature $[^{\circ}C]$
PDMS	913.9	6.8	30.5	21.5±0.5
Tap Water	997	1.02		

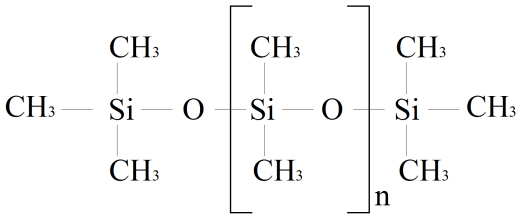

Figure 4.1: The molecular structure of PDMS.

However, measurements using an Anton-Paar Physica MCR301® rheometer showed the viscosity of the oil to be 6.8 centiStokes (See Appendix B). The density of the oil was measured and found to be 913.9 kg/m^3, which was similar to the value specified by the manufacturer. The interfacial tension between tap water and the oil was measured using a pendant droplet image fitting method (See Appendix B). A summary of the physical properties of the oil is shown in Table 4.1.

4.2 The Flow Rig

A flow rig was constructed to replicate the process of mixing water with fuel in an industrial scale gas turbine. A schematic diagram of the rig is shown in Figure 4.2. Oil is stored in tank 1 and water is stored in tank 2, each is a full-draining 60-gallon drum equipped with a vortex-breaker at the bottom to prevent air from being sucked into the line. The oil is pumped by a Parker-Hannifin® H62-AA1B gear pump, while water is pumped by an AR NorthAmerica® XWLA13G15N reciprocating plunger-type pump with 3 plungers. The water pump was also equipped with a Pipeguard® pulsation dampener. Downstream of each pump a Stra-Val® N1508 relief valve is installed to safeguard against pressure surges. Since both pumps are positive displacement pumps, mass flow rate is controlled through a return loop after each valve that pumps back some of the flow to the storage tank of each liquid. Since the pressure in the test section is expected to vary due to the addition or removal of different components, and due to the varying supply rate of each liquid to achieve different ϕ_d, the mass flow rate in each return loop is controlled using a Flo-Miser FM75®

flow rate controller valve manufactured by Custom Valve Concepts®. These flow control valves allow a constant flow rate to be discharged back into the storage tank independent of the upstream pressure. The oil and water flows headed to the test section are metered using FTB-904 ball-bearing turbine flowmeters manufactured by Omega®, each flowmeter was calibrated by Omega® for the viscosity of the fluid it meters.

The oil and water are mixed in a tee-junction assembly manufactured by Parker-Hannifin®, referred to as number 3 in Figure 4.2. The tee-junction assembly is shown in Figure 4.3, oil enters from the left and water enters from the top, and the mixture leaves the tee-junction from the right. The tee-junction contains two check-valves (Model # CBG8L), one upstream of the mixing point on the water side, and one downstream of the mixing point on the mixture side. A schematic diagram of these check-valves is shown in Figure 4.4. The inlet and outlet connections of the tee-junction are 5/8" Parker A-Lok tube connections. Welded 316 stainless steel tubing is used with an inner diameter of 14.75 mm. The length of straight tube on the oil inlet side of the tee-junction is 32 tube IDs and on the water side is 6 tube IDs, the reason for the difference is the check valve that is located on the water side. Downstream of the tee-junction comes the pipe-pressure-drop test section which is a continuous horizontal section of the tubing. It consists of an entrance length of 28 tube IDs, a test portion length of 1.543 m (104 tube IDs) along which the pressure drop is measured, and an exit length of 14 tube IDs. Pressure drop is measured through ports made of 304 stainless steel tubing of 6.35 mm OD and 2.1336 mm ID welded flush to the main tube walls. Pressure drop is measured using a PX771A differential pressure transducer manufactured by Omega® and calibrated in-house over a range of 0 to 117000 Pascal with a resolution of 7 Pascals. The pressure transducer is connected to the ports using flexible tubing, filled with oil all times.

Downstream of the pipe-pressure-drop test section is a safety screen assembly, referred to as number 4 in Figure 4.2. Safety screens are used to protect the fuel injectors of gas turbines from relatively large debris that might accidentally arrive from upstream, origi-

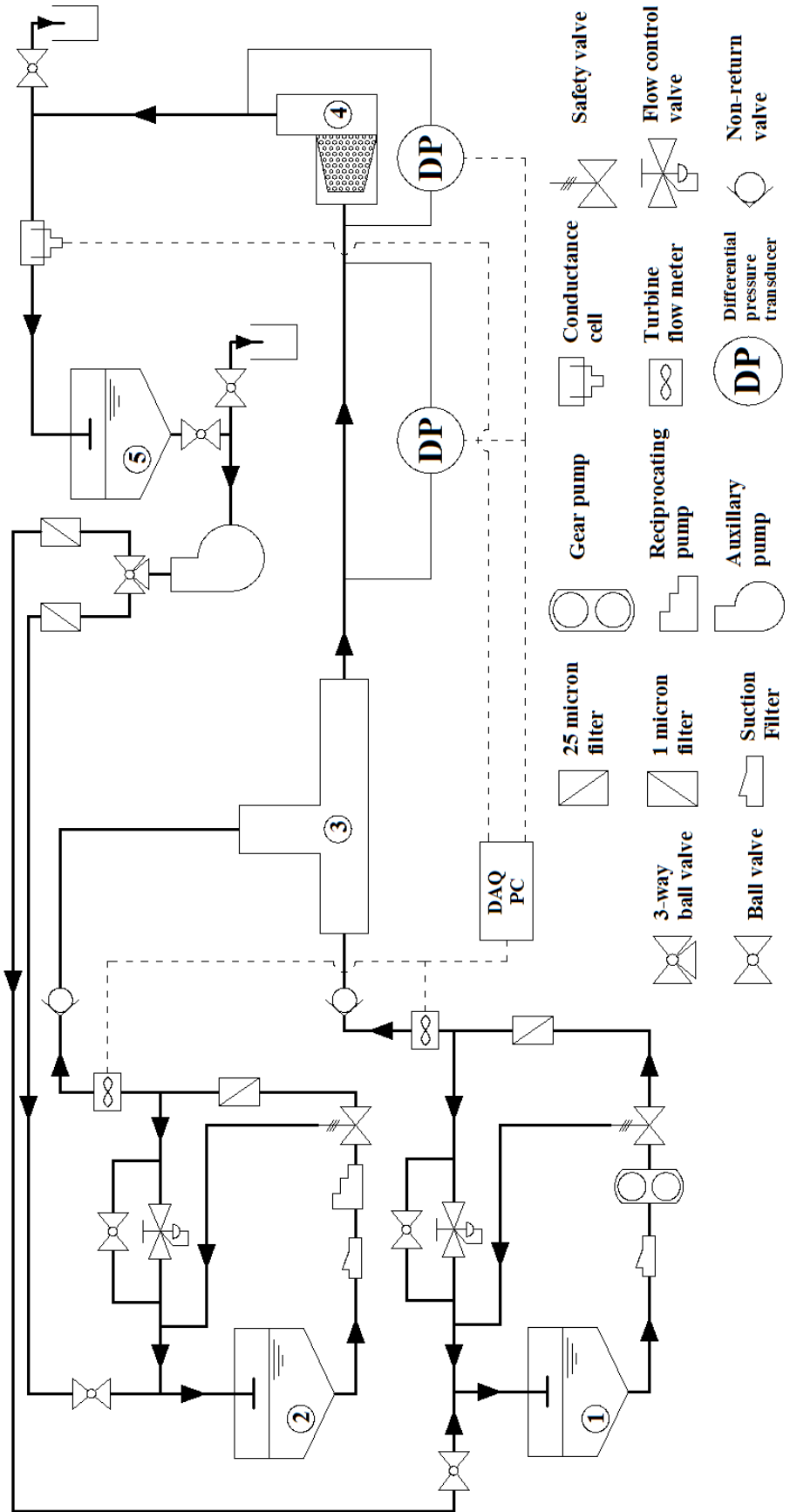

Figure 4.2: The flow rig.

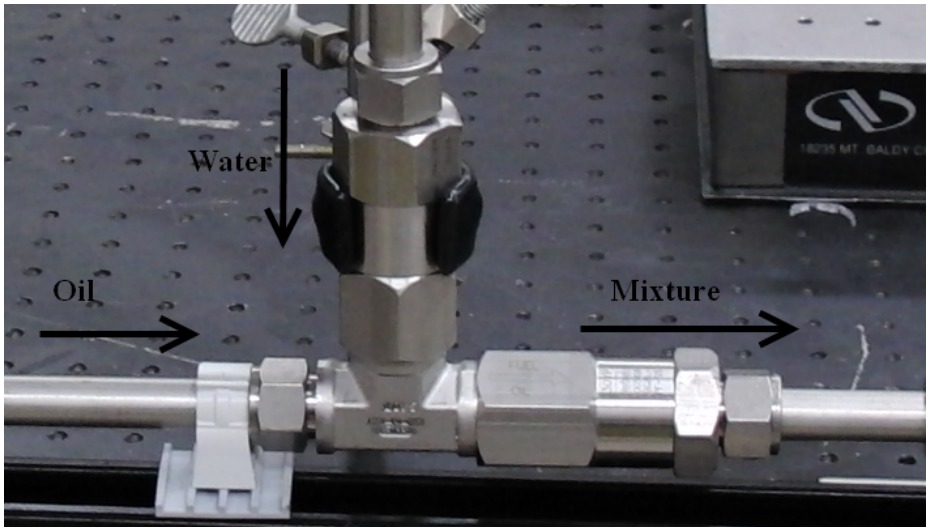

Figure 4.3: The tee-junction.

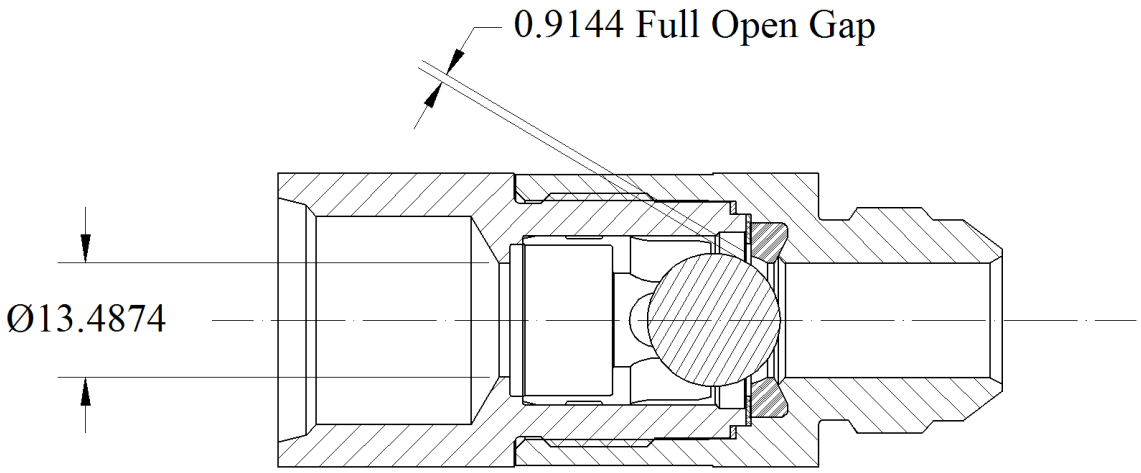

Figure 4.4: Diagram of the check-valve in the tee-junction. The smallest gap at fully open valve is shown. Dimensions are in mm.

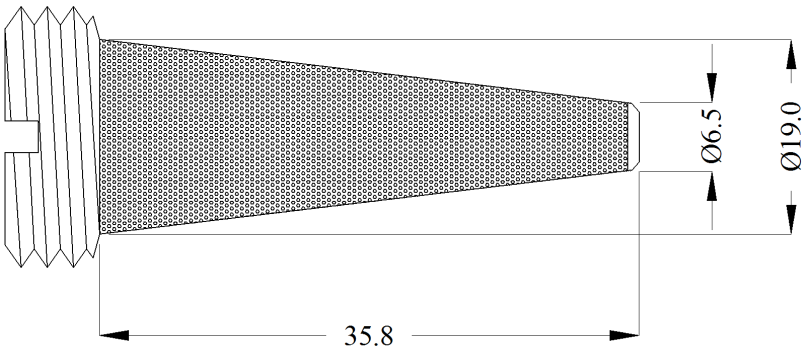

Figure 4.5: Diagram of the safety screen. Dimensions are in mm.

nating from points downstream of the last filter, or due to the failure of filters. The safety screen studied in this dissertation is a Lee Hi-Bar Screen model # FSHB2203115M made of stainless steel by The Lee Company®. A schematic digaram is shown in Figure 4.5. The safety screen has 14805 holes of 150 micron diameter, constituting a 19% open-to-total area, where the total area is 1400 mm^2.

The safety screen is held in an L-shaped housing made of stainless steel, shown in Figure 4.6. The tubes going in and out of the housing are connected by welded joints. The safety screen-housing combination creates a complex geometry for the flow to go through. The flow of liquid-liquid dispersed flows through pipe fittings and elements of complex geometry is rarely addressed in the literature, and never before addressed for a safety screen. Therefore, the pressure drop across this complex geometry is measured using two ports similar to those used in the pipe-pressure-drop test section, situated each at 2 tube IDs from the entrance and exit of the housing. This distance was chosen based on an estimation that the flow would be attaching back to the exit tube walls after emerging from the assembly, and a desire to minimize any effects of a change in the status of the dispersion that might occur after its emergence from the safety screen. A typical setup that would consider pressure drop through a number of consecutive ports before and after the fitting in question was not possible in this case, as the replication of the actual industrial setup did not allow enough tube length. A second pressure transducer unit, identical to the

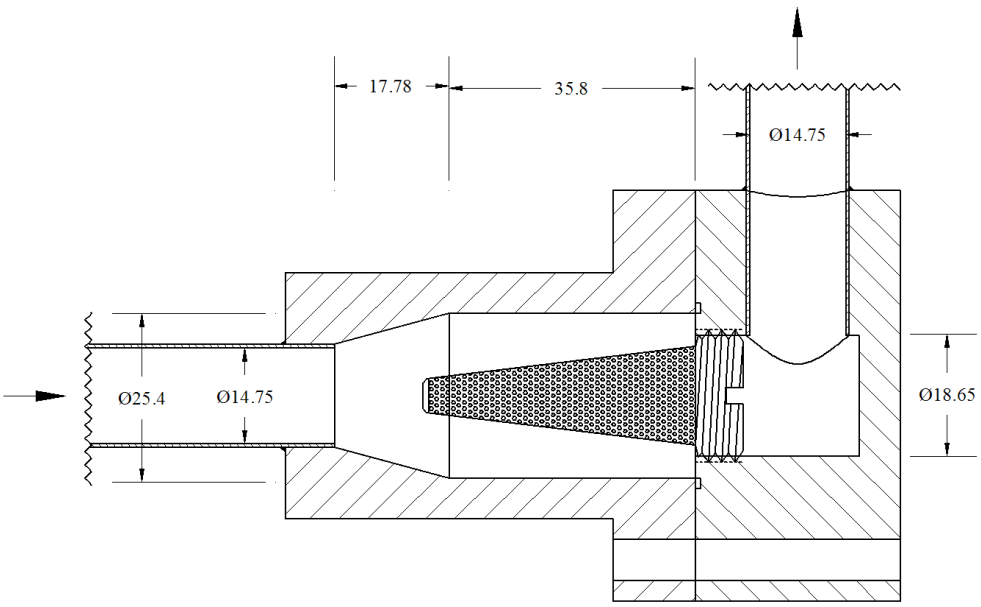

Figure 4.6: Diagram of the safety screen housing. Dimensions are in mm.

first, is calibrated for a pressure range of 0 to 138000 Pascals, due to the higher pressure drop expected from the screen-housing combination. Both the inlet and the outlet of the safety screen housing were positioned horizontally.

Downstream of the safety screen is a conductance cell, manufactured in-house, to determine the continuous phase in the liquid-liquid dispersed flow. The details of the conductance cell are described in *Jepsen* (2009). After leaving the conductance cell, the liquid-liquid dispersion is collected in a settling tank, referred to as number 3 in Figure 4.2. When the oil and water stratify in the settling tank they are pumped back to their respective storage tanks by an auxiliary pump, passing through fine filters.

4.3 Experimental Procedure

The procedure for measuring the pressure drop in the pipe-pressure-drop test section and across the safety screen assembly is as follows. The ball valve that bypasses each of the flow control valves (shown in Figure 4.2) is set to the fully open position. The oil and water pumps are turned on, first the oil pump then the water pump. Then the bypass ball

valves are slowly and simultaneously closed in order to gradually load the flow control valves. The flow rates of oil and water going to the test section are read. If any of the flow rates require adjustment, then the bypass ball valves are set back to the fully open position, the respective flow control valve that requires adjustment is adjusted and both bypass ball valves are closed back slowly in a similar manner. If any of the flow rates needs further adjustment the procedure is repeated until the desired flow rates are achieved. Once the desired flow rates are reached and are steady, the flow is allowed a few seconds to fully stabilize and then the measurements are recorded over 30 seconds on a PC. Once the measurements are taken, the pumps are stopped immediately.

The schedule for taking measurements was to span the feasible range of dispersed phase ratios for a constant flow rate, and then move to a higher flow rate. The spanning of dispersed phase ratio started for each flow rate randomly from either the lowest or highest ϕ_w for the case the moved to the successive ϕ_w.

Measurements are taken until either the water or the oil in the storage tanks runs out. The mixture is then let to separate by stratification in the settlement tank. Although the separation of oil and water starts immediately after the flow stops, the bulk of the oil and water in the settlement tank separate within 4 to 6 hours, but the smallest droplets don't separate for several days. Water droplets in the oil fully separate and segregate, however, oil droplets in the water do not separate fully, and the water is left with a cloudy appearance. The amount of oil left in the water phase is estimated to be between 0.5 and 1.5 % by volume. This estimation is made by letting samples of once used water to settle in a graduated glass tube over several months until the water became fully transparent and clear. After a minimum of 4 days from each experiment, the stratified water and oil are pumped back to the storage tanks for a new round of measurements. Water, being the denser liquid, settles in the bottom and is pumped first, the layer of water that is close to the water-oil interface is discarded, and replaced with fresh tap water.

There is no need for cooling circuits for the liquids since running times are limited. The

running time of any set of experiments, before the storage tanks are emptied, is less than 5 minutes. Stabilizing the temperature of the liquids relies on the laboratory environmental control system which keeps the ambient temperature at 21 ± 1 °C.

4.4 Photographic Setup

The difficulty of obtaining a droplet size distribution in unstable liquid-liquid dispersed flows was explained in the previous chapter, and the literature survey showed that no setup was successful in obtaining a measurement using direct imaging, without disturbing the flow. The state-of-the-art in direct imaging of dispersed systems is a commercially available, but still imperfect. Additionally, a single unit cost is on the order of $ 100k at the time of the writing of this dissertation. The following describes the method that was used for direct imaging without flow disruption.

4.4.1 Concept of the method for direct imaging

The imaging techniques reviewed in 3.2.1 used different illumination methods. Forward scattering is the most common method, since it is able to give images of good contrast, and requires relatively smaller intensity light sources. It was used, among many, by *Ward* (1964); *Collins and Knudsen* (1970); *Karabelas* (1978); *Angeli and Hewitt* (1998); *Pacek et al.* (1994a) and *Lovick et al.* (2005). When ϕ_d is relatively large, multiple scattering from the large number of droplets reduces the intensity of the forward scattered light sharply. To overcome this and still be able to directly image droplets on the order of tens of microns, the thickness of the flow region through which light has to travel is reduced (*Ward*, 1964), which is intrusive to the flow. Backscattering gives an alternative approach. *Ritter and Kraume* (2000) and *Reed et al.* (1998) used beams of light that were focused onto the plane to be photographed, and the backscattered light from those focused beams formed the image. Multiple scattering was not an issue because only the droplets that were in the plane of focus got the high intensity light. However, the problem here was the increased reflection

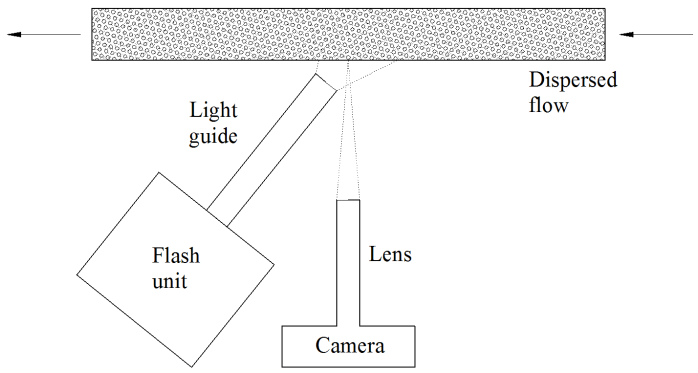

Figure 4.7: Diagram of the safety screen housing. Dimensions are in mm.

as was discussed, and the proposed solution introduces intrusiveness. Thurthermore, these methods cannot be used in small sized pipes. The concept implemented in this dissertation uses backscattered light from a diverging light beam instead of a focused one. The diverging beam is projected onto a transparent pipe section, and the backscattered light forms the image of the droplets. The drawback in this case is the loss of contrast due to the excessive amount of light that reaches the imaging plane due to multiple scattering.

4.4.2 Implementation of the direct imaging concept

The photographic setup is shown in Figure 4.7. A flash unit is used to generate a short pulse of light which is delivered to the imaging plane through a light guide in the form of a diverging beam. A microscopic lens attached to a camera and focused on the imaging plane collects the backscattered light from the droplets.

The transparent section shown in Figure 4.8 was made of a glass tube of a rectangular cross section, to provide a flat surface that allows imaging without optical distortion. The glass tube was connected to the metal tubes through two coupling sections manufactured to provide a smooth transition from one cross section to the other to minimize any disturbance to the flow. The two coupling sections were reinforced with each other through 4 metal rods. An alternative setup would be to use a transparent pipe of circular cross section with a rectangular box around it that is filled with a refractive index matching transparent

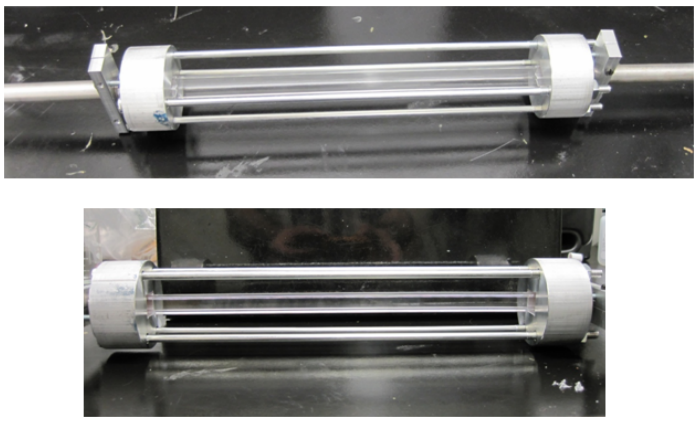

Figure 4.8: The transparent test section.

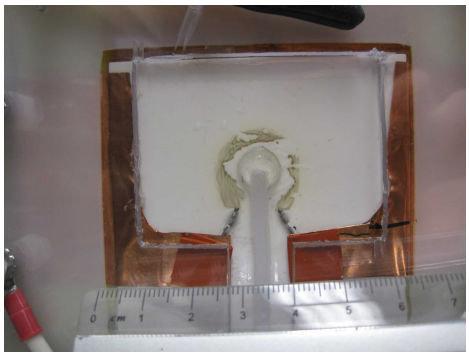

Figure 4.9: The arc of the flash.

medium. However, the rectangular tube was determined to be simpler in this case, and the flow disruption appeard to be small.

The flash is manufactured by Prism Science Works®; it is an arc discharge that has a FWHM duration of 200 to 300 nanoseconds. The arc of the flash has a horseshoe shape and is shown in Figure 4.9. The frequency of the flash is not sufficient to obtain video images, only single shots are possible. The light guide that transmits light from the arc is an optical fiber, manufactured by Lumenyte® under the name STA-FLEX™ SEL700. The diameter of the inner core is 18.8 mm. This large diameter ensures the transfer of enough light from the arc to the imaging plane.

To obtain sufficient magnification, a Navitar® 12X™ lens is used to magnify the droplets. The focal length of the lens is constant for different, selectable magnification ratios. The lens is attached to a Nikon® D80™ camera.

4.4.3 Small flow rig

A small-size flow rig was constructed to facilitate the evaluation of the photographic method. A schematic diagram of the setup is shown in Figure. It consists of a 6 liter capacity tank, connected to a centrifugal pump, after the pump is a transparent section made from a drawn glass tube with a rectangular cross section, with an internal dimensions of 1 cm x 1 cm. The connection with the rest of pipes is provided through two plastic couplings that were machined to give a smooth transition. The rest of the loop uses 1/2" NPT PVC pipes. After the transparent section the flow is simply directed back to the tank. Oil and water are added to the tank. A hand-held agitator helps keep the oil and water mixed, and as the mixture passes through the pump and flows back to the tank, it mixes vigorously and becomes a homogeneous dispersion after a few minutes of operation.

CHAPTER V

Results

5.1 Single Liquid Flow in the System

The friction factor for single phase oil and water was obtained in the pipe-pressure-drop test section in order to characterize the status of Newtonian single phase flow in the system and compare it to smooth pipe behavior in an idealized system where turbulence develops due to the flow in the pipe rather than resulting from a fitting joint. This single phase friction factor is shown in Figure 5.1 as a function of the Reynolds number. For comparison, the Blasius relationship is plotted along with the experimental data of *Nikuradse* (1933) for smooth pipes, and the points from the Colrebook relationship (Equation A.13), corresponding to the same Reynolds numbers of Nikuradse's data, with an average surface roughness of 0.624 microns. This is the roughness of the welded stainless steel tubing, provided by the manufacturer. It can be seen that for the turbulent regime there is a very good agreement between the system's measured behavior and Nikuradse's data.

A zoomed view around the transition region is shown in Figure 5.2. It can be seen that the transition starts at smaller Reynolds numbers than typical (*Nikuradse*, 1933) which are represented here through the data fit suggested by *Morrison* (2010), and in effect happens over a short range of Reynolds numbers. This is due to the fact that after leaving the check valve of the tee-junction, the flow is developed only over 28 tube IDs rather than the full distance required to ensure fully developed pipe flow. The shorter entrance distance

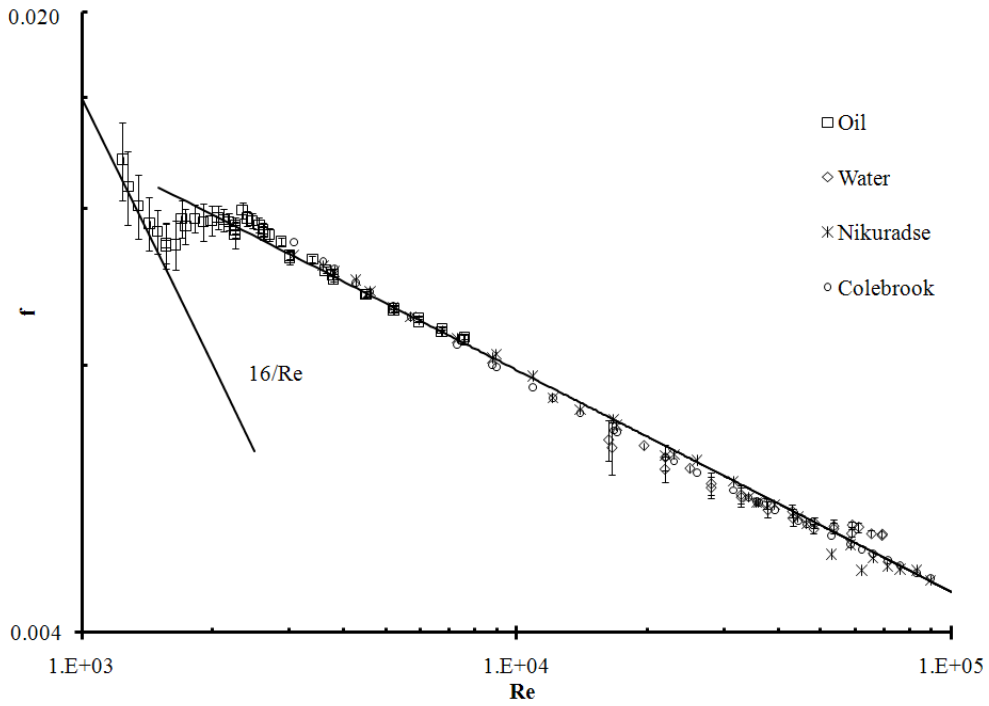

Figure 5.1: Friction factor for single phase liquids compared to the Blasius relationship, Nikuradse's data and the Colebrook relationship for the Nikuradse data points.

replicates the actual gas turbine configuration and this was more important for the current study than would be the case for a purely fundamental flow experiment. The two phase results will be compared to this transition. The high error margins seen at the lower flow rates of both oil and water are due to the small values of pressure drop. This will not be seen for two phase flows since pressure drop will have higher values even at low flow rates. The error range there will be on the order of the size of the data point, as can be seen for the higher flowrate data in Figure 5.1, so no error bars will be used.

5.2 Determination of the Inversion Point

The conductance cell is used to determine the ϕ_w at which the continuous phase is inverted into dispersed and the dispersed into continuous. Tap water is a conductive liquid while the PDMS oil is non-conductive. This property is used to determine when the continuous phase in a liquid-liquid dispersed flow is oil or water. Figure 5.3 shows the resistance

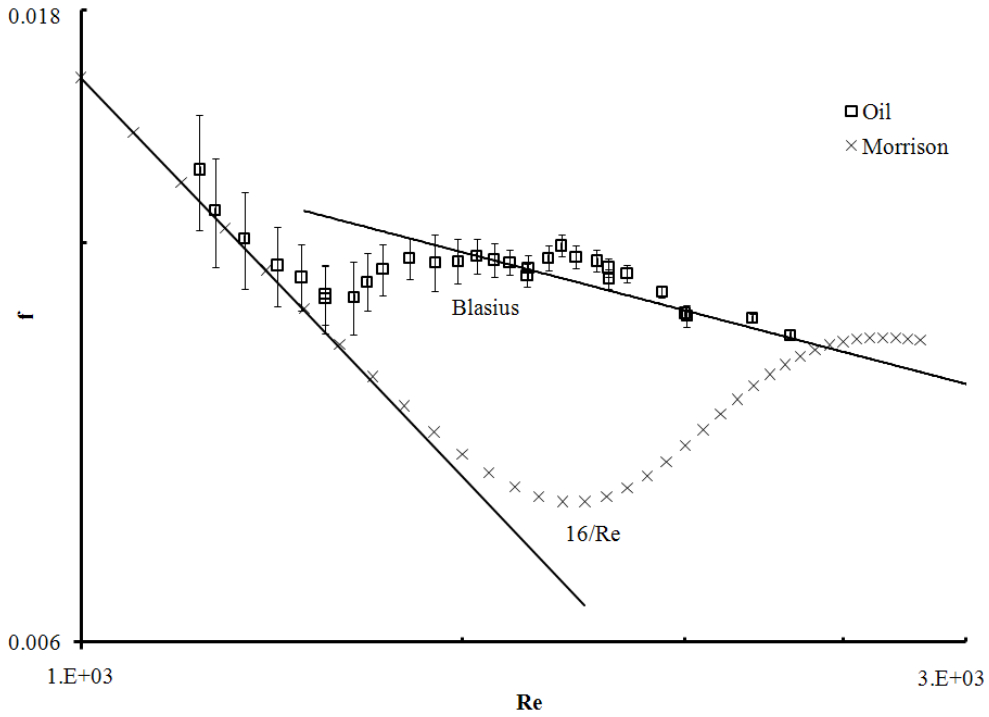

Figure 5.2: Details of the laminar-to-turbulent transition region for single phase oil flow.

of the dispersed flow as a function of ϕ_w. The inversion point is between ϕ_w = 41.25% and 43.61%, where a large change in resistance is noticed from before ϕ_w = 41.25% to after ϕ_w = 43.61%. More details are given in *Jepsen* (2009).

5.3 Liquid-Liquid Pressure Drop

This section presents the pressure drop behavior of the simultaneous flow of oil and water and analyzes it. The apparent viscosity is determined for each dispersed phase ratio. Laminar and turbulent flow regions are determined. The μ_m vs. ϕ_d of the water-in-oil system and the oil-in-water system are compared. A model based on the law-of-the-wall, independent of apparent viscosity is used to predict pressure drop in the turbulent region.

The pressure drop per unit pipe length as a function of mixture velocity is shown in Figures 5.4 for W/O flows, and in Figure 5.5 for O/W flows. Also plotted in each figure is the pressure drop due to the continuous phase, with an extended curve-fit. It can be seen that an increased dispersed phase ratio, generally gives an increase in pressure.

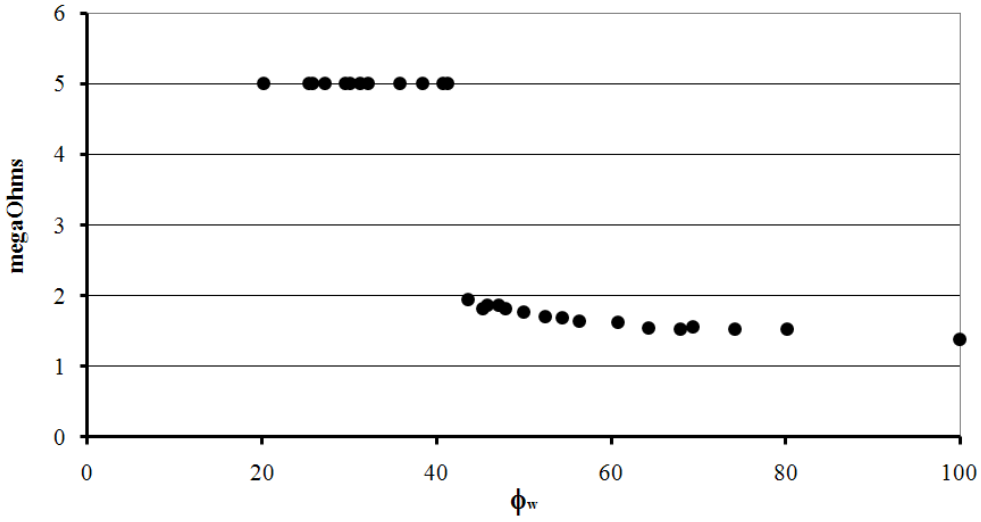

Figure 5.3: Resistance of the dispersed flow measured by the conductance cell as a function of ϕ_w.

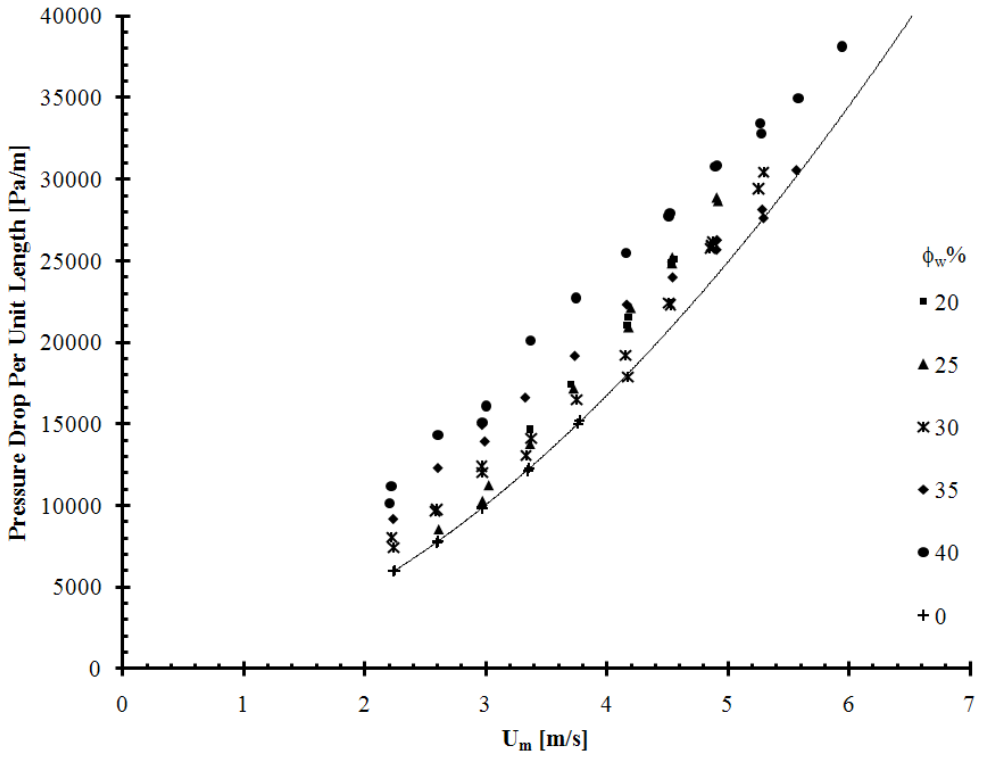

Figure 5.4: Pressure drop per unit pipe length, as function of the mixture velocity for different ϕ_w of W/O flows.

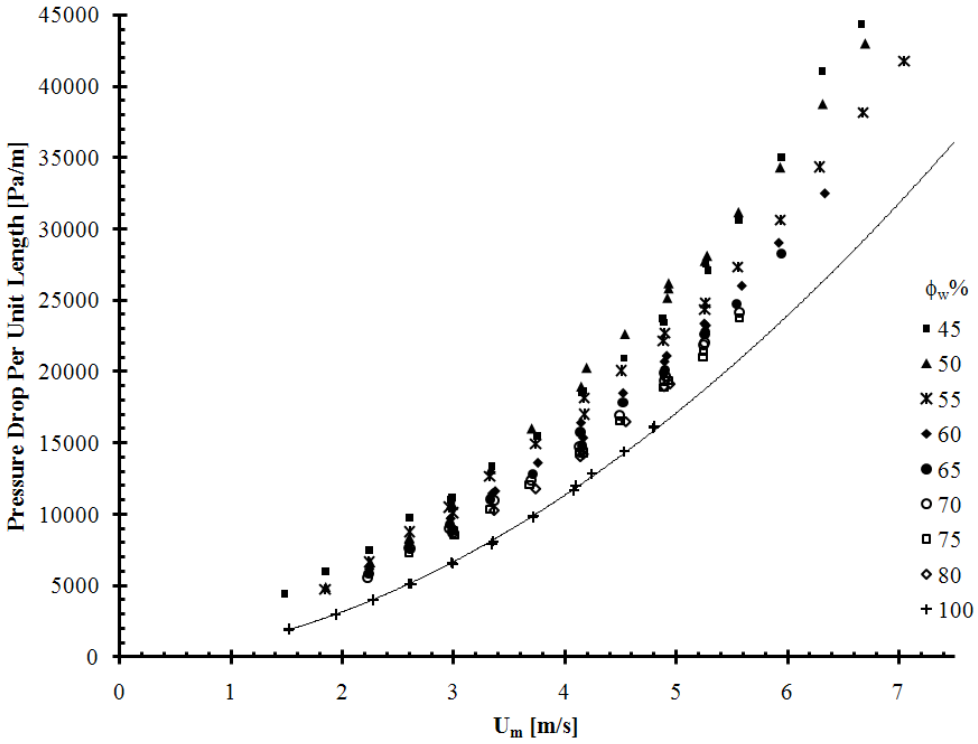

Figure 5.5: Pressure drop per unit pipe length, as function of the mixture velocity for different ϕ_w of O/W flows.

The normalized pressure drop per unit pipe length as a function of ϕ_w is shown in Figure 5.6, at selected mixture velocities (for the full range see Appendix C). The normalization is with respect to pressure drop per unit length at an equivalent mean velocity of only oil flowing in the tube. These results show that pressure drop is highest around the phase inversion point, and decreases further away.

5.3.1 Water-in-Oil Flows

The friction factor of W/O flows is shown in Figure 5.7 as a function of Re_c. Due to the nature of the flow being in a tube of relatively short length, and having limited development length, the first step to reducing friction factor data is to determine whether any of the apparent viscosity models adequately describe the results. The relationships mentioned in 3.1.1.1 were tested. The model of *Krieger and Dougherty* (1959) (Equation 3.10), and the Pal Model II by *Pal* (2003) (Equation 3.21) were found to be the best among these

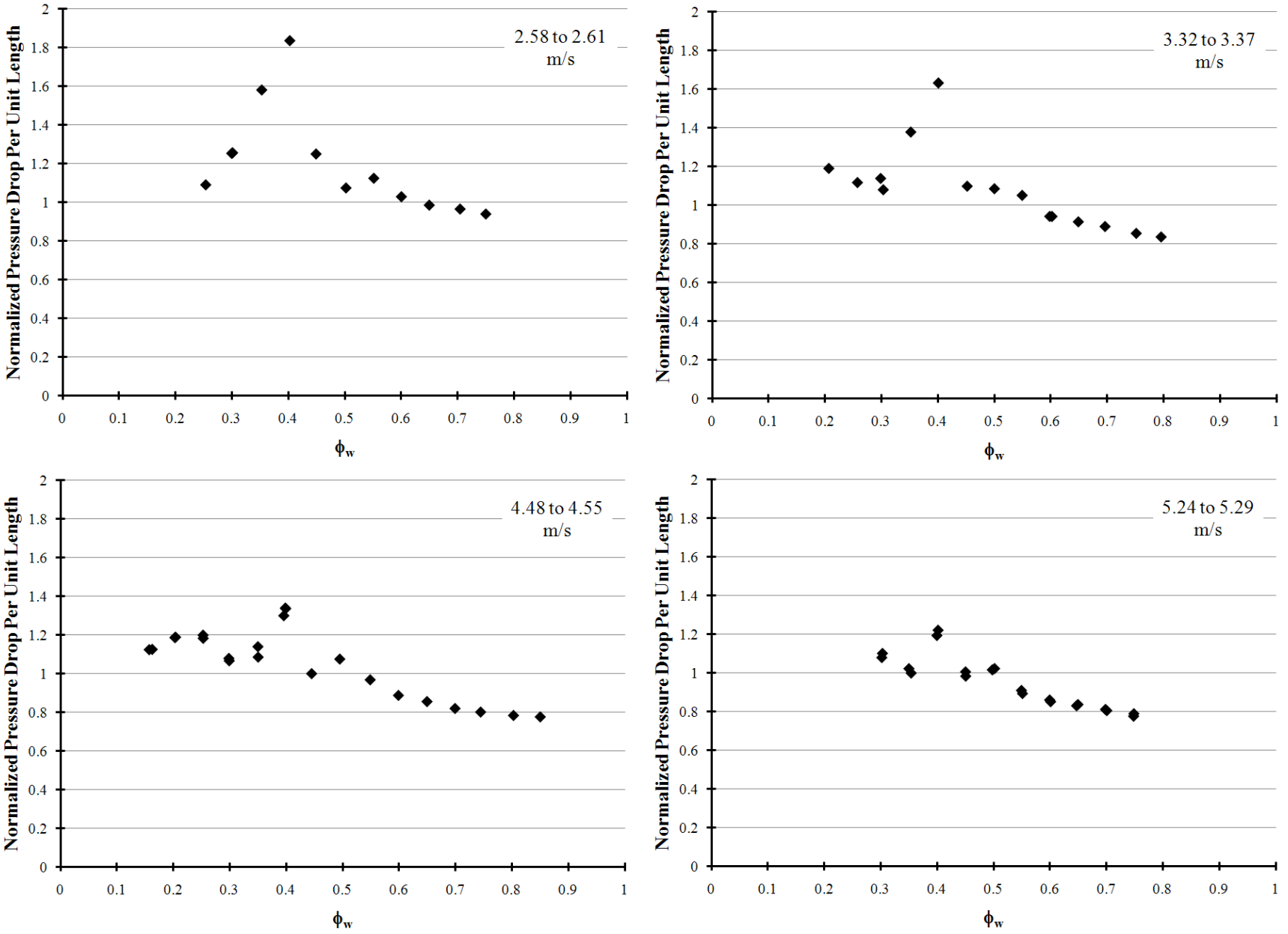

Figure 5.6: Pressure drop per unit pipe length, normalized by oil-only pressure drop at similar average velocities, as a function of ϕ_w.

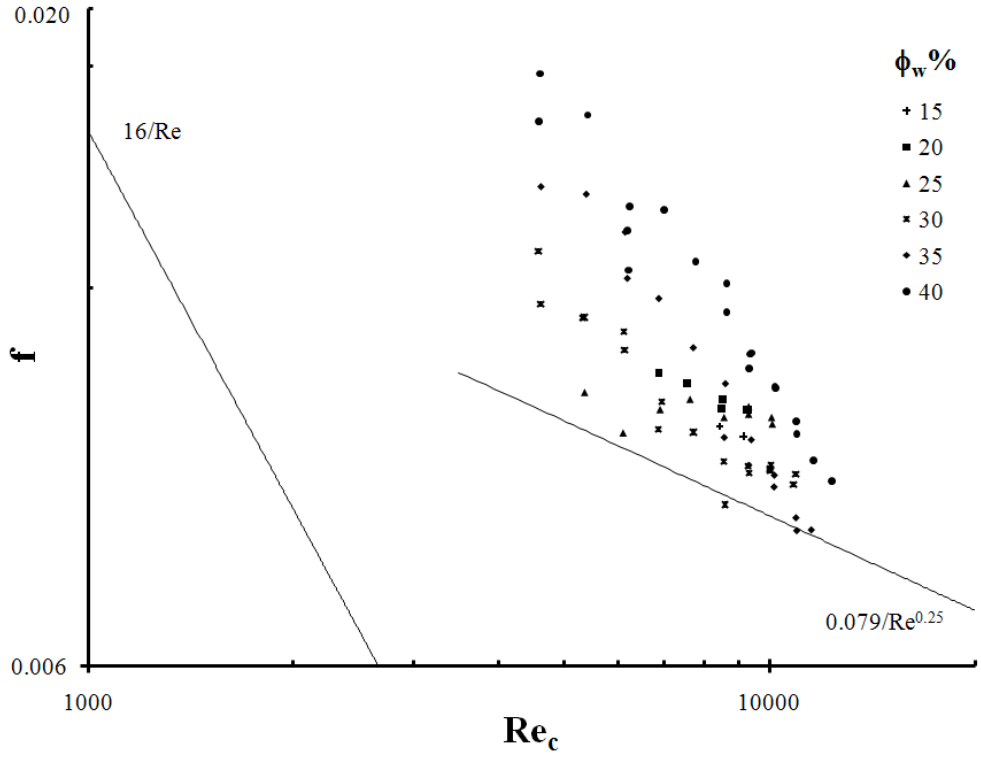

Figure 5.7: Friction factor of W/O flows as a function of Re_c.

relationships to relate the laminar flow friction factor to the Hagen-Poiseuille law.

Although the best among those available, both models seem to be inadequate. The assumption of $Ca \rightarrow 0$ in Equation 3.21 could be why Pal Model II fell shorter from Krieger and Dougherty's model, where a finite droplet capillary number would exist in this case, but measuring the droplet capillary number was not attempted. Krieger and Dougherty's model, assuming $\mu_i = 2.5$ and $\phi^{max} = 0.74$, is able to group the laminar regime of different ϕ_w but fails to align on the Hagen-Poiseuille curve. As it was mentioned in Chapter III, for the laminar regime at these dispersed phase concentrations we should not expect high deviations from Newtonian behavior.

Figures 5.8 and 5.9 reveal two regions in the laminar regime, one for $f > 0.01106$ that has a high scatter of data, and one for $f < 0.01106$ that has much smaller scatter. If the region of high scatter is assumed to behave as Newtonian, and would correspond to the Hagen-Poiseuille law, apparent viscosity can be determined through a third degree power

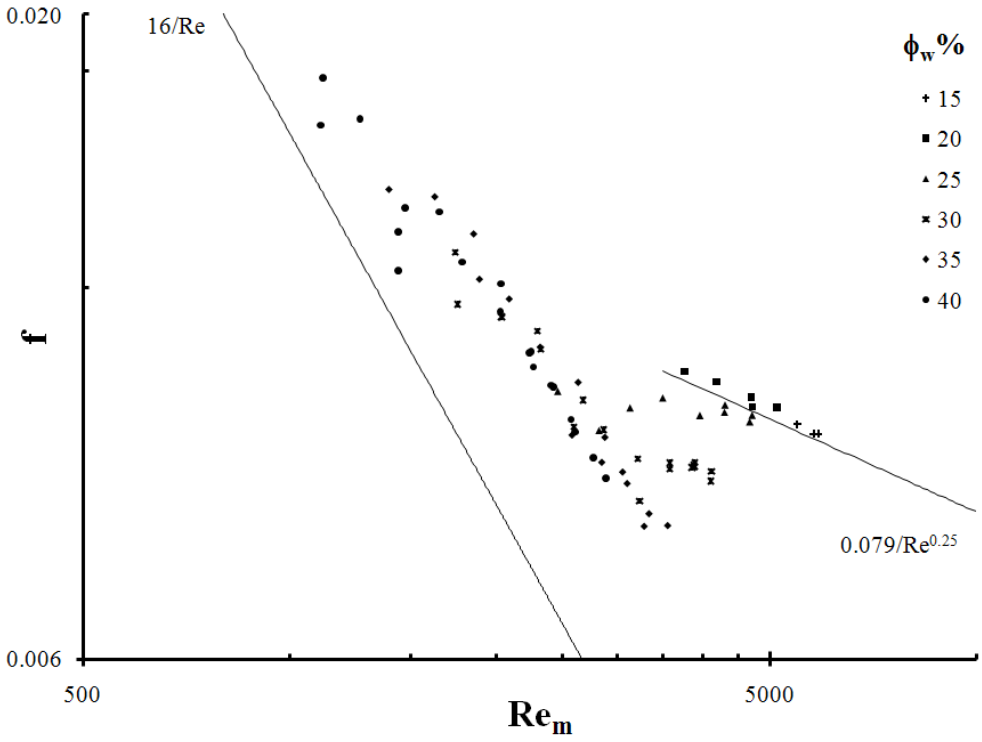

Figure 5.8: Friction factor of W/O flows as a function of Re_m. Apparent viscosity is obtained from Equation 3.10 (μ_i = 2.5 and ϕ^{mas} = 0.74).

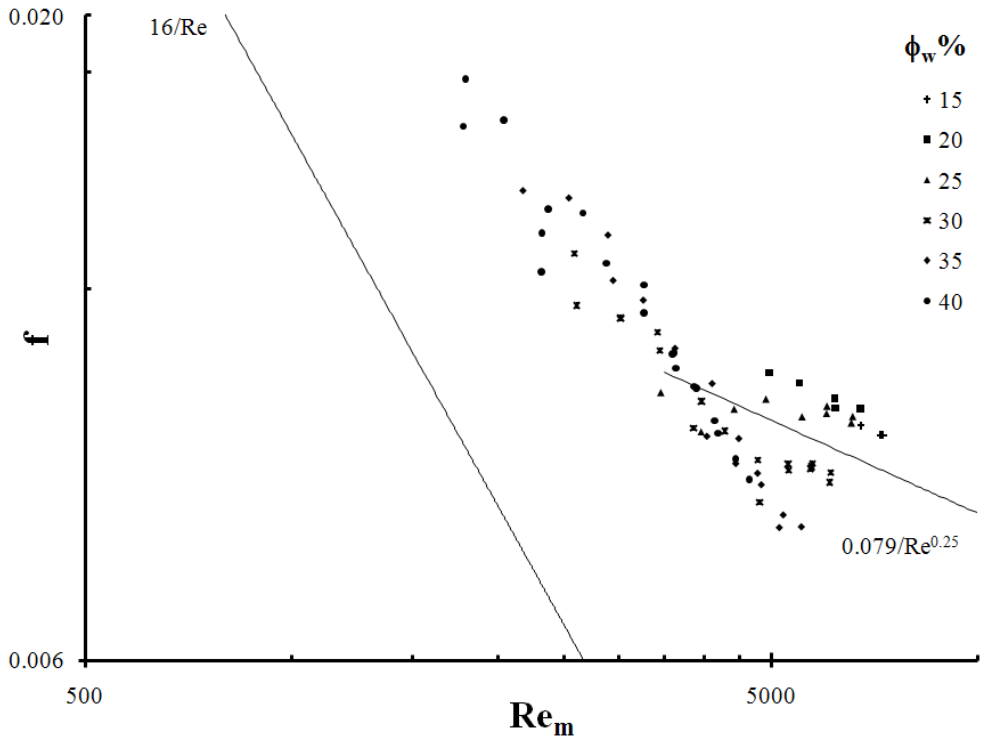

Figure 5.9: Friction factor of W/O flows as a function of Re_m. Apparent viscosity is obtained from Equation 3.21.

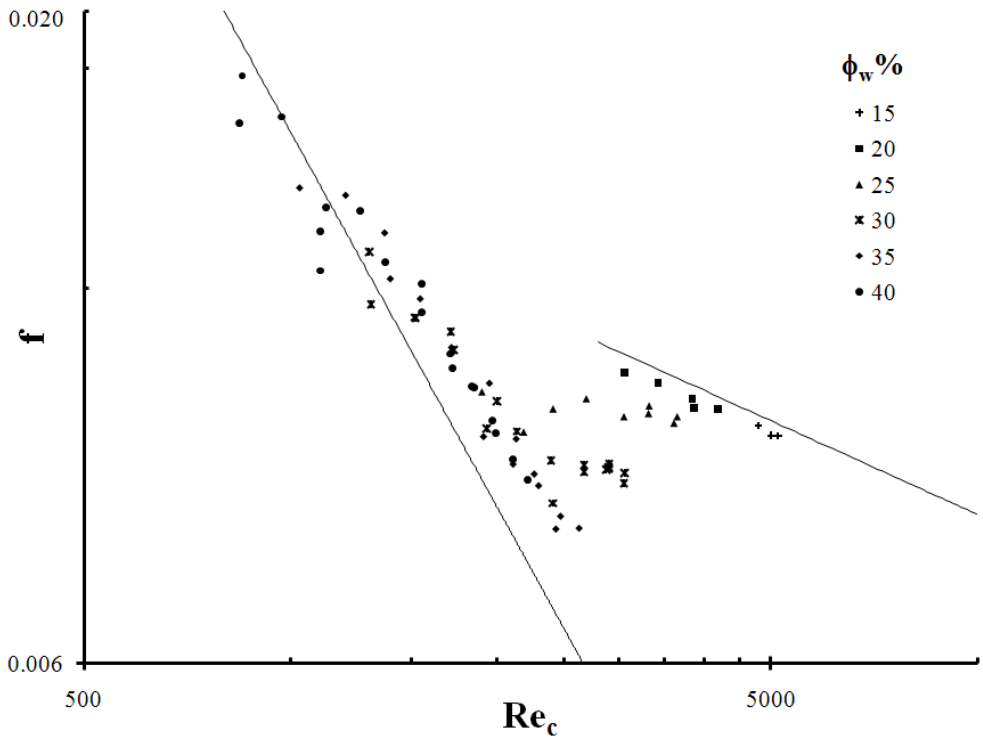

Figure 5.10: Friction factor of W/O flows as a function of Re_m. $\frac{\mu_m}{\mu_c} = 1+2.5\phi_d+12\phi_d^2+25\phi_d^3$.

series in the form of Equation 3.7. The result is shown in Figure 5.10, with the coefficients being $K_1 = 2.5$, $K_2 = 12$ and $K_3 = 25$. The region of small scatter deviates from the Hagen-Poiseiulle law slightly, in a manner similar to that observed by *Pouplin et al.* (2010). The turbulent region in Figure 5.10 ($\phi_w = 0.15$ and 0.2) is aligned with the lower side of the Blasius curve.

Alternatively, the small scatter region is made to align with the Hagen-Poiseulle law in Figure 5.11, by adjusting the apparent viscosity for each of the dispersed phase ratios in that region separately. In this case, the wide scatter region will fall to the left of the Hagen-Poiseulle curve, where the turbulent region exhibits clear drag reduction. The resulting apparent viscosity correlation is in Equation 5.1, similar to that obtained by *Vand* (1948), but with a larger K_2 constant. This difference in value can result from a larger shape factor of collision doublets (by a factor of 1.9), and also a larger collision time constant in deformable liquid droplets (by a factor of 1.5), from the values proposed by *Vand* (1948) for rigid spheres.

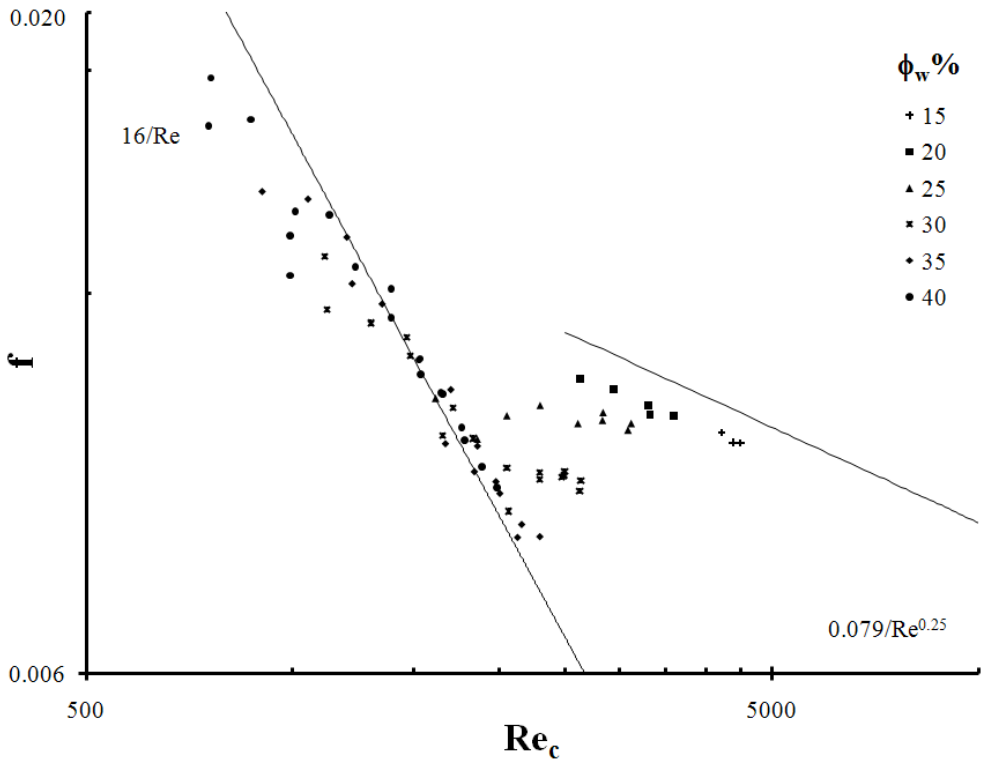

Figure 5.11: Friction factor of W/O flows as a function of Re_m. μ_m is determined through Equation 5.1.

$$\frac{\mu_m}{\mu_c} = 1 + 2.5\phi + 26\phi^2 \tag{5.1}$$

The transition region between the laminar and turbulent regimes shows a dependence on dispersed phase ratio. For the flows of ϕ_w = 0.15 and 0.2 the flow is turbulent in the measured range of data. The flow of ϕ_w = 0.25 starts the transition region to turbulence at an $Re_m \approx 1830$, followed by the flow of ϕ_d = 0.3 at an $Re_m \approx 1890$. However, flows at ϕ_w = 0.35 and 0.4 stay laminar in the measured range and it would be predictable that they will start transitioning at even higher Re_m. Very similar results were found by *Pouplin et al.* (2010). Figure 5.12 compares the transition region of the liquid-liquid flows with that of single phase oil.

All four apparent viscosity correlations mentioned above are compared in Figure 5.13.

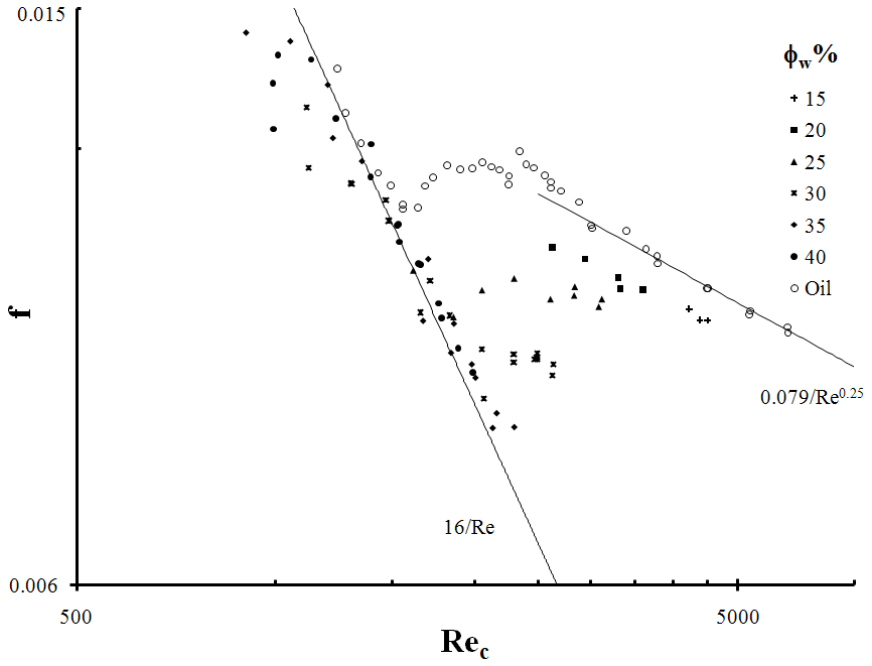

Figure 5.12: Transition region of W/O flows compared to single phase oil flow. μ_m is determined through Equation 5.1.

This comparison shows that a short entrance-length-to-diameter, combined with a short length over which pressure drop is measured and over the considered dispersed phase ratios, results in the apparent viscosity of a W/O liquid-liquid dispersed flow to be larger than predicted by most models (comparison was made but not shown for Pal Model III and the model of *Leviton and Leighton* (1936)), for which the backing experiments have larger development land test section lengths.

5.3.2 Oil-in-Water flows

The friction factor of W/O flows is shown in Figure 5.7 as a function of Re_c. Neither of the different dispersed phase concentration data are parallel to the Hagen-Poiseulle or the Blasius lines. The determination of apparent viscosity hence, depends on aligning data in the turbulent region for different concentrations. None of the relationships mentioned in Chapter III is found to be adequate. After testing different relationships the polynomial relationship of Equation 5.2 reduced the W/O friction factor to Figure 5.15. This reduction

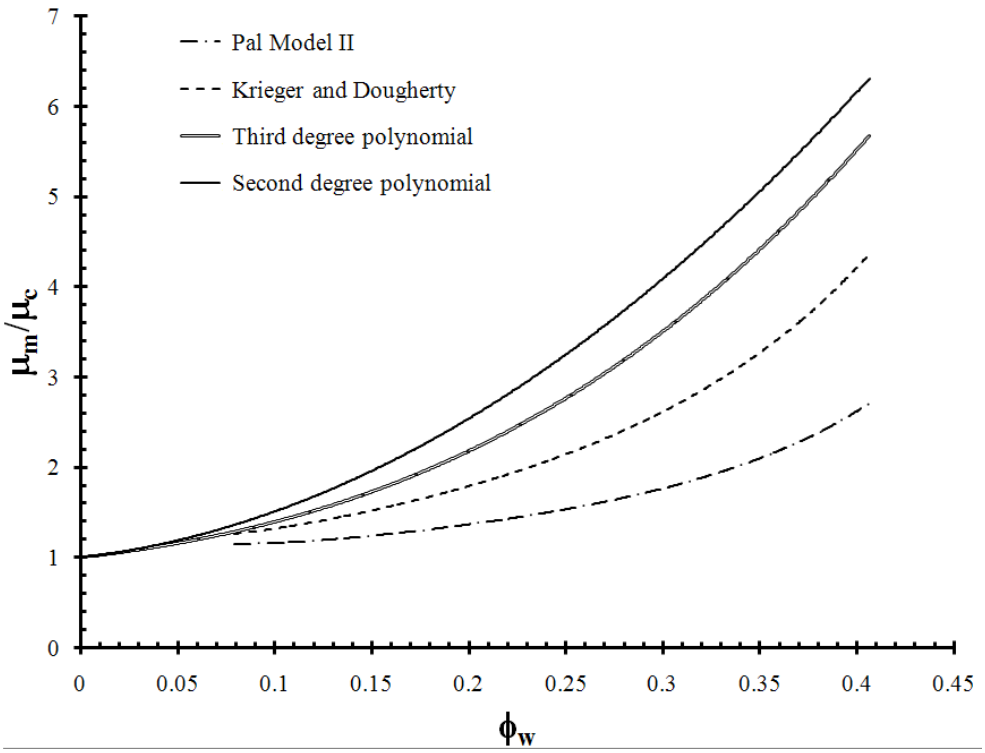

Figure 5.13: Apparent viscosity correlations investigated for W/O friction factor correlation (See text for polynomial relationships).

results in the grouping of the turbulent regime data around the line of Equation 5.3, with a scatter decreasing with increasing Re_m. Also, the laminar regime data is grouped around Equation 5.4, which clearly indicated a non-Newtonian behavior in the laminar regime. These lines, along with the single phase oil data are shown in Figure 5.16.

$$\frac{\mu_m}{\mu_c} = 1 + 67\phi - 237\phi^2 + 330\phi^3 \tag{5.2}$$

$$f = 0.27Re_m^{0.42} \tag{5.3}$$

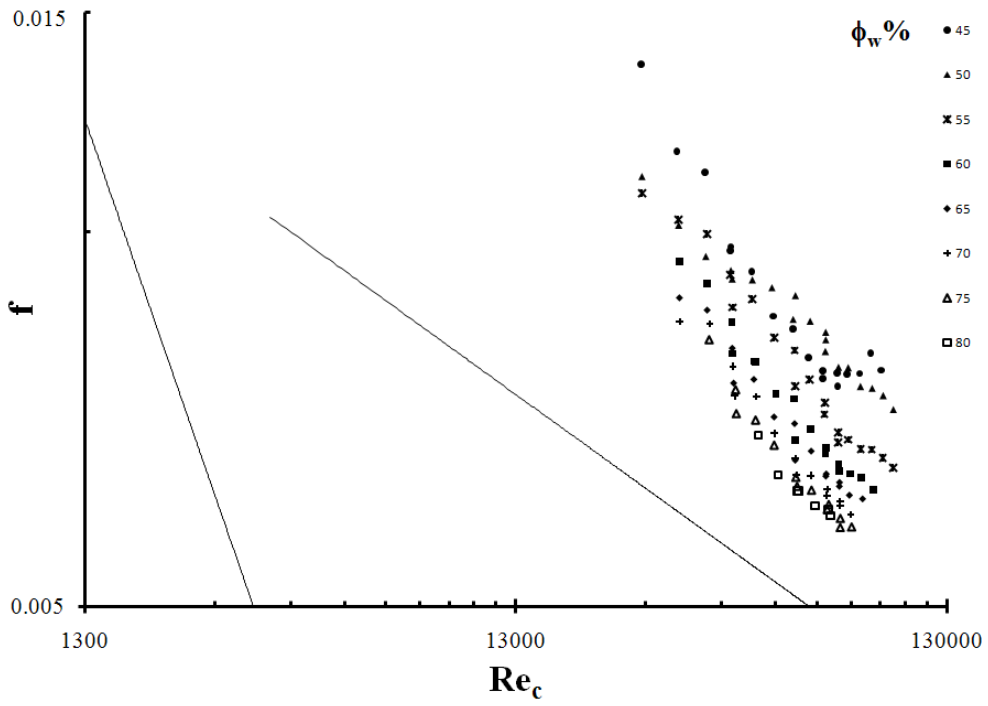

Figure 5.14: Friction factor of O/W flows as a function of Re_c.

$$f = 0.83 Re_m^{0.585} \tag{5.4}$$

A non-Newtonian behavior is expected for dispersed phase ratios of 0.5 and above. However, the available data here indicate that the $\phi_d = 0.45$ is also going to have non-Newtonian behavior, at least immediately prior to its transition region. The three dispersed phase ratios that have data in the transition region show that transition to turbulence is clearly dependent on ϕ_d, and the larger ϕ_d the later the transition to turbulence. For $\phi_d = 0.45$ the transition starts at $Re_m \approx 1650$, for $\phi_d = 0.5$ at $Re_m \approx 2100$ and for $\phi_d = 0.55$ at $Re_m \approx 3100$. However, the length of the transition region does not vary significantly with ϕ_d.

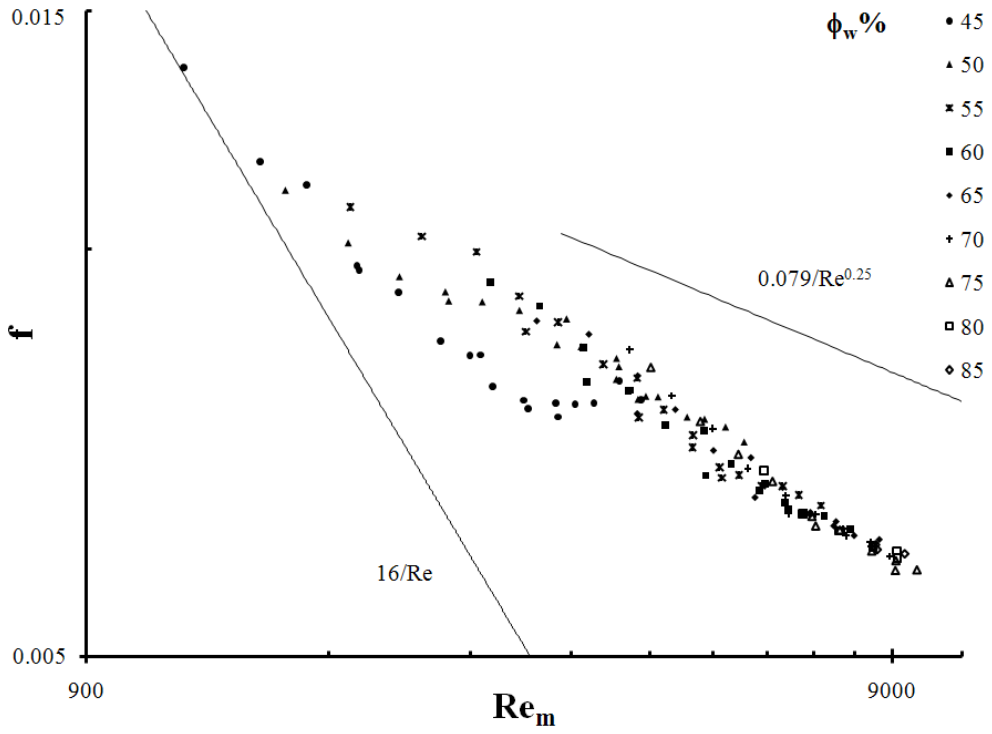

Figure 5.15: Friction factor of O/W flows as a function of Re_m. μ_m is determined by Equation 5.2.

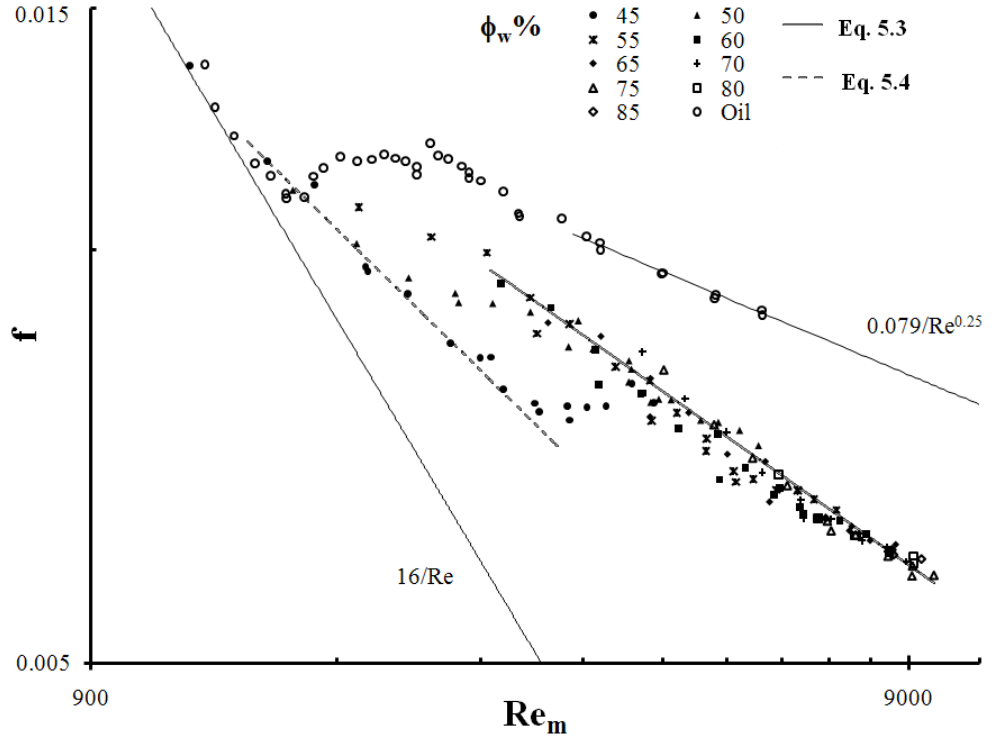

Figure 5.16: The non-Newtonian behavior of O/W flows. μ_m is determined by Equation 5.2.

5.3.3 Predicting Pressure Drop in the Turbulent Regime

Here we explore the prediction of pressure drop in the turbulent regime independent of apparent viscosity. *Mikielewicz* (2003a) proposed a one dimensional model of the Law of the Wall type for gas-in-liquid dispersed flows in vertical smooth pipes. *Vielma* (2006) modified this model to predict the friction factor in turbulent liquid-liquid dispersed flows, independently from apparent viscosity and without the knowledge of the behavior of the dispersion under laminar conditions. The model is independent of the viscosity of the dispersed phase, as it assumes the existence of turbulence only in the continuous phase, where the dispersed phase affects and modifies the turbulence of the continuous phase but the internal motion in the dispersed phase is neglected. Hence, the Reynolds number is based on the continuous phase viscosity. The model also assumes homogeneous distribution of the dispersed phase with no interfacial slip. *Vielma* (2006) obtained a non-dimensional velocity profile of Equation 5.5, equivalent to that of smooth pipes, but with modified coefficients for the case of liquid-liquid flows.

$$u^+ = \frac{1}{\kappa(1-\phi_d)^{0.5}} Ln(y^+) + B' \tag{5.5}$$

where κ is the von-Karman coefficient, and B' is an integration constant.

By defining a modified von-Karman coefficient κ' (Equation 5.6), the form of Equation 5.5 becomes similar to Equation A.15a. Based on this, *Vielma* (2006) suggested that the friction factor for liquid-liquid dispersed flows can be analogously calculated by modifying the implicit equation of the friction factor for single phase flow- Equation 5.7 - obtained by *White* (2006), to use the modified von-Karman coefficient and B', as a function of Re_c.

$$\kappa' = \kappa(1-\phi_d)^{0.5} \tag{5.6}$$

$$\frac{1}{\sqrt{f}} = \frac{1}{\sqrt{2}}\left\{\frac{1}{\kappa'}\left[Ln\left(\frac{Re_c\sqrt{f}}{2\left(\sqrt{2}+0.3(\epsilon/D)Re_c\sqrt{f}\right)}\right)-\frac{3}{2}\right]+B'\right\} \tag{5.7}$$

According to *Mikielewicz* (2003a) and *Mikielewicz* (2003b), the integration constant B' is a function of the thickness of the viscous sublayer, which in turn depends on ϕ_d (*Ward and Knudsen*, 1967; *Mikielewicz*, 2003b) and the minimum drop diameter (*Thomas*, 1962; *Mikielewicz*, 2003b). Based on this, *Vielma* (2006) expressed B' as a function of ϕ_d and the minimum droplet diameter, nomalized by the pipe diameter. The minimum droplet diameter was calculated based on the suggestion of *Kouba* (2003), given in Equation 5.8, that the Weber number corresponding to the minimum droplet diameter is 8.

$$d_{min} = \frac{8\sigma}{\rho_c U_c^2} \tag{5.8}$$

U_c is the so-called "continuous phase velocity" which can be calculated from Re_c when the density is replaced by ρ_c. *Vielma* (2006) suggested the calculation of B' using the expression of Equation 5.9. After some trial and error, it was found that the expression of Equation 5.10 suites the current data much better. For the single fluid case where there are no droplets, this from yields back B, the integration constant for single phase flow. The values of some of the constants for determining B' were also modified from the suggestions of *Vielma* (2006), a comparison is shown in Table 5.1.

$$B' = B\left[b_1^{\phi_d}(1-\phi_d)^{b_2} + b_3\left(\frac{d_{min}}{D}\right)^{b_4}\right] \tag{5.9}$$

$$B' = B\left[b_1^{\phi_d}(1+\phi_d)^{b_2} + b_3\left(\frac{d_{min}}{D}\right)^{b_4}\right] \tag{5.10}$$

Table 5.1: Constans for determining B' and κ'.

	b_1	b_2	b_3	b_4	c_1	c_2	c_3	c_4
Vielma (2006)	6	1.5	-12	1.1	0.0014	-5.1	4	1.8
Current Model	0.7	1.5	-8	0.76	0.009	-3.94	3.9	0.82

The effect of droplet-droplet interaction was taken into account in the model through the maximum droplet diameter d_{max}, which depends on the rate of coalescence and breakup. This effect was incorporated as a change in κ'. However, droplet-droplet interactions become important only when the dispersed phase has enough concentration, the limit varies, but usually is considered to begin when ϕ_d is between 0.1 and 0.2. *Vielma* (2006) considered $\phi_d = 0.1$ the limit after which droplet-droplet interaction becomes significant, in this dissertation the limit will be considered $\phi_d = 0.15$. Below this limit κ' is determined by Equation 5.6. For the high concentration case, κ' will be determined using the functional form suggested by *Vielma* (2006) in Equation 5.11, but with modified constant as shown in Table 5.1.

$$\kappa' = \kappa \left[c_1^{\phi_d} (1 - \phi_d)^{c_2} + c_3 \left(\frac{d_{max}}{D} \right)^{c_4} \right] \tag{5.11}$$

The determination of d_{max} is done through the model of *Torres-Monzon* (2006) shown in Equation 5.12.

$$d_{max} = \frac{2.93}{e^{0.4}} \left(\frac{\phi_d}{1 - \phi_d} \right)^{0.6} \left(\frac{\sigma}{\rho_c} \right)^{0.6} \tag{5.12}$$

where the rate of energy dissipation per unit mass e is determined in turbulent pipe flow through the frictional pressure drop from Equation 5.13. combining Equation 5.13 and Equation 5.12 and dividing by D we get Equation 5.14 that can be substituted in Equa-

tion 5.11.

$$e = \frac{2fU_m^3}{D} \tag{5.13}$$

$$\frac{d_{max}}{D} = \frac{2.2205}{We^{0.6} f^{0.4}} \left(\frac{\phi_d}{1 - \phi_d} \right)^{0.6} \tag{5.14}$$

Transferring from the low concentration to the high concentration regime is done through a smooth switching function. *Vielma* (2006) suggested the function in Equation 5.15 which is used in this dissertation.

$$\chi = \frac{atan[150 \times 1.75(0.15 - \phi_d)]}{\pi} + 0.5 \tag{5.15}$$

The friction factor can now be calculated through Equation 5.16.

$$f = \chi f_{low\phi} + (1 - \chi) f_{high\phi} \tag{5.16}$$

Figure 5.17 shows a comparison of the measured pressure drop per unit length (symbols) and those calculated using the model described above (curves). A fairly close matching can be seen. Figure 5.18 makes a comparison between the predicted and measured values. It can be seen that the model describes the experiments adequately in the turbulent regime.

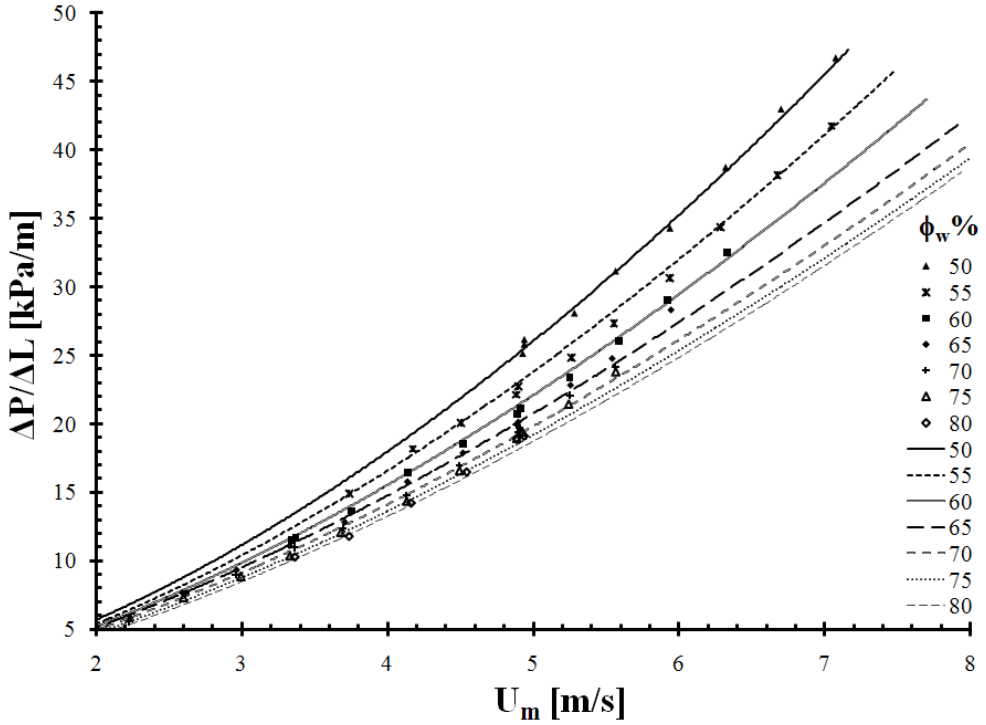

Figure 5.17: Pressure drop per unit pipe length at different mixture velocities, compared to the predictions of the model of *Vielma* (2006).

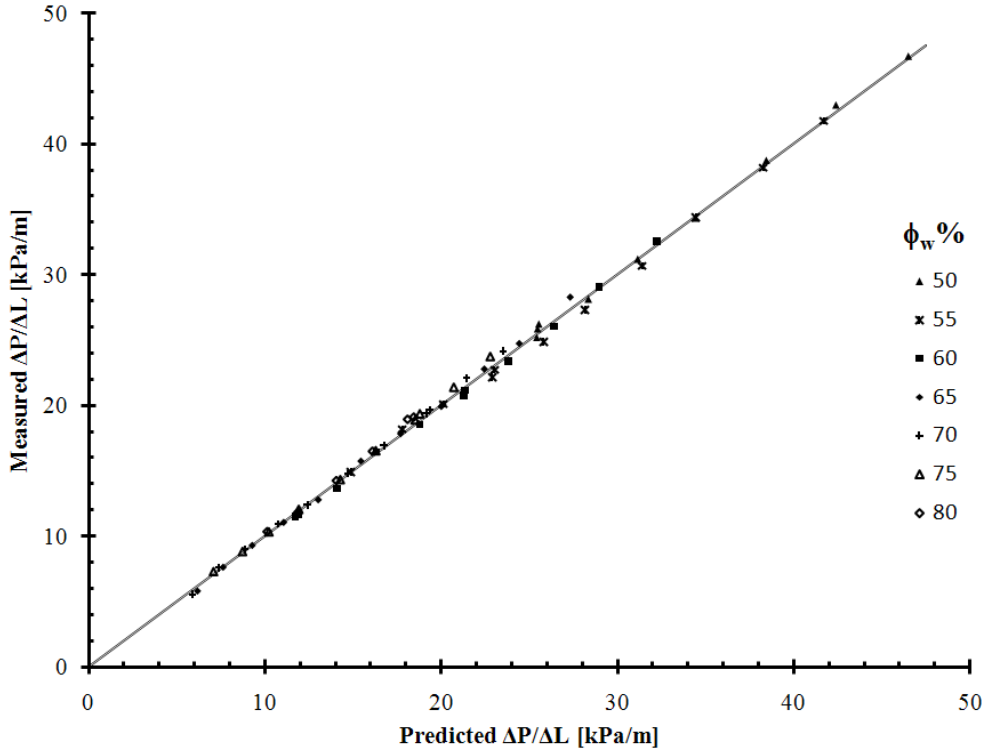

Figure 5.18: Measured values of pressure drop compared to the predictions of the model of *Vielma* (2006).

5.4 Pressure Drop Across the Safety Screen Assembly

Piping components and fittings are generally characterized by a loss coefficient K_l, defined in Equation 5.17 (*Kreith and Goswami*, 2005).

$$\frac{\Delta P}{\rho} = K_l \frac{U^2}{2} \tag{5.17}$$

For liquid-liquid flows, the averaged parameters of ρ_m and U_m would be used. In single phase flows, when the flow is turbulent in the pipe before the piping component or fitting, K_l is considered generally constant, and would not vary or be affected by the Reynolds number. *Hwang and Pal* (1997) studied the loss coefficient of sudden expansions and contractions in liquid-liquid dispersed flows. They concluded that neither the dispersed phase ratio nor the apparent viscosity had a significant effect on the loss coefficient. *Hwang and Pal* (1998) found that in the case of liquid-liquid dispersed flows of oil and water, K_l for globe valves and gate valves was also a constant, and did not depend on the dispersed phase ratio or the Reynolds number for different positions of the opening of the valves. Apart from this example, literature on liquid-liquid dispersed flows through complex fittings and piping components is scares, and the author of this dissertation is not aware of any works on the liquid liquid dispersed flows through filters and screens.

The measurement of pressure drop across the safety screen assembly was done simultaneously with the measurement of pressure drop along the tube portion of the test section. Thus, the state condition of the pipe flow at which the safety screen assembly pressure drop is measured is well characterized of whether being laminar or turbulent, based on the results of Section 5.3.

5.4.1 Pressure Drop without the Safety Screen

The pressure drop across the safety screen housing is measured first without installing the safety screen. Figure 5.19 shows the energy loss per unit mass liquid for single phase

oil and water flows as a function of the mean velocity in the tube before the housing. All the points of the single phase flows appearing in Figure 5.19 are in the turbulent regime in the tube before the Safety Screen assembly. The loss coefficient of the oil flow is $K_{lo} = 2.2$ and for water is $K_{lw} = 2.1$ with a difference less than 5%, well within expreimental error. Figure 5.20 shows the energy loss of the water-and-oil flow at different ϕ_w. The W/O flows are in the laminar regime, and some in the transition regime, with the exception of the $\phi_w = 0.2$; while the O/W flows are mostly in the turbulent regime, and few containing transition points, with the exception of $\phi_w = 0.45$ being in the laminar regime. The pressure drop of the housing without the safety screen was tested only at three different U_m, which showed to sufficiently establish a constant loss coefficient, independent of the dispersed phase ratio or the state of the flow being turbulent or laminar. This can be seen in Figure 5.21, where the mean value of K_l is 2.125. This value is not unexpected for a fitting of the internal complexity of the saftey screen housing. *Kreith and Goswami* (2005); *McCabe and Smith* (1967) mention values ranging from 0.6 to 0.9 for a smooth 90° elbow, while here the turn is not smooth with a complex interior. These results of water-and-oil flow is in line with the findings of *Hwang and Pal* (1997) and *Hwang and Pal* (1998).

5.4.2 Pressure Drop with the Safety Screen

The installation of the safety screen in the assembly increased the loss coefficient dramatically, as would be expected. Figure 5.22 shows the energy loss per unit mass liquid for single phase oil and single phase water flows as a function of the mean velocity in the tube. For the case of water, all the points are in the turbulent regime, and they lineup linearly to give $K_{lw} \approx 5.47$. However, for the case of oil, the lineup is not as clear, and points in the slower region deviate to higher losses. This is the result of many of these points being in the transition and laminar regimes, unlike the last four points which are in the turbulent regime. A value of $K_{lo} \approx 8.81$ is estimated. Despite this deviation, it is clear that the loss coefficients of water and oil single phase flows in the presence of the safety screen have considerable

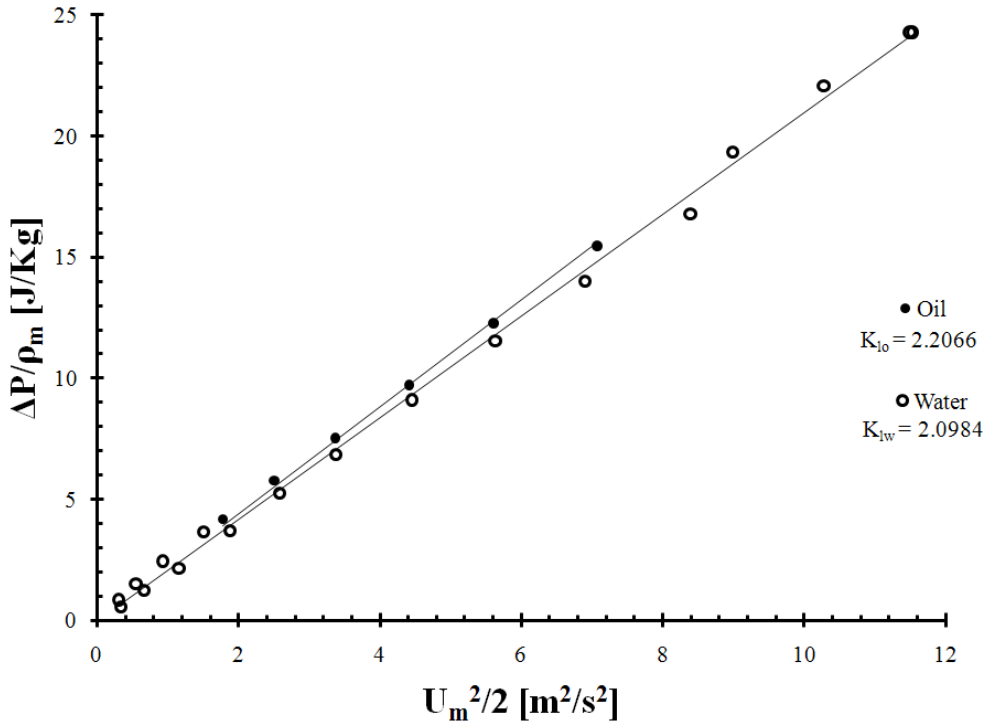

Figure 5.19: Energy loss per unit mass of liquid for single phase flow through the safety screen housing without the safety screen.

differences. A highly probable reason for this is that in the presence of the safety screen the main part of energy loss does not come from form drag, but from frictional losses resulting from the liquids being forced through the small holes of the filter. This explains the higher loss coefficient of the more viscous oil compared to the less viscous water.

The energy loss from water-and-oil flow in the presence of the safety screen are shown in Figure 5.23 at selected ϕ_w. The scatter of measured data is rather small. The loss coefficients obtained from the slopes of Figure 5.23 are shown in Figure 5.24. Two distinct regions can be seen. A constant loss coefficient K_l = 5.575 for the fully turbulent O/W flows, that is very close to the single phase water value. A linearly varying loss coefficient in the laminar O/W flows which decreases with increasing ϕ_w with a slope of -0.0686. It should be noted however, that the flows of ϕ_w = 0.15 and 0.2 are in the early turbulent regime, and ϕ_w = 0.5 and 0.55 are mostly in the turbulent regime with some transition.

As a conclusion, we can say that for the case of an element with pores like the safety

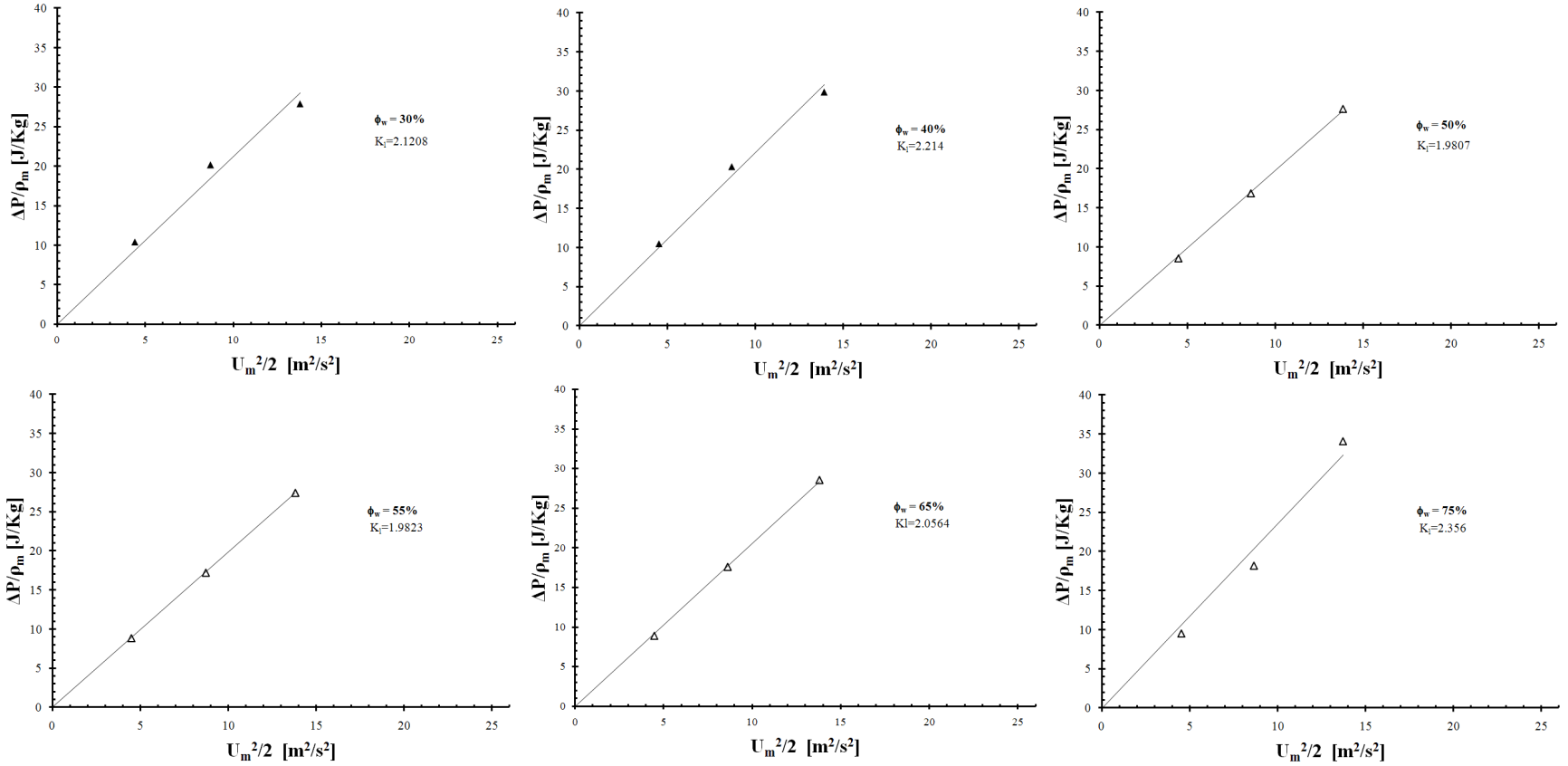

Figure 5.20: Energy loss per unit mass of liquid as a function of flow rate at different ϕ_w. Safety screen housing alone. Full symbols are W/O flow and open symbols are O/W.

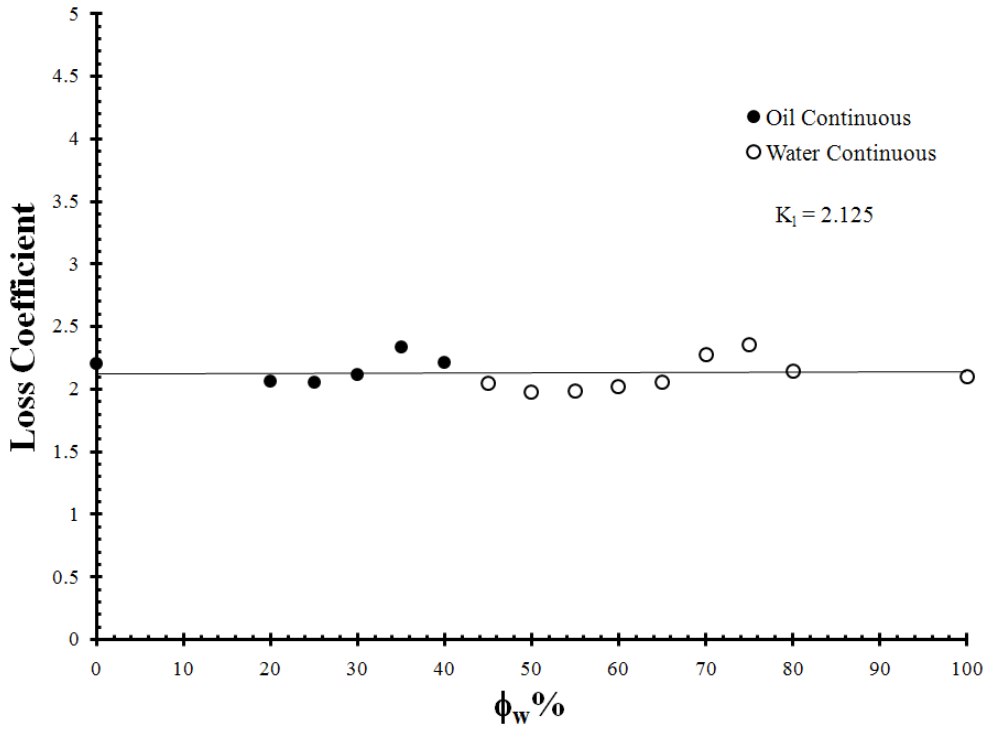

Figure 5.21: The average loss coefficient of the safety screen housing without the screen at ϕ_w.

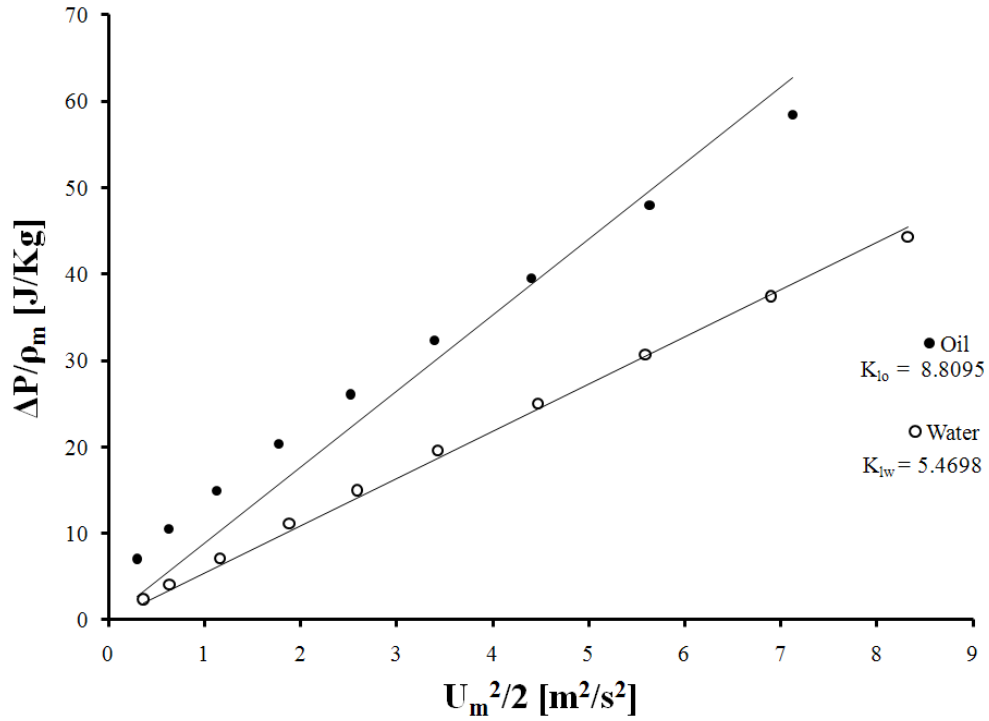

Figure 5.22: Energy loss per unit mass of liquid for single phase flow through the safety screen housing with the safety screen.

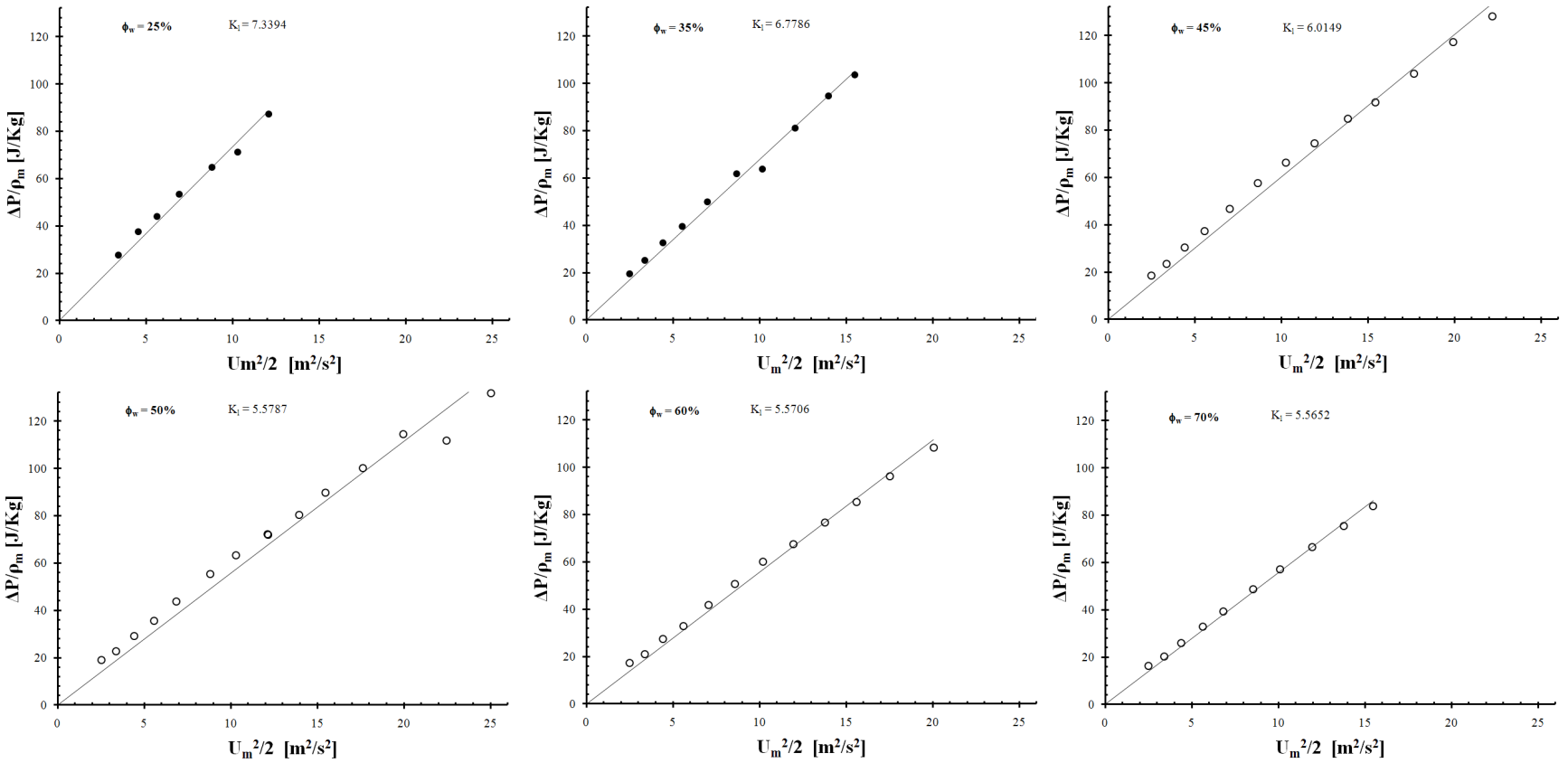

Figure 5.23: Energy loss per unit mass of liquid as a function of flow rate at different ϕ_w. Safety screen installed in housing. Full symbols are W/O flow and open symbols are O/W.

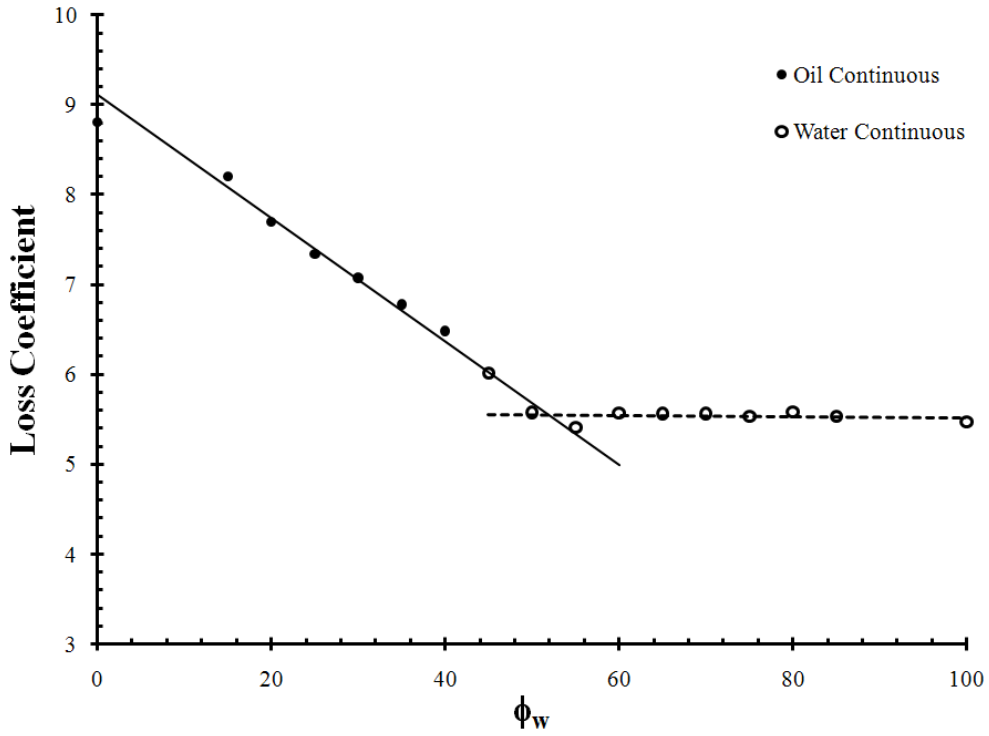

Figure 5.24: The loss coefficient of the safety screen in its housing at different ϕ_w.

screen, the loss coefficient is independent of the dispersed phase ratio in fully turbulent flows, but is linearly dependent on it for laminar flows. The loss coefficient decreases linearly with the increase of the lower viscosity liquid, regardless of which component is the dispersed and continuous phase. The loss coefficient does not depend on the apparent viscosity of the dispersion, and neither on phase inversion, as it kept behaving linearly through the inversion point between $\phi_w = 0.4$ and $\phi_w = 0.45$.

5.5 Photographic Results

The photographic setup described in Chapter IV is used to obtain images of the dispersed flow at different flow conditions. Since this requires the installation of the transparent test section, the images are acquired in separate experiments from the pressure drop measurements. The maximum zoom achievable with the lens gave photographs sized 860×575 microns, at full resolution of 10 mega-pixels, with a depth of field of 10 microns.

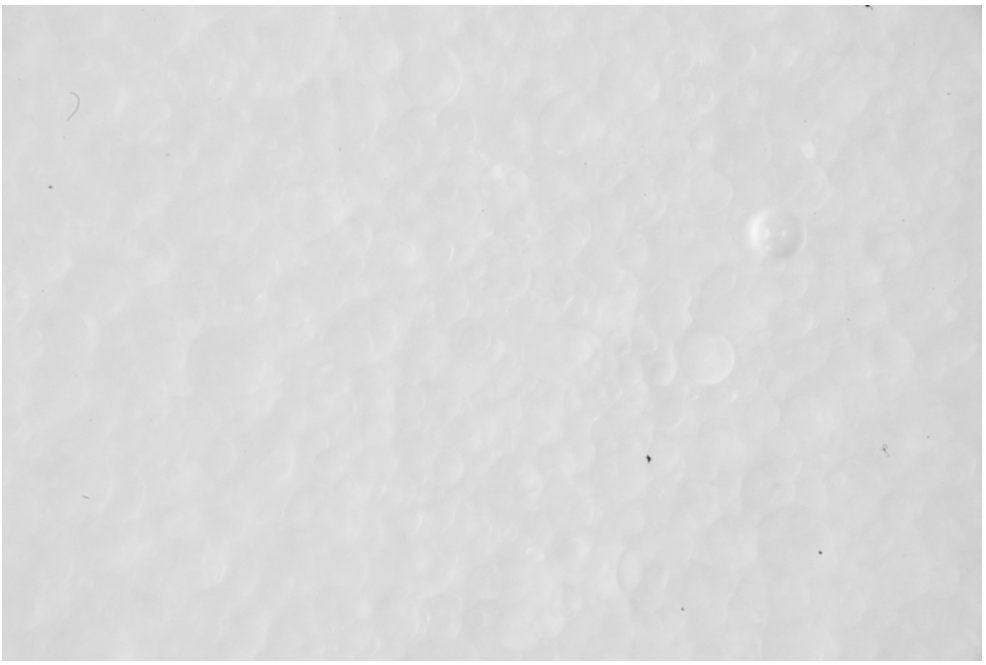

Figure 5.25: Raw image of droplets for a $\phi_w = 0.65$.

The small depth of field helps distinguish out-of-focus droplets easily. Flooding the highly scattering medium of small droplets with a diverging beam of light results in some loss of contrast. Despite this, the raw images still have enough contrast between the continuous phase and the droplets for the latter to be clearly distinguished. However, a correction of contrast by image processing software helps enhance the overall contrast and makes distinguishing the droplets even easier. Figure 5.26 shows a raw image for $\phi_w = 0.65$. The same image after being corrected for contrast and brightness is shown in Figure 5.26, with a scale added to the frame of the image.

Obtaining droplet size information from photographs of high concentration of circular shapes is still an active area of research. The difficulty in automatic processing of corrected images comes from the following complicating factors. The contrast at the border of the droplets is not high enough due to the difficulty of achieving this in the highly scattering medium, an issue that exacerbates with decreasing droplet sizes; the large number of droplets adjacent to each other, which becomes worse with increasing dispersed phase ratio; the possibility of droplets within the depth of field overlapping each other; and finally

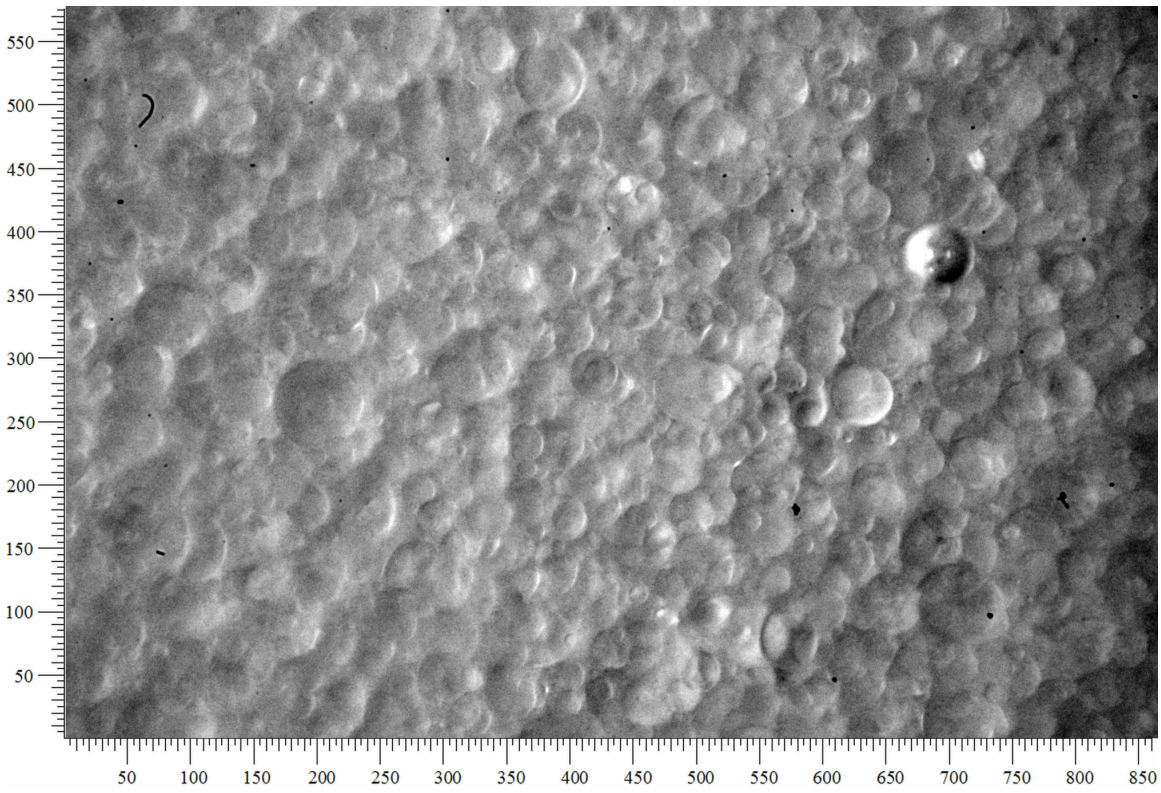

Figure 5.26: The image in Figure 5.25 corrected for contrast and brightness. The displayed units are in microns.

a size range of droplets that varies over an order of magnitude or more. Various levels of success have been achieved in automatically obtaining the droplet size distribution from images. *Alban et al.* (2004) achieved automatic detection of droplets and obtained droplet size distributions of droplets on the order of millimeters in various dispersed stirred vessels. Their image quality was significantly affected by the increase of dispersed phase ratio. Most other techniques for smaller ranges of droplet sizes and high concentrations are still semi-automated at best, and require human intervention in detecting the droplets, which can afterwards be counted and measured automatically (*Taboada et al.*, 2006; *Zabulis et al.*, 2007). In this dissertation, once the droplets were manually detected and marked using graphics software on the images. An algorithm based on the Hough transform was used to count and measure the droplets.

CHAPTER VI

Discussion

To better understand the reasons behind the specific behavior of liquid-liquid flows in pipes and tubes presented in Chapter V, more light should be shed on the behavior of droplets in these flows. Here, an analysis will be presented on the deformability of droplets in the dispersions studied in this dissertation, and provide direct photographic evidence where possible.

6.1 Analysis of the Behavior of Laminar Flows

The W/O flows of $0.25 < \phi_w < 0.4$ as well as the O/W flow of $\phi_w = 0.45$ were mostly in the laminar and some in the transition regimes. *Pouplin et al.* (2010) suggested that the Newtonian behavior of laminar dispersion flows is linked to the ability of the droplets to retain their spherical shape. They proposed a criterion to determine a critical Ohnesorge number which can be used to determine the range of droplet sizes that would undergo a finite deformation without fracturing. This criterion can be used to explain any deviation from Newtonian behavior. The criterion states that if the Capillary number is greater than 0.1 in a laminar flow (determined by the Reynolds number being below the critical limit), then the critical Ohnesorge number is given by Equation 6.1. And the droplet or radius r will deform when the Ohesorge number based on the continuous phase is greater than Oh_{crit}, as shown in Relationship 6.2.

$$Oh_{crit} = \left(\frac{Ca_{lim}}{Re_{mcrit}}\right)^{\frac{1}{2}} \frac{D}{r} \frac{\rho_c \mu_c}{\rho_m \mu_m} \tag{6.1}$$

$$Oh = \frac{\mu_c}{(\rho_c \sigma r)^{0.5}} > 0.316 \frac{1}{\sqrt{Re_{mcrit}}} \frac{D}{r} \frac{\rho_c \mu_c}{\rho_m \mu_m} \tag{6.2}$$

The Oh of the W/O and O/W laminar flows is calculated, and compared to Oh_{crit} for each ϕ_w in Figure 6.1 over a range of droplet diameters.

The behavior of W/O flows can be explained based on this comparison. Most of the droplets in the dispersed flows studied are generated due to the high shear regions in complex interior of the check valve at the end of the t-junction. The shear rate is proportional to the flow rate. Thus, the higher the flow rate the higher the shear rate that acts on the droplets, which leads to the creation of smaller droplets that resist deformation. Therefore, in the W/O flows a Newtonian behavior is observed for most of the laminar region. This is consistent with the vast majority of results of other investigators as we noted in Chapter III. However, there seems to be a slight deviation from Newtonian behavior at the lower end of Re_m. It is not possible to completely rule out experimental error, but a possible explanation based on the Ohnesorge number criterion could be made, since the lower flow rates will produce lower shear rates in the check valve, hence generate larger droplets that could undergo coalescence in the tube due to corresponding lower shear rates in the tube as well, which will result $Oh > Oh_{cirt}$. This is more likely at higher dispersed phase concentrations.

The behavior of O/W flows is less clear, as the entire measured laminar range deviates significantly from Newtonian behavior. O/W flows have a larger maximum capillary number that allows the existence of droplets up to 450 microns, compared to only 250 microns for W/O flows, before they are fractured. Despite being larger, these droplets will still have

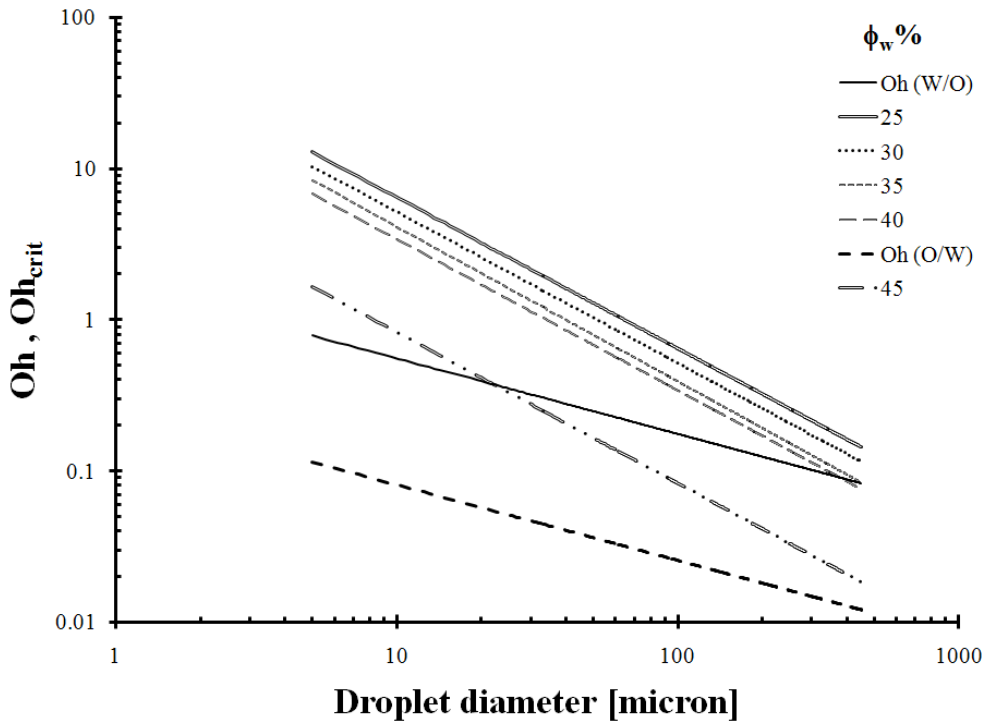

Figure 6.1: The Ohnesorge number of W/O and O/W flows for different droplet sizes compared to the critical values.

Ohnesorge numbers less than Oh_{crit} as shown in Figure 6.1. The photographic evidence also supports the fact that no droplets with significant deformation was seen (Figure 5.26). Thus, it is suggested that droplet deformation is not the mechanism responsible for the non-Newtonian behavior. It is not clear to the author at this point what this mechanism could be.

6.2 Analysis of the Behavior of Turbulent Flows

According to the definition of turbulent drag reduction mentioned in Section 3.1.4 of Chapter III, O/W turbulent regime flows presented in Chapter V underwent drag reduction. Two major hypotheses exist that explain turbulent drag reduction in liquid-liquid dispersed flows. The first hypothesis, by *Pal* (1993), holds the dynamic coalescence and breakup of droplets in unstable liquid-liquid dispersions responsible for modifying the turbulence of the continuous phase, thus causing a reduction in drag. In support of this view, Pal cited

the limited drag reduction observed in surfactant stabilized flows. There is no explanation, however, to the mechanism by which the breakup and coalescence events would modify the turbulence. The second hypothesis, by *Pal* (2007), suggests that the drag reducing behavior is the result of the deformation of the dispersed phase droplets, because of what Pal describes as a lower effective viscosity of the dispersion in turbulent flow. It is not clear in this explanation why would deforming droplets cause a lower effective (apparent) viscosity. The photographic evidence of *Collins and Knudsen* (1970) (Figure 3.17) cited by *Pal* (2007) was not taken in a flow system representative of the type of dispersed flows analyzed by Pal. As mentioned in Chapter III *Collins and Knudsen* (1970) studied the effect of turbulence on the breakup of droplets, and the introduction of the dispersed phase into the continuous was done very carefully, so that any breakup of droplets happens only due to the turbulence of the continuous phase, while the systems considered here contain dispersions generated due to high shear rate in agitators and pumps or fittings. Although the flow conditions of *Ward* (1964) were ideal, and he obtained in-situ droplet images that look much different than the images of *Collins and Knudsen* (1970), it cannot be stated that the flows of Ward were drag reducing because no measurements were made in the laminar regime. But even so, there still was no evidence of droplet stretching in the photographs of *Ward* (1964).

The results obtained in this dissertation do not show any evidence of the droplet deformation explanation of drag reduction. The photographs did not contain any droplets with observable deviation from the spherical shape. Also, calculations show that droplets under the flow conditions, will retain their spherical shapes. *Pouplin et al.* (2010) suggested a criterion for determining the deformability of droplets smaller than the Kolmogorov length scale ($\eta_k = \left(\nu_c^3/\bar{\epsilon}\right)^{0.25}$) in a turbulent flow. According to this criterion (Relationshp 6.3), if the capillary number based on the strain rate of the Kolmogorov scale is smaller than 0.1, then the droplets will not be deformed.

$$\frac{\mu_m \gamma_k d}{2\sigma} < 0.1 \tag{6.3}$$

where

$$\gamma_k = \left(\frac{2\bar{\epsilon}}{15\nu_c}\right)^{0.5} \tag{6.4}$$

where $\bar{\epsilon}$ is the average turbulence energy dissipation rate, given by Equation 6.5.

$$\bar{\epsilon} = 5.6 \times 10^{-3} \frac{U_m^3}{D} \tag{6.5}$$

this makes the final form of Equation 6.3 be given as:

$$0.027325 \sqrt{Re_m} \frac{\mu_m U_m}{\sigma} < 0.1 \frac{D}{d} \tag{6.6}$$

Calculating these values for the measured range shows that droplets that are the size of the Kolmogorov scale are are 2 to 12 times below the deformability limit. Droplets larger than the Kolmogorov scale will have more complicated criteria of deformability, but there is no photographic evidence of the existence of such deformations. Therefore, we can conclude that the mechanism by which drag reduction is taking place is due to the dynamic coalescence and breakup of droplets. Figure 6.2 shows a sample of the images collected for O/W flows in the turbulent regime experiencing drag reduction where droplets appear to preserve their spherical shape.

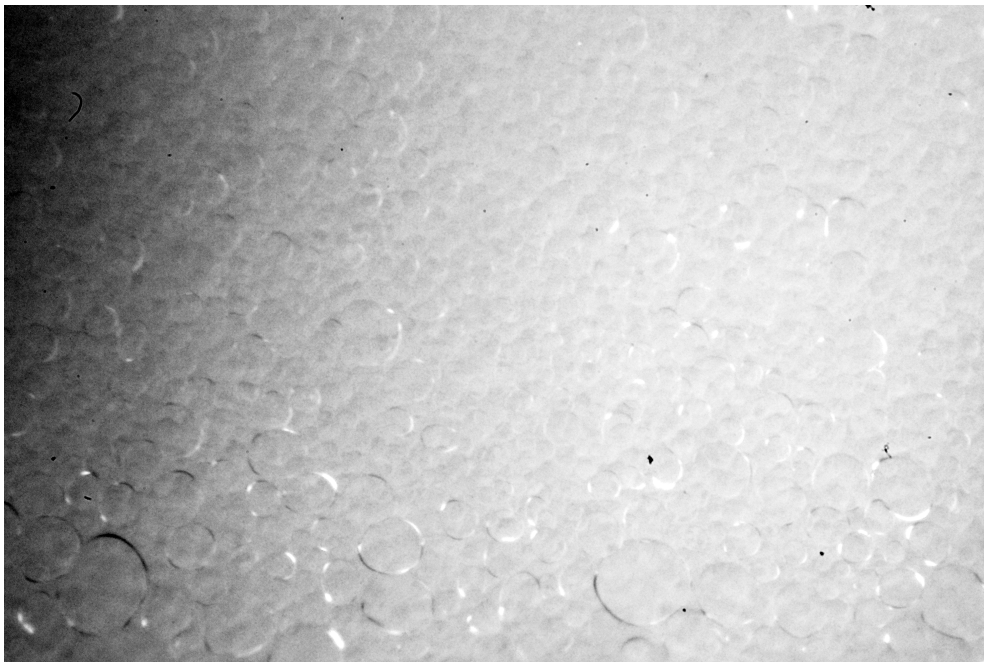

Figure 6.2: Droplets in an O/W flow, for conditions of Test Number 181 of Table D.15.

CHAPTER VII

Conclusions

The examination of pressure drop characteristics of liquid-liquid dispersed flows of PDMS and tap water, in a piping system and under conditions very similar to industrial installations led to the following conclusions.

- In the short distances available for measurement in the installation, single phase flows transitioned to turbulence at low Reynolds numbers due to short development lengths.
- W/O flows formed up to a dispersed phase concentration of 40%, their behavior was close to a Newtonian behavior, and most of those flows were in the laminar and transition regimes.
- The apparent viscosity of W/O flows was found to follow a second degree power series, with coefficients comparable to literature values.
- Increasing the dispersed phase ratio in W/O flows resulted in a higher Re_m for transition to turbulence.
- O/W flows formed up to dispersed phase concentrations of 60%, they were found to have non-Newtonian behavior, in both the laminar and turbulent regimes.
- O/W flows experienced drag reduction, but no evidence was found on droplet deformation being responsible for this behavior.

- The apparent viscosity of O/W flows was found to follow a third degree power series.
- Increasing the dispersed phase ratio in O/W flows resulted in a higher Re_m for transition to turbulence.
- A model from the literature, based on the Law-of-the-Wall was adopted to predict the pressure drop in turbulent O/W flows, independent from apparent viscosity. The model successfully predicted measured pressure drop values.
- In-situ photographic images of droplets in the near-wall area were obtained by using a method which we found no evidence of it having been used before. Illumination was provided by the backscattering from a diverging beam of light, generated from an arc flash with a duration of a few hundreds of nanoseconds.
- The loss coefficient of the housing a safety screen, without the safety screen installed, was determined to be a constant, independent of dispersed phase ratio, type of dispersion and the Reynolds number.
- The loss coefficient of the housing with the safety screen installed was determined to be constant from flows that are fully turbulent.
- The loss coefficient of the housing with the safety screen installed but for laminar and transition regime flows was determined to depend only on the ratio of the more viscous component, and increasing as the concentration of that phase increased. There was no dependence on the Reynolds number or the type of dispersion.

BIBLIOGRAPHY

BIBLIOGRAPHY

Alban, F., S. Sajjadi, and M. Yianneskis (2004), Dynamic Tracking of Fast LiquidLiquid Dispersion Pprocesses With a Real-Time In-Situ Optical Technique, *Chem. Eng. Research and Design*, *82*, 843–859.

Angeli, P., and G. Hewitt (1998), Pressure Gradient in Horizontal Liquid-Liquid Flows, *Int. J. Multiphase Flow*, *24*, 1183–1203.

Angeli, P., and G. Hewitt (2000a), Drop Size Distribution in Horizontal Oil-Water Dispersed Flows, *Chemical Eng. Sci.*, *55*, 3133–3143.

Angeli, P., and G. Hewitt (2000b), Flow Structure in Horizontal Oil-Water Flow, *Int. J. Multiphase Flow*, *26*, 1117–1140.

Barnea, E., and J. Mizrahi (1975), A Generalized Approach to the Fluid Dynamics of Particulate Systems. Part 2: Sedimentation and Fluidisation of Clouds of Spherical Liquid Drops, *Canadian J. Chemical Engineering*, *53*, 461–468.

Barnea, E., and j. Mizrahi (1976), On the "Effective" Viscosity of Liquid-Liquid Dispersions, *Ind. Eng. Chem. Fund.*, *15*(2), 120–125.

Baron, T., C. Sterling, and A. Schueler (1953), Viscosity of Suspensions - Review and Application in Two-Phase Flow, *Proceedings of Midwestern Conference of Fluid Mechanics*, *3*, 103–123.

Bolszo, C., A. Narvaez, S. Abbilian, A. Jepsen, D. Dunn-Rankin, V. McDonell, and W. Sirignano (2009), Generation and Pressure Atomization of Water-in-Oil Emulsions for Gas Turbines.

Brauner, N. (2001), The Prediction of Dispersed Flow Boundaries in Liquid-Liquid and Gas-Liquid Systems, *Int. J. Multiphase Flow*, *27*, 885–910.

Brauner, N. (2003), *Modeling and Experimentation in Two-phase Flow*, 221 pp., Springer-Wien, New York.

Cengel, J., F. A., F. J., W. C., and K. J. (1962), Laminar and Turbulent FLow of Unstable Liquid-Liquid Emulsions, *AIChE J.*, *8*(3), 335–339.

Chaker, M., C. Meher-Homji, and T. Mee III (2004), Inlet Fogging of Gas Turbine EnginesPart I: Fog Droplet Thermodynamics, Heat Transfer, and Practical Considerations, *J. Engineering for Gas Turbines and Power*, *126*, 545–558.

Choi, S., and W. Schowalter (1975), Rheological Properties of Nondilute Suspensions of Deformable Particles, *Phys. Fluids*, *18*(4), 420–427.

Colebrook, C. (1939), Turbulent Flow in Pipes, with Particular Reference to the Transition Region Between Smooth and Rough Pipe Laws, *Journal of the Institution of Civil Engineers*.

Collins, S., and J. Knudsen (1970), Drop-Size Distribution Produced by Turbulent Pipe Flow of Immiscible Liquids, *AIChE J.*, *16*(6), 1072–1080.

Derkach, S. (2009), Rheology of Emulsions, *Advances in Colloid and Interface Science*, *151*, 1–23.

Eckert, R., C. McLaughlin, and J. Rushton (1985), Liquid-Liquid Interfacial Areas Formed by Turbine Impellers in Baffled, Cylindrical Mixing Tanks, *AIChE J.*, *31*(11).

Einstein, A. (1906), Calculation of the Viscosity-Coefficient of a Liquid in Which a Large Number of Small Spheres Are Suspended, *Annalen der Physik*.

Elseth, G. (2001), An Experimental Study of Oil/Water Flow in Horizontal Pipes, Ph.D. thesis, The Norwegian University of Science and Technology (NTNU), Porsgrunn, Norway.

Fairuzov, Y., P. Arenas-Medina, J. Verdejo-Fierro, and R. Gonzalez-Islas (2000), Flow Pattern Transitions in Horizontal Pipelines Carrying Oil-Water Mixtures: Full-Scale Experiments, *J. Energy Resources Technology*, *122*, 169–176.

Faruqui, A., and K. J. (1962), Velocity and Temperature Profiles of Unstable Liquid-Liquid Dispersions in Vertical Turbulent Flow, *Chemical Eng. Sci.*, *17*, 897–907.

Frankel, N., and A. Acrivos (1970), The Constitutive Equation for a Dilute Emulsion, *J. Fluid Mechanics*, *44*(1), 66–78.

Fu, W., L. Hou, L. Wang, and F. Ma (2002), A Unified Model for the Micro-Explosion of Emulsified Droplets of Oil and Water, *Fuel Processing Technology*, *79*, 107–119.

Govier, G., and K. Aziz (1972), *The Flow of Complex Mixtures in Pipes*, 503-612 pp., Van Nostrand Reinhold Company, New York, USA.

Hamann, O. (2002), Method and Apparatus for Particle Assessment Using Multiple Scanning Beam Reflectance, United States Patent, no. 6,449,042.

Hinze, J. (1955), Fundamentals of the Hydrodynamic Mechanism of Splitting in Dispersion Processes, *AIChE J.*, *1*(3), 289–295.

Hughmark, G. (1971), Drop breakup in turbulent pipe flow, *AIChE J.*, *17*(4), 1000.

Hwang, C., and R. Pal (1997), Flow of Two-Phase Oil/Water Mixtures Through Sudden Expansions and Contractions, *Chemical Eng. J.*, *68*, 157–163.

Hwang, C., and R. Pal (1998), Pressure Losses in Globe and Gate Valves during Two-Phase Oil/Water Emulsion Flow, *Ind. Eng. Chem. Res.*, *37*, 636–642.

Ioannou, K., N. O., and P. Angeli (2005), Phase Inversion in Dispersed Liquid-Liquid Flows, *Experimental Thermal and Fluid Science*, *29*, 331–339.

Jaeger, H., and R. Nagel (1992), Physics of Granular State, *Science*, *255*, 1523–1531.

Jeong, I., K. Lee, and J. Kim (2008), Characteristics of Auto-Ignition and Micro-Explosion Behavior of a Single Droplet of Water-in-Fuel, *J. Mechanical Science and Technology*, *22*, 148–156.

Jepsen, A. (2009), Characterization of Dynamic, Surfactant-free Emulsions, Master's thesis, University of California, Irvine, Irvine, USA.

Joseph, D., and Y. Renardy (1993), *Fundamentals of Two-Fluid Dynamics Part II: Lubricated Transport, Drops and Miscible Liquids*, 176 pp., Springer-Verlag, Brussels.

Kadota, T., H. Tanaka, D. Segawa, S. Nakaya, and H. Yamasaki (2007), Microexplosion of and Emulsion Droplet During Leidenfrost Burning, *Proceedings of the Combustion Iinstitute*, *31*, 2125–2131.

Kane, R. (1990), *Viscous Drag Reduction in Boundary Layers*, chap. Drag Reduction by Particle Addition.

Karabelas, A. (1978), Droplet Size Spectra Generated in Turbulent Pipe Flow of Dilute Liquid/Liquid Dispersions, *AIChE J.*, *24*(2), 170–180.

Kolmogorov, A. (1949), On the Breaking of Drops in Turbulent Flow, *Doklady Akad. Nauk.*, *66*, 825–828.

Kouba, G. (2003), Mechanistic models for droplet formation and breakup, in *Proceedings of ASME/JSME. Fluid Engineering Division Summer Meeting, Hawaii*, FEDSM2003-45542, pp. 1–9.

Kreith, F., and D. Goswami (Eds.) (2005), *The CRC Handbook of Mechanical Engineering, Second Edition*, CRC Press.

Krieger, I., and T. Dougherty (1959), A Mechanism for Non-Newtonian Flow in Suspensions of Rigid Spheres, *Transactions of the Society of Rheology*, *3*, 137–152.

Krynke, K., and J. Sek (2004), Predicting Viscosity of Emulsions in the Broad Range of Inner Phase Concentrations, *Colloids and Surfaces A: Physicochem. Eng. Aspects*, *245*, 81–92.

Kufferath, A., K. Ehrhardt, C. Heyse, and W. Leuckel (1999), Continuous Generation and Air-Assisted Atomization of Fuel Oil-Water-Emulsions, *Combustion Sci. and Tech.*, *143*, 17–26.

Kunitz, M. (1926), An Empirical Formula for the Relation Between Viscosity of Solution and Volume of Solute, *J. General Physiology*, *9*(6), 715–725.

Lamb, H. (1928), *Statics, Including Hydrostatics and the Elements of the Theory of Elasticity,3rd ed.*, Cambridge University Press, Cambridge, England:.

Law, C., C. Lee, and N. Srinivasan (1980), Combustion Characteristics of Water-in-Oil Droplets, *Combustion and Flame*, *37*, 125–143.

Leviton, A., and A. Leighton (1936), Viscosity Relationships in Emulsions Containing Milk Fat, *J. Physical Chemistry*, *40*, 71–80.

Lif, A., and K. Holmberg (2006), Water-in-Diesel Emulsions and Related Systems, *Advances in Colloid and Interface Sci.*, *123-126*, 231–239.

Lovick, J., A. Mouza, S. Paras, G. Lye, and P. Angeli (2005), Drop Size Distribution in Highly Concentrated LiquidLiquid Dispersions Using a Light Back Scattering Method, *J. Chemical Tech. & Biotechnology*, *80*, 1054–1060.

Maass, S., S. Horn, and M. Kraume (2008), Imaging Stratifying Liquid-Liquid Flow by Capacitance Tomography, *Czasopismo Techniczne*.

Mandal, T., D. Chakrabarti, and G. Das (2007), Oil Water Flow through Different Diameter Pipes Similarities and Differences, *Chem. Eng. Research and Design*, *85*(A8), 1123–1128.

Mattiello, M., L. Cosami, L. Pistone, F. Beretta, and P. Massoli (1992), Experimental evidence for microexplosions in water/fuel oil emulsion flames inferred by laser light scatteringn, in *Proceedings of the 24th Symposium (Internationa) on Combustion*, pp. 1573–1578, The Combustion Institute.

McCabe, W., and J. Smith (1967), *Unit Operations of Chemical Engineering, Second Edition*, McGraw-Hill Book Company.

McClements, D., and J. Coupland (1996), Theory of Droplet Size Distribution Measurements in Emulsions Using Ultrasonic Spectroscopy, *Colloids and Surfaces A: Physicochem. Eng. Aspects*, *117*, 161–170.

Metzner, A., and J. Reed (1955), Flow of Non-Newtonian Fluids-Correlation of the Laminar, Transition, and Turbulent-Flow Regions, *AIChE J.*, *1*(4), 434–440.

Mikielewicz, D. (2003a), Hydrodynamics and Heat Transfer in Bubbly Flow in the Turbulent Boundary Layer, *Int. J. Heat and Mass Transfer*, *46*, 207–220.

Mikielewicz, D. (2003b), Hydrodynamics and Heat Transfer in Bubbly Flow in the Turbulent Boundary Layer, *Int. J. Heat and Mass Transfer*, *46*, 207–220.

Mizutani, Y., M. Fuchihata, and M. Muraoka (2001), In Situ Observation of Microexplosion of Emulsion Droplets in Spray Flames, *Atomization and Sprays*, *11*, 521–532.

Moody, L. (1944), Friction Factors for Pipe Flow, *Transactions of the ASME*, *66*(8), 671–684.

Morrison, F. (2010), Data Correlation for Friction Factor in Smooth Pipes, *Department of Chemical Engineering, Michigan Technological University, Houghton, MI*.

Nadler, M., and D. Mewes (1997), Flow Induced Emulsification in the Flow of Two Immiscible Liquids in Horizontal Pipes, *Int. J. Multiphase Flow*, *23*(1), 55–68.

Nikuradse, J. (1933), Stromungsgesetz in rauhren rohren, vDI Forschungshefte 361. (English translation: Laws of flow in rough pipes), *Tech. rep.*, Technical report, NACA Technical Memorandum 1292. National Advisory Commission for Aeronautics (1950), Washington, DC.

Oldroyd, J. (1953), The Elastic and Viscous Properties of Emulsions and Suspensions, *Proceedings of the Royal Society of London. Series A*, *218*(1132), 122–132.

Oldroyd, J. (1955), The Effect of Interfacial Stabilizing Films on the Elastic and Viscous Properties of Emulsions, *Proceedings of the Royal Society of London. Series A*, *232*(1191), 567–577.

Omer, A. (2009), Pipeline Flow Behavior of Water-in-Oil Emulsions, Ph.D. thesis, University of Waterloo, Ontario, Canada.

Pacek, A., I. Moore, A. Nienow, and R. Calabrese (1994a), Video Technique for Measuring Dynamics of Liquid-Liquid Dispersion During Phase Inversion, *AIChE J.*, *40*(12).

Pacek, A., A. Nienow, and I. Moore (1994b), On the Structure of Turbulent Liquid-Liquid Dispersed Flows in an Agitated Vessel, *Chemical Eng. Sci.*, *29*(20).

Pal, R. (1987), Emulsions: Pipeline Flow Behavior, Viscosity Equations and Flow Measurement, Ph.D. thesis, University of Waterloo, Canada.

Pal, R. (1993), Pipeline Flow of Unstable and Surfactant Stabilized Emulsions, *AIChE J.*, *39*(11), 1754–1764.

Pal, R. (2000), Shear Viscosity Behavior of Emulsions of Two Immiscible Liquids, *J. Colloid & interface Sci.*, *225*, 359–366.

Pal, R. (2003), Viscous Behavior of Concentrated Emulsions of Two Immiscible Newtonian Fluids with Interfacial Tension, *J. Colloid & interface Sci.*, *263*, 296–305.

Pal, R. (2007), Mechanism of Turbulent Drag Reduction in Emulsions and Bubbly Suspensions, *Ind. Eng. Chem. Res.*, *46*, 618–622.

Palierne, J. (1990), Linear Rheology of Viscoelastic Emulsions with Interfacial Tension, *Rheologica Acta*, *29*, 204–214.

Park, J., K. Huh, and J. Lee (2001), Reduction of NO_x, Smoke and Break Specific Fuel Consumption with Optimal Injection Timing and Emulsion Ratio of Water-Emulsified Diesel, *Proc. Instn. Mech. Engrs. Part D*, *215*, 618–622.

Pouplin, A., O. Masbernat, S. Decarre, and A. Line (2010), Wall Friction and Effective Viscosity of a Homogeneous Dispersed Liquid-Liquid Flow in a Horizontal Pipe, *AIChE*.

Prince, L. (1977), *Microemulsions Theory and Practice*, Academic Press, New York.

Rajapakse, A. (2007), Drop Size Distributions and Interfacial Area in Reactive Liquid-Liquid Dispersions, Ph.D. thesis, RMIT University, Melbourne, Australia.

Reed, B., J. Hokanson, O. Hamann, and T. Montague (1998), System for Acquiring an Image of a Multi-Phase Fluid by Measuring Backscattered Light, United States Patent, no. 5,815,264.

Richter, A., T. Voigt, and M. Ripperger (2007), Ultrasonic Attenuation Spectroscopy of Emulsions with Droplet Sizes Greater than 10 μm, *J. Colloid and Interface Sci.*, *315*, 482–492.

Ritter, J., and M. Kraume (2000), On-line Measurement Technique for Drop Size Distributions in Liquid/Liquid Systems at High Dispersed Phase Fractions, *Chemical Eng. Tech.*, *23*, 579–581.

Schwartz, F., and M. Braun (1999), Apparatus for Measuring Particle Dimensions in Fluids, United States Patent, no. 5,900,933.

Simmons, M., and B. Azzopardi (2001), Drop Size Distributions in Dispersed Liquid-Liquid Pipe Flow, *Int. J. Multiphase Flow*, *27*, 843–859.

Simmons, M., P. Langston, and A. Burbidge (1999), Particle and Droplet Size Analysis from Chord Distributions, *Powder Tech.*, *102*, 75–83.

Simmons, M., S. Zaidi, and B. Azzopardi (2000), Comparison of Laser-Based Drop-Size Measurement Techniques and Their Application to Dispersed Liquid-Liquid Pipe Flow, *Optical Eng.*, *39*(2).

Taboada, B., L. Vega-Alvarado, M. Vega-Alvarado, E. Galindo, and G. Corkidi (2006), Semi-Automatic Image Analysis Methodology for the Segmentation of Bubbles and Drops in Complex Dispersions Occurring in Bioreactors, *Experiments in Fluids*, *41*, 383–392.

Tajima, H., K. Takasaki, M. Nakashima, K. Kawano, M. Ohishi, J. Yanagi, and S. Osafune (2001), Visual study on combustion of low-grade fuel water emulsion, in *The Fifth International Symposium on Diagnostics and Modeling of Combustion in Internal Combustion Engines*, 1-02, pp. 44–49.

Taylor, G. (1932), The Viscosity of a Fluid Containing Small Drops of Another Fluid, *Proceedings of the Royal Society of London. Series A*, *138*(834), 41–48.

Thomas, D. (1962), Transport Characteristics of Suspensions: Part VI. Minimum Transport Velocity for Large Particle Size Suspensions in Round Horizontal Pipes, *AIChE J.*, *8*(3), 373–378.

Torres-Monzon, C. (2006), Modeling of Oil-Water Flow in Horizontal and Near Horizontal Pipes, Ph.D. thesis, The University of Tulsa, Tulsa, Oklahoma.

Vand, V. (1948), Viscosity of Solutions and Suspensions, *J. Physical Chemistry*, *52*, 277–299.

Vassen, G., and H. Stein (1995), The Applicability of Catastrophe Theory to Emulsion Phase Inversion, *J. Colloid and Interface Sci.*, *176*, 378–387.

Vielma, J. (2006), Rheological Behavior of Oil-Water Dispersion Flow in Horizontal Pipes, Master's thesis, The University of Tulsa, Tulsa, Oklahoma.

Wang, C., and J. Chen (1996), An Experimental Investigation of the Burning Characteristics of Water-Oil Emulsions, *Int. Comm. Heat Mass Transfer*, *23*(6), 823–834.

Ward, J. (1964), Turbulent Flow of Liquid-Liquid Dispersions: Drop Size, Friction Losses, and Velocity Distributions, Ph.D. thesis, Oregon State University, Oregon, USA.

Ward, J., and J. Knudsen (1967), Turbulent Flow of Unstable Liquid-Liquid Dispersions: Drop Sizes and Velocity Distributions, *AIChE J.*, *13*(2), 356–365.

Wegmann, A., and P. von Rohr (2006), Two Phase Liquid-Liquid Flows in Pipes of Small Diameters, *Int. J. Multiphase Flow*, *32*, 1017–1028.

White, F. (2006), *Viscous Fluid Flow*, McGraw-Hill, New York.

Xu, X. (2007), Study on Oil-Water Two-Phase Flow in Horizontal Pipelines, *J. Petroleum Sci. and Eng.*, *59*, 43–58.

Yaron, I., and B. Gal-Or (1972), On Viscous Flow and Effective Viscosity of Concentrated Suspensions and Emulsions, *Rheologica Acta*, *11*, 241–252.

Zabulis, X., M. Papara, A. Chatziargyriou, and T. Karapantsios (2007), Detection of Densely Dispersed Spherical Bubbles in Digital Images Based on a Template Matching Technique Application to Wet Foams, *Colloids and Surfaces A: Physicochem. Eng. Aspects*, *309*, 96–106.

APPENDICES

APPENDIX A

Pipe Flow Fundamentals

The Friction Factor

As can be found in any standard fluid mechanics text book (e.g. *White* (2006)), in a Hagen-Poiseuille flow through a circular pipe, the cross-sectional velocity distribution is given as:

$$u = \frac{-\mathbf{d}p/\mathbf{d}x}{4\mu}\left[\left(\frac{D}{2}\right)^2 - r^2\right] \tag{A.1}$$

And the volumetric flow rate is given as:

$$Q = \frac{\pi D^4}{128\mu}\left(-\frac{\mathbf{d}p}{\mathbf{d}x}\right) \tag{A.2}$$

The mean velocity U can be found by diving Q with the cross-sectional area:

$$U = \frac{D^2}{32\mu}\left(\frac{-\mathbf{d}p}{\mathbf{d}x}\right) \tag{A.3}$$

The wall shear stress then becomes proportional to the mean velocity:

$$\tau_w = \mu\left(\frac{\mathbf{d}u}{\mathbf{d}r}\right) \tag{A.4a}$$

$$\tau_w = \frac{1}{4}D\left(-\frac{\mathbf{d}p}{\mathbf{d}x}\right) \tag{A.4b}$$

$$\tau_w = \frac{8\mu U}{D} \tag{A.4c}$$

The friction factor (aka skin-friction coefficient) named after Fanning is the nondimensionalization of the wall shear stress with the pipe dynamic pressure[1].

$$f = \frac{\tau_w}{\rho U^2/2} \tag{A.5}$$

Hence, in a Hagen-Poiseuille flow, the friction factor becomes:

$$f = \frac{16}{Re} \tag{A.6}$$

A phenomenological friction factor can also be obtained through a less rigorous dimensional analysis. Δp, the pressure drop between two points along a straight pipe section of constant cross-sectional area (with no gravitational potential difference), should be proportional to $\rho\frac{U^2}{2}$ on dimensional bases (both being energy per unit volume), the pressure drop is also proportional to the distance between the two points L, which can be normalized by the pipe diameter, thus it can be stated:

[1]Note that this is an arbitrary definition. We could have chosen instead to normalize by a different quantity, like the average kinetic energy of the fluid $\rho\frac{\bar{u}^2}{2}$

$$\Delta p \propto \rho \frac{U^2}{2} \frac{L}{D} \tag{A.7}$$

F, the proportionality constant of Equation A.7, is known as the Darcy-Weisbach friction factor.

$$F = 2 \frac{\Delta p}{\rho U^2} \frac{D}{L} \tag{A.8}$$

From Equations A.4b and A.5:

$$f = \frac{D}{2\rho U^2} \left(\frac{\mathbf{d}p}{\mathbf{d}x} \right) \tag{A.9}$$

$$f = \frac{F}{4} \tag{A.10}$$

In the turbulent regime, where the Hagen-Poiseuille flow assumptions are not valid, no theoretically derivable relationship can give the friction factor in "easily measurable" terms. Blasius formulated Equation A.11 from his experimental data on turbulent flow in smooth pipes, which has since become one of the most widely accepted reference curves for f in the turbulent regime.

$$f = \frac{0.079}{Re^{0.25}} \tag{A.11}$$

The viscosity on which the *Re* is based in Equation A.11 was defined for laminar, Newtonian flows as the proportionality constant relating the shear stress to the rate of strain. However, in Equation A.11 and from Equation A.5 we have:

$$\tau_w \propto \frac{\rho U^2}{Re^{0.25}} \tag{A.12a}$$

$$\mu_{turbulent} \propto \rho U D \frac{\tau_w^4}{\rho^4 U^8} \tag{A.12b}$$

$$\mu_{turbulent} \propto \frac{\tau_w^4 D}{\rho^3 U^7} \tag{A.12c}$$

$$\mu_{turbulent} \propto \left(\frac{\tau_w}{\rho U^2}\right)^3 \frac{\tau_w}{U/D} \tag{A.12d}$$

$$\mu_{turbulent} \propto (f)^3 \mu_{laminar} \tag{A.12e}$$

Nikuradse (1933) obtained friction factor data for turbulent flows in artificially roughened pipes, where sand grains of uniform roughness were glued to smooth pipes. The friction factor data was obtained at different roughness-to-diameter ϵ/D ratios. These sets of data had since been the golden standard against which experiments are compared.

Colebrook (1939) devised the formal of Equation A.13 for commercial pipes that have roughness not necessarily of uniform nature like the ones used by Nikuradse. *Moody* (1944) plotted this relationship in a diagram similar to Figure A.1, which is celebrated after him.

$$\frac{1}{\sqrt{f}} = -4.0log\left(\frac{\epsilon}{3.7D} + \frac{1.255}{Re\sqrt{f}}\right) \tag{A.13}$$

Generalized Reynolds Number

The viscosity of non-Newtonian fluids is a function of shear rate. In the absence of elasticity forces, and for fluids whose behavior is time independent, *Metzner and Reed* (1955) developed the expression of Equation A.14 to correlate the friction factor and the flow rate of these fluids.

$$Re_{Gen} = \frac{\rho D^{\hat{n}} U^{(2-\hat{n})}}{8^{(\hat{n}-1)}\hat{k}} \tag{A.14}$$

where $\hat{n}$ is the flow behavior index that characterized the degree of non-Newtonian behavior of the fluid (the further $\hat{n}$ from unity, the more non-Newtonian the fluid). $\hat{k}$ is the consistency index, the larger $\hat{k}$ the "more viscous" the fluid. $\hat{n}$ and $\hat{k}$ might be constant over certain ranges of shear rates but are not necessarily constants. For unity flow behavior index the generalized Reynolds number reduces to the Reynolds number of a Newtonian fluid with a viscosity equal to the value consistency index.

Law-of-the-wall

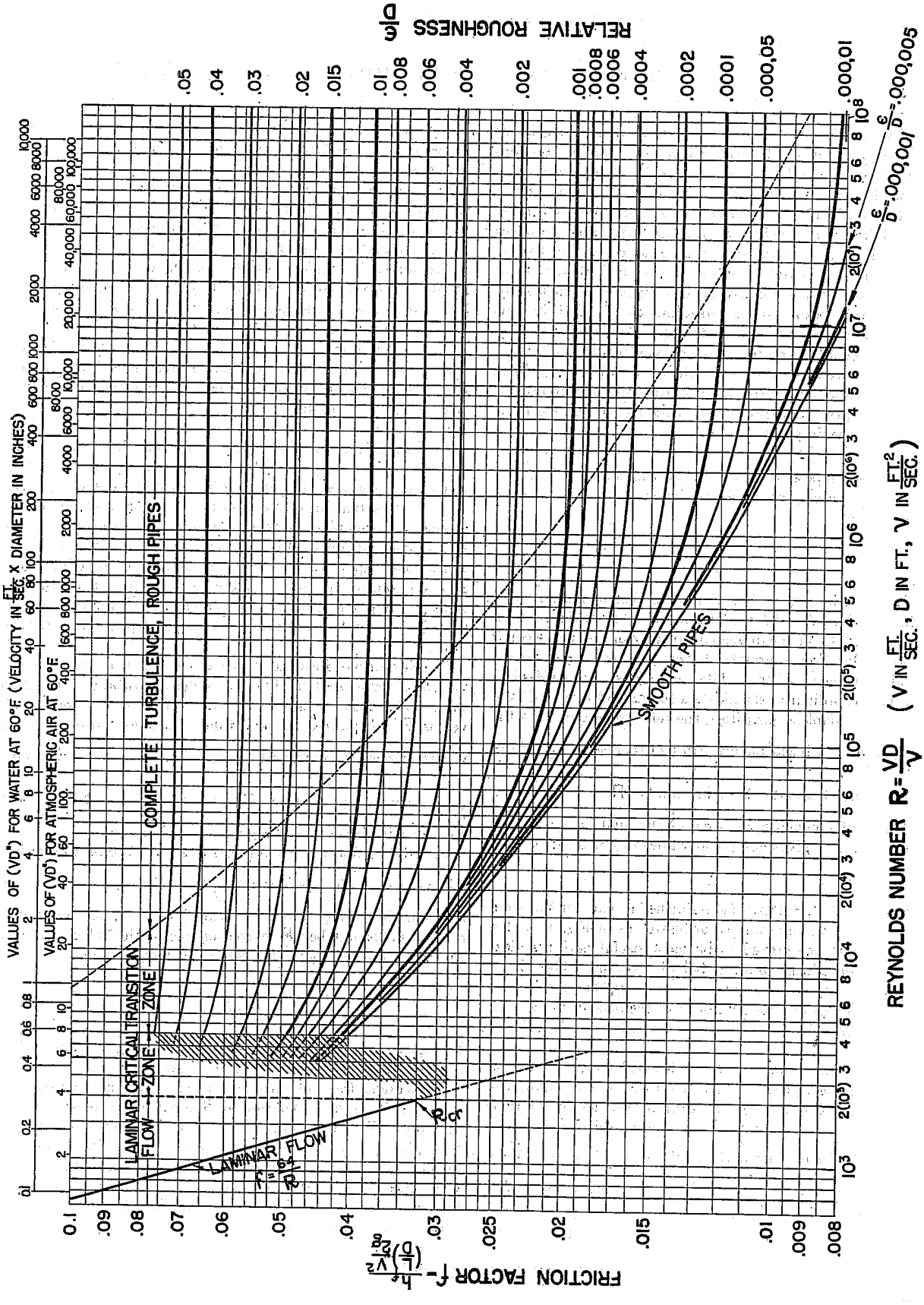

Figure A.1: Fiction factor of turbulent, single phase flows in pipes of different roughness (*Colebrook*, 1939).

The "law of the wall" gives the velocity profile in a turbulent flow

$$u^+ = A \log y^+ + B \qquad \text{Law of the wall} \qquad \text{(A.15a)}$$

$$where: \; u^+ = \frac{u}{u^*} \qquad \text{dimensionless velocity} \qquad \text{(A.15b)}$$

$$y^+ = \frac{\rho y u^*}{\mu} \qquad \text{dimensionless distance from the wall} \qquad \text{(A.15c)}$$

$$u^* = \sqrt{\frac{\tau_w}{\rho}} \qquad \text{frictional velocity} \qquad \text{(A.15d)}$$

$$y = R - r \qquad \text{distance from the wall} \qquad \text{(A.15e)}$$

in the case of two-phase flows, both A and B are functions of ϕ.

APPENDIX B

Silicon Oil Properties

Viscosity

The viscosity of the PDMS oil was measured using an Anton-Paar Physica MCR301 rheometer, over a range of shear rates of 10 to 300 1/s. The results are shown in Figure B.1. The average for the unused oil viscosity is 6.61 mPa.s and for the used oil 6.81 mPa.s. Therefore, the average of these two, 6.71 mPa.s will be taken as the real viscosity of the oil.

Interfacial Tension with Water

The interfacial tension of the oil and water was measured by solving the hydrostatic Young-Laplace equations (*Lamb*, 1928) that define the shape of a pending drop of one liquid into the other. The solution of the equations was done through a routine written by Justin Burton. Figure B.2 shows the calculated curvature matching that obtained by a photograph of a drop of PDMS suspended in water shown in Figure B.3. The oil was sampled from the oil tank after having been mixed with water for several testing rounds.

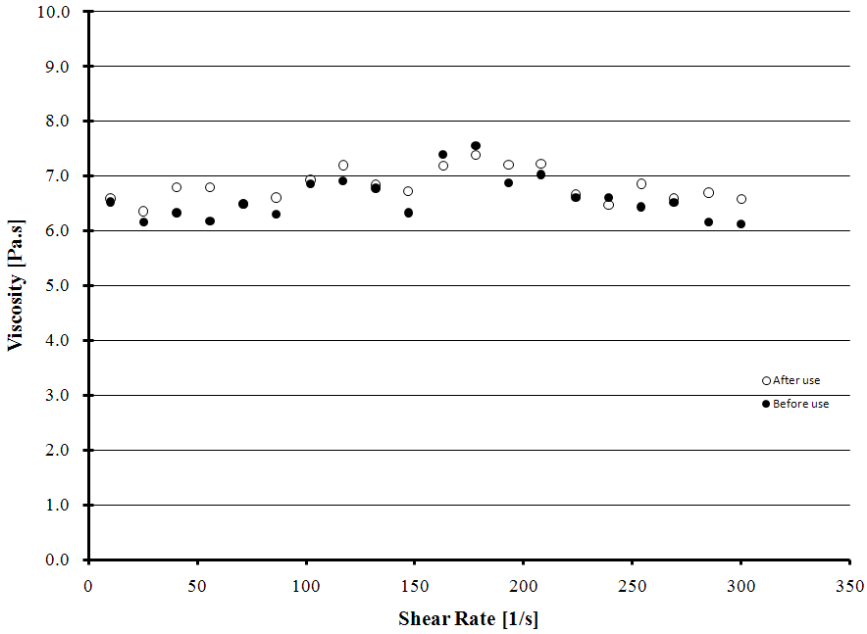

Figure B.1: Comparison of the viscosity of PDMS before and after being used in the experiments.

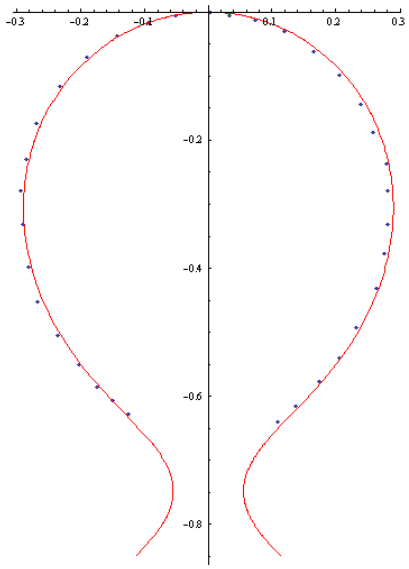

Figure B.2: Comparison of the calculated shape of the drop (red) to points on the perimeter of the photographed drop (blue).

Figure B.3: The photograph of the PDMS droplet surrounded by water, used in determining the interfacial tension between the two.

APPENDIX C

Normalized Pressure Drop per Unit Tube Length

The pressure drop across a unit length of tube, normalized by the corresponding pressure drop of oil-only flow, is plotted as a function of ϕ_w at different mixture velocities. The values of the oil-only pressure drop are obtained from the equation corresponding to the curve fitted to the measured values of oil-only flow. This curve appears in Figure 5.4, given in Equation C.1. Pressure drop follows closely the values expected from the Blasius curve (Equation C.2).

$$\frac{\delta P}{\delta L} = 1419.5 U_m^{1.7807} \tag{C.1}$$

$$\frac{\delta P}{\delta L} = 1464.5 U_m^{1.75} \tag{C.2}$$

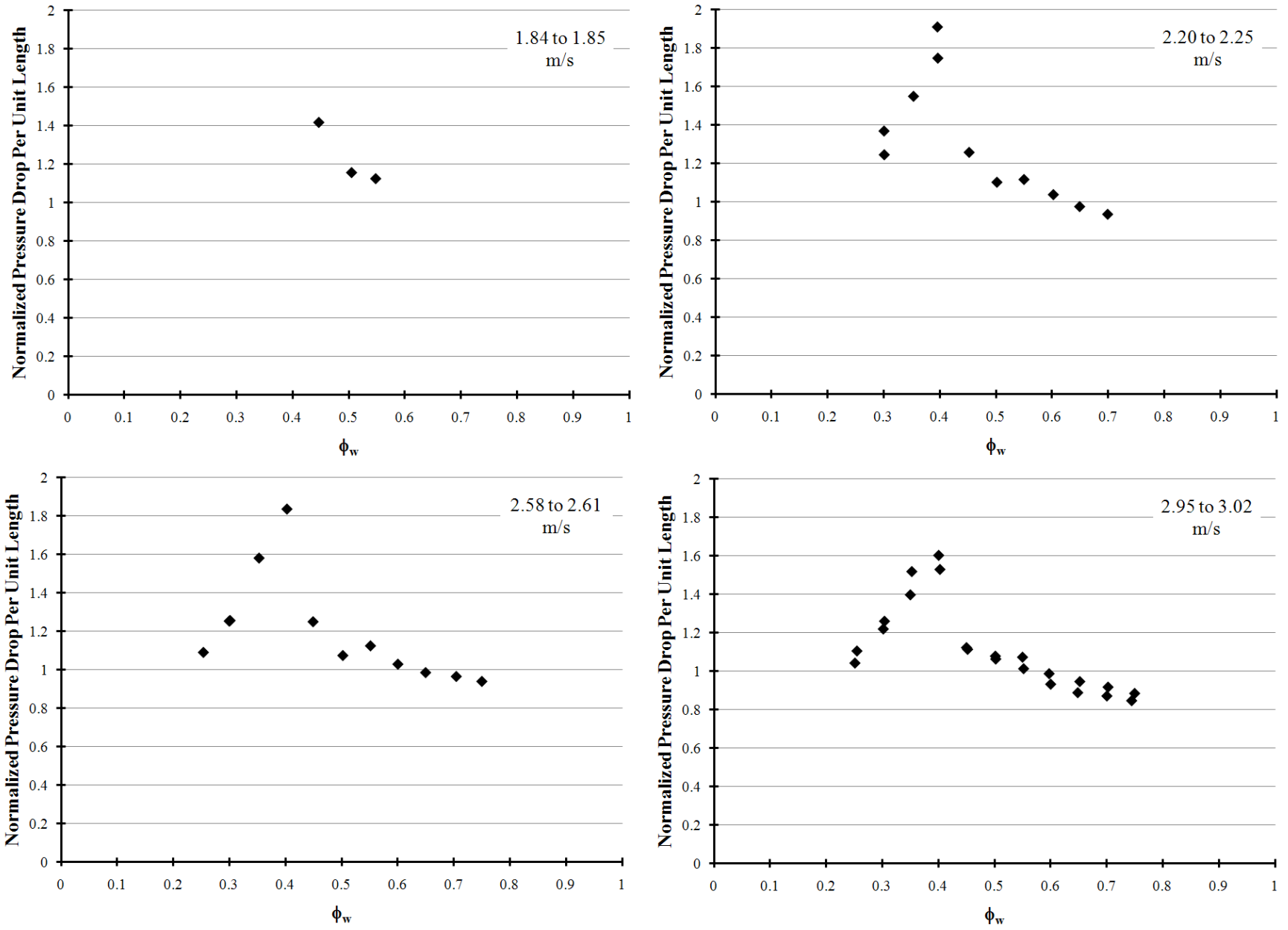

Figure C.1: Pressure drop per unit pipe length [Pa/m], normalized by oil-only pressure drop for U_m = 1.8, 2.2, 2.6 and 2.9 m/s, as a function of ϕ_w.

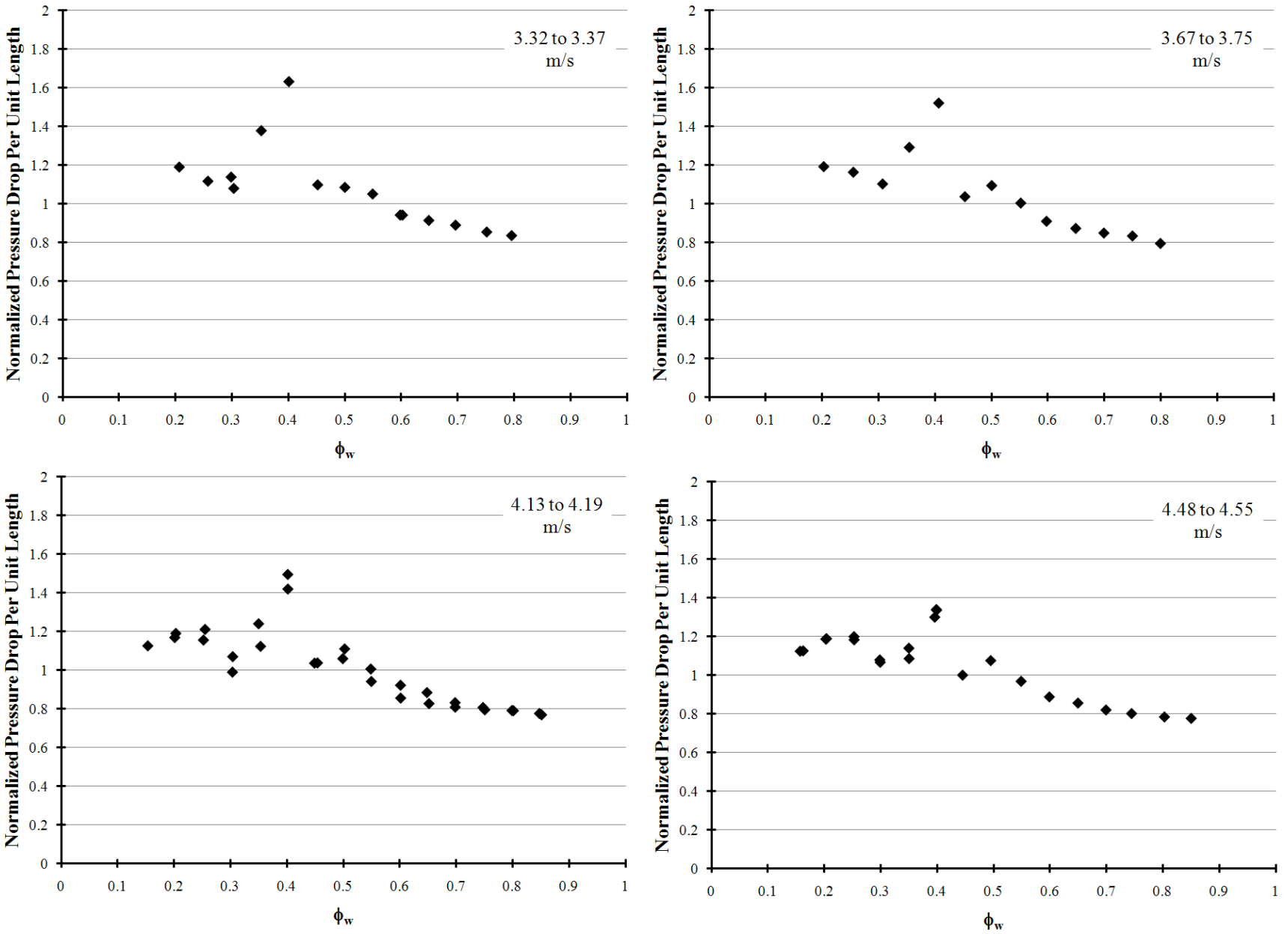

Figure C.2: Pressure drop per unit pipe length [Pa/m], normalized by oil-only pressure drop for U_m = 3.3, 3.7, 4.1 and 4.5 m/s, as a function of ϕ_w.

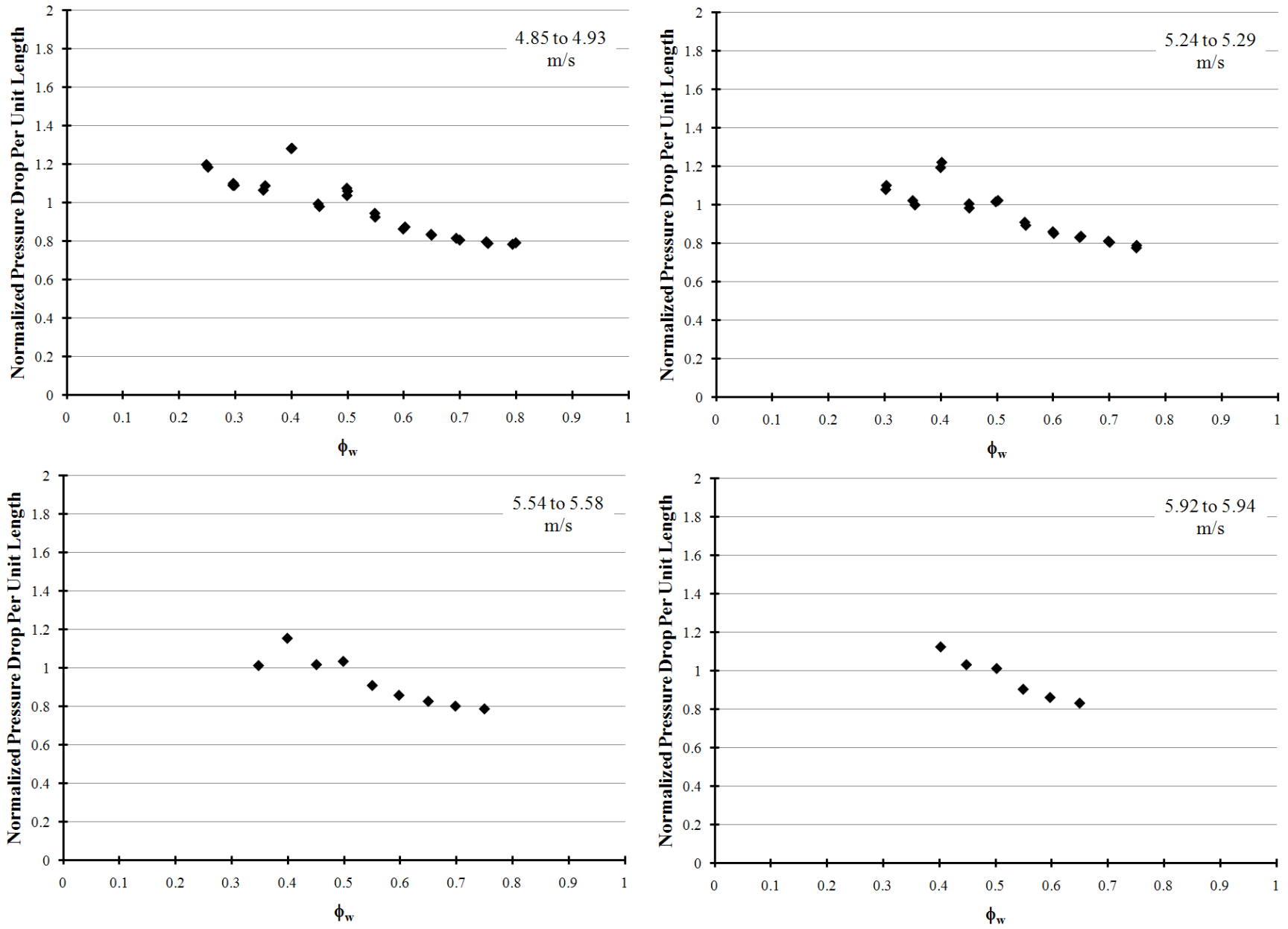

Figure C.3: Pressure drop per unit pipe length [Pa/m], normalized by oil-only pressure drop for U_m = 4.9, 5.2, 5.5 and 5.9 m/s , as a function of ϕ_w.

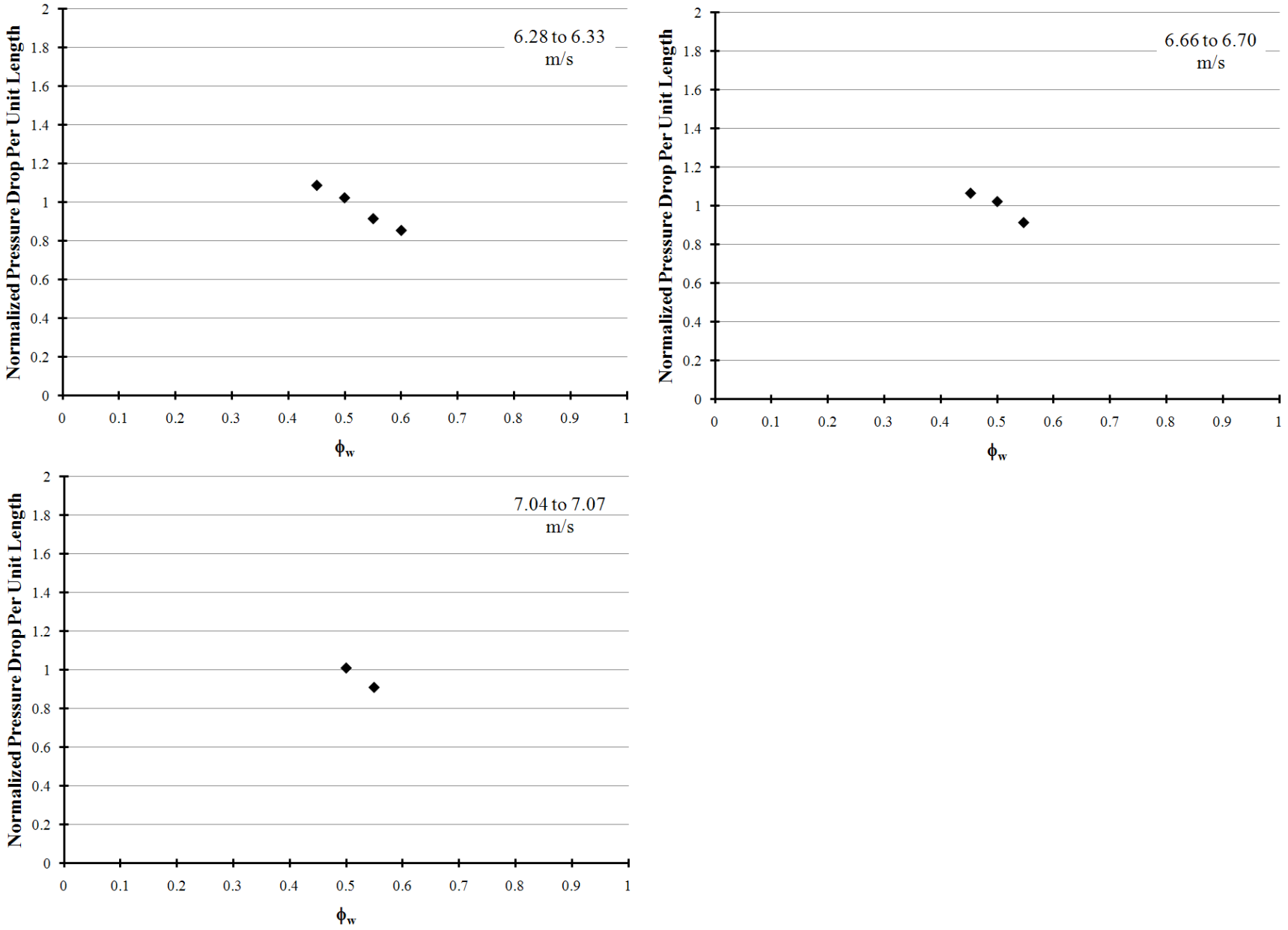

Figure C.4: Pressure drop per unit pipe length [Pa/m], normalized by oil-only pressure drop for U_m = 6.3, 6.7 and 7 m/s, as a function of ϕ_w.

APPENDIX D

Raw Experimental Data

This Appendix lists the raw data. The appendix first lists the single phase data for pressure drop along the pipe, and then for pressure drop across the safety screen assembly with and without the safety screen. Then the two phase results of pressure drop long the pipe, and across the safety screen assembly with and without the safety screen. The flow rate data is given in Gallons per minute [GPM], as obtained from the measuring devices, while pressure drop was divided by the pipe length to give pressure drop per unit pipe length.

Table D.1: Pressure drop per unit pipe length for water

Test No.	Water Flow Rate [GPM]	$\frac{\Delta P}{\Delta L}$ [$\frac{Pa}{m}$]
1	11.067	4 302.94
2	10.036	8 771.21
3	9.064	13 239.47
4	8.062	17 707.74
5	7.026	22 176.00
6	6.142	26 644.27
7	5.240	31 112.53
8	4.101	35 580.80
9	3.100	40 049.06
10	2.208	44 517.33
11	2.299	48 985.60
12	3.044	53 453.86
13	4.110	57 922.13
14	5.240	62 390.39
15	6.146	66 858.66
16	7.073	71 326.92
17	8.077	75 795.19
18	9.031	80 263.46
19	10.032	84 731.72
20	11.021	89 199.99
38	11.456	169 628.77
39	12.248	174 097.03
40	12.975	178 565.30
41	12.953	183 033.57
42	2.124	187 501.83
43	2.829	191 970.10
44	3.673	196 438.36
45	4.682	200 906.63

Table D.2: Pressure drop per unit pipe length for oil

Test No.	Oil Flow Rate [GPM]	$\frac{\Delta P}{\Delta L}$ [$\frac{Pa}{m}$]
21	10.196	15 215.06
22	9.068	12 286.94
23	8.016	9 872.91
24	7.037	7 807.32
25	6.070	6 024.75
26	5.084	4 445.27
27	4.051	2 950.95
28	3.025	1 745.13
29	2.098	815.96
30	10.161	15 004.05
31	9.045	12 131.82
32	8.024	9 803.65
33	7.016	7 715.02
34	6.047	5 975.70
35	5.089	4 402.40
36	4.037	2 945.13
37	3.029	1 769.54
46	3.514	2 367.29
47	3.871	2 808.12
48	4.563	3 728.23
49	4.889	4 157.28
50	1.670	646.61
51	1.718	637.02
52	1.812	675.44
53	1.923	726.50
54	2.009	776.37
55	2.098	821.87
56	2.211	907.72
57	2.330	1 058.85
58	2.447	1 189.60
59	2.562	1 295.55
60	2.672	1 412.32
61	2.764	1 524.95
62	2.854	1 613.76
63	2.936	1 700.09
64	3.034	1 798.29
65	2.280	1 033.76
66	3.148	2 013.35
67	3.224	2 069.03
68	3.311	2 168.86
69	3.440	2 314.78
70	3.513	2 387.60
71	3.633	2 517.81

Table D.3: Pressure drop across the safety screen assembly without the safety screen for water

Test No.	Water Flow Rate [GPM]	[Pa]
1	11.067	16 748.76
2	10.036	13 971.33
3	9.064	11 524.96
4	8.062	9 087.32
5	7.026	6 837.29
6	6.142	5 231.45
7	5.240	3 681.45
8	4.101	2 153.51
9	3.100	1 230.14
10	2.208	556.63
38	11.456	19 299.19
39	12.248	22 027.57
40	12.975	24 223.86
41	12.953	24 212.62
42	2.124	856.12
43	2.829	1 520.21
44	3.673	2 441.45
45	4.682	3 661.68

Table D.4: Pressure drop across the safety screen assembly without the safety screen for oil

Test No.	Oil Flow Rate [GPM]	[Pa]
30	10.161	14 131.29
31	9.045	11 222.53
32	8.024	8 888.12
33	7.016	6 888.27
34	6.047	5 274.36
35	5.089	3 832.21
36	4.037	2 546.22
37	3.029	1 618.43
46	3.514	2 143.87
47	3.871	2 486.21
48	4.563	3 445.11
49	4.889	3 807.86
50	1.670	925.64
51	1.718	924.55
52	1.812	1 051.15
53	1.923	1 162.68
54	2.009	1 217.14
55	2.098	1 336.00
56	2.211	1 446.81
57	2.330	1 441.55
58	2.447	1 459.18
59	2.562	1 475.18
60	2.672	1 473.29
61	2.764	1 553.80
62	2.854	1 601.91
63	2.936	1 627.62
64	3.034	1 777.47
65	2.280	1 494.92
66	3.148	1 878.90
67	3.224	2 012.37
68	3.311	2 045.70
69	3.440	2 121.15
70	3.513	2 188.55
71	3.633	2 326.48

Table D.5: Pressure drop across the safety screen assembly with the safety screen for water

Test No.	Water Flow Rate [GPM]	[Pa]
11	2.299	2 378.57
12	3.044	4 084.29
13	4.110	7 066.71
14	5.240	11 091.72
15	6.146	14 963.80
16	7.073	19 517.39
17	8.077	24 969.97
18	9.031	30 578.02
19	10.032	37 325.35
20	11.021	44 220.60

Table D.6: Pressure drop across the safety screen assembly with the safety screen for oil

Test No.	Oil Flow Rate [GPM]	[Pa]
21	10.196	53 364.67
22	9.068	43 833.05
23	8.016	36 115.62
24	7.037	29 538.20
25	6.070	23 828.08
26	5.084	18 623.48
27	4.051	13 644.24
28	3.025	9 583.29
29	2.098	6 451.30

Table D.7: Pressure drop per unit pipe length, nominal mixture flow rate 5 [GPM]

Test No.	Oil Flow Rate [GPM]	Water Flow Rate [GPM]	$\frac{\Delta P}{\Delta L}$ [$\frac{Pa}{m}$]
1	2.251	2.730	4 745.28
2	2.766	2.235	6 020.37
3	2.477	2.529	4 922.87

Table D.8: Pressure drop per unit pipe length, nominal mixture flow rate 6 [GPM]

Test No.	Oil Flow Rate [GPM]	Water Flow Rate [GPM]	$\frac{\Delta P}{\Delta L}$ [$\frac{Pa}{m}$]
4	3.597	2.363	10 160.23
5	3.620	2.372	11 208.79
6	4.194	1.803	8 045.02
7	1.809	4.209	5 532.92
8	3.903	2.131	9 205.50
9	2.118	3.926	5 813.19
10	4.227	1.820	7 426.46
11	2.720	3.328	6 662.56
12	3.313	2.737	7 508.15
13	2.404	3.646	6 196.40
14	3.031	3.055	6 647.65

Table D.9: Pressure drop per unit pipe length, nominal mixture flow rate 7 [GPM]

Test No.	Oil Flow Rate [GPM]	Water Flow Rate [GPM]	$\frac{\Delta P}{\Delta L}$ [$\frac{Pa}{m}$]
15	4.886	2.091	9 640.61
16	2.453	4.554	7 638.16
17	4.899	2.112	9 745.34
18	2.803	4.212	7 995.97
19	1.754	5.267	7 308.30
20	3.872	3.157	9 744.57
21	4.200	2.830	14 315.93
22	4.550	2.481	12 330.83
23	3.501	3.534	8 386.79
24	3.157	3.884	8 792.35
25	5.256	1.786	8 529.31
26	2.086	4.974	7 582.89

Table D.10: Pressure drop per unit pipe length, nominal mixture flow rate 8 [GPM]

Test No.	Oil Flow Rate [GPM]	Water Flow Rate [GPM]	$\frac{\Delta P}{\Delta L}$ $[\frac{Pa}{m}]$
27	2.376	5.615	8 979.22
28	3.596	4.399	10 513.48
29	2.785	5.226	9 303.24
30	5.577	2.440	12 411.86
31	5.188	2.831	14 967.23
32	6.003	2.017	10 271.84
33	3.228	4.796	9 735.31
34	5.601	2.425	12 037.18
35	4.791	3.236	15 101.63
36	3.210	4.825	9 214.64
37	4.400	3.635	11 012.10
38	4.005	4.035	10 674.64
39	4.807	3.264	14 200.81
40	2.835	5.236	8 850.61
41	4.437	3.635	11 193.72
42	2.418	5.657	8 686.27
43	5.248	2.831	13 954.78
44	3.620	4.464	10 123.71
45	2.021	6.068	8 845.76
46	4.027	4.067	10 651.52
47	4.855	3.249	16 099.74
48	2.073	6.050	8 532.52
49	6.077	2.082	11 231.15

Table D.11: Pressure drop per unit pipe length, nominal mixture flow rate 9 [GPM]

Test No.	Oil Flow Rate [GPM]	Water Flow Rate [GPM]	$\frac{\Delta P}{\Delta L}$ $[\frac{Pa}{m}]$
50	4.045	4.931	12 674.97
51	5.824	3.160	16 638.32
52	3.156	5.837	11 061.60
53	2.233	6.763	10 349.21
54	6.274	2.727	13 085.27
55	4.505	4.508	13 181.71
56	4.950	4.079	13 383.19
57	3.593	5.441	11 490.25
58	2.754	6.320	10 943.57
59	6.748	2.335	13 758.00
60	1.854	7.232	10 304.02
61	7.217	1.876	14 684.21
62	5.450	3.644	20 130.95
63	3.658	5.447	11 655.88
64	6.394	2.717	14 096.31

Table D.12: Pressure drop per unit pipe length, nominal mixture flow rate 10 [GPM]

Test No.	Oil Flow Rate [GPM]	Water Flow Rate [GPM]	$\frac{\Delta P}{\Delta L}$ $[\frac{Pa}{m}]$
65	2.483	7.459	12 067.00
66	3.000	6.983	12 378.40
67	7.977	2.026	17 435.25
68	4.999	5.009	16 020.92
69	3.510	6.505	12 797.30
70	7.491	2.563	17 170.77
71	2.021	8.069	11 813.33
72	6.516	3.575	19 191.37
73	4.521	5.572	14 918.54
74	6.009	4.114	22 718.27
75	5.540	4.586	15 502.04
76	7.020	3.109	16 492.18
77	4.080	6.062	13 638.75

Table D.13: Pressure drop per unit pipe length, nominal mixture flow rate 11.2 [GPM]

Test No.	Oil Flow Rate [GPM]	Water Flow Rate [GPM]	$\frac{\Delta P}{\Delta L}$ $[\frac{Pa}{m}]$
78	3.367	7.790	14 762.54
79	2.818	8.348	14 341.72
80	2.218	8.955	14 062.74
81	3.931	7.249	15 748.79
82	4.457	6.731	16 442.90
83	1.662	9.530	13 725.06
84	7.241	3.963	20 081.73
85	5.612	5.596	18 952.57
86	3.903	7.311	14 810.92
87	6.177	5.038	18 552.82
88	9.493	1.727	20 176.40
89	7.808	3.416	19 190.41
90	6.720	4.514	26 856.92
91	6.718	4.517	25 501.96
92	2.801	8.438	14 293.34
93	3.390	7.850	14 536.00
94	4.477	6.765	15 390.72
95	2.260	8.982	14 238.37
96	6.133	5.110	18 665.65
97	8.982	2.269	21 048.35
98	7.311	3.941	22 335.32
99	1.716	9.543	13 998.16
100	5.085	6.186	18 176.73
101	7.848	3.426	17 891.55
102	5.075	6.200	17 023.49
103	8.984	2.296	21 535.82
104	8.432	2.850	20 915.26
105	8.438	2.894	22 084.93
106	5.641	5.699	20 274.67

Table D.14: Pressure drop per unit pipe length, nominal mixture flow rate 12.2 [GPM]

Test No.	Oil Flow Rate [GPM]	Water Flow Rate [GPM]	$\frac{\Delta P}{\Delta L}$ $[\frac{Pa}{m}]$
107	7.323	4.793	26 731.36
108	3.650	8.482	16 916.64
109	3.102	9.040	16 558.67
110	1.820	10.327	16 053.42
111	10.244	1.907	23 236.13
112	10.191	1.974	23 321.40
113	5.494	6.678	20 083.97
114	7.912	4.262	22 525.87
115	7.323	4.858	27 744.63
116	8.552	3.632	22 419.74
117	7.345	4.862	27 916.84
118	4.280	7.929	17 850.67
119	4.899	7.311	18 519.02
120	8.573	3.654	22 300.92
121	6.792	5.443	20 938.30
122	9.763	2.477	24 855.29
123	9.159	3.097	24 831.43
124	9.166	3.094	25 193.94
125	6.198	6.072	22 628.60
126	2.421	9.852	16 508.16
127	7.985	4.294	24 001.90
128	9.793	2.505	25 106.54

Table D.15: Pressure drop per unit pipe length, nominal mixture flow rate 13.2 [GPM]

Test No.	Oil Flow Rate [GPM]	Water Flow Rate [GPM]	$\frac{\Delta P}{\Delta L}$ $[\frac{Pa}{m}]$
129	9.228	3.879	25 747.54
130	9.238	3.898	25 943.81
131	9.223	3.924	25 890.68
132	9.258	3.904	26 197.16
133	7.281	5.902	23 738.48
134	5.949	7.246	22 135.00
135	7.258	5.937	23 445.41
136	2.645	10.555	18 968.72
137	4.626	8.578	19 931.71
138	3.301	9.905	18 909.94
139	5.299	7.918	20 723.66
140	3.968	9.250	19 353.33
141	7.923	5.302	30 794.58
142	5.973	7.258	22 719.14
143	4.648	8.587	20 106.83
144	9.954	3.297	28 856.23
145	4.063	9.190	19 669.09
146	7.958	5.300	30 870.47
147	8.618	4.643	25 690.02
148	8.578	4.690	26 282.19
149	5.276	7.994	21 128.56
150	9.940	3.342	28 639.86
151	6.662	6.638	25 158.40
152	3.365	9.945	19 380.73
153	6.664	6.667	25 823.25
154	6.683	6.648	26 187.81
155	2.750	10.591	19 144.41

Table D.16: Pressure drop per unit pipe length, nominal mixture flow rate 14.2 [GPM]

Test No.	Oil Flow Rate [GPM]	Water Flow Rate [GPM]	$\frac{\Delta P}{\Delta L}$ $[\frac{Pa}{m}]$
156	3.557	10.597	21 006.40
157	3.554	10.614	21 407.63
158	4.236	9.942	21 863.20
159	5.676	8.507	23 388.14
160	4.275	9.916	22 072.68
161	9.904	4.288	29 414.77
162	6.365	7.828	24 325.75
163	5.005	9.192	22 606.29
164	4.971	9.232	22 795.64
165	7.132	7.079	27 753.67
166	6.402	7.816	24 847.23
167	5.668	8.556	23 256.00
168	7.816	6.410	27 518.19
169	8.508	5.719	33 444.23
170	8.555	5.698	32 791.20
171	7.101	7.162	28 107.67
172	9.278	5.001	28 154.72
173	7.841	6.439	27 088.00
174	9.967	4.338	30 441.34
175	9.241	5.068	27 626.86

Table D.17: Pressure drop per unit pipe length, nominal mixture flow rate 15 [GPM]

Test No.	Oil Flow Rate [GPM]	Water Flow Rate [GPM]	$\frac{\Delta P}{\Delta L}$ $[\frac{Pa}{m}]$
176	5.249	9.726	24 743.51
177	6.753	8.253	27 316.16
178	8.247	6.771	30 617.20
179	4.544	10.484	24 147.52
180	7.537	7.491	31 164.29
181	3.772	11.271	23 756.41
182	9.810	5.235	30 567.10
183	9.060	6.017	34 981.28
184	6.077	9.015	26 034.05

Table D.18: Pressure drop per unit pipe length, nominal mixture flow rate 16 [GPM]

Test No.	Oil Flow Rate [GPM]	Water Flow Rate [GPM]	$\frac{\Delta P}{\Delta L}$ $[\frac{Pa}{m}]$
185	6.437	9.553	29 043.63
186	7.982	8.056	34 300.43
187	7.225	8.814	30 647.14
188	9.588	6.458	38 132.21
189	8.856	7.199	35 031.89
190	5.620	10.445	28 291.15

Table D.19: Pressure drop per unit pipe length, nominal mixture flow rate 17 [GPM]

Test No.	Oil Flow Rate [GPM]	Water Flow Rate [GPM]	$\frac{\Delta P}{\Delta L}$ $[\frac{Pa}{m}]$
191	7.638	9.346	34 347.53
192	9.368	7.687	41 071.05
193	8.542	8.531	38 729.94
194	6.848	10.262	32 507.41

Table D.20: Pressure drop per unit pipe length, nominal mixture flow rate 18 [GPM]

Test No.	Oil Flow Rate [GPM]	Water Flow Rate [GPM]	$\frac{\Delta P}{\Delta L}$ $[\frac{Pa}{m}]$
195	9.860	8.144	44 345.64
196	8.171	9.866	38 152.36
197	9.053	9.052	42 970.40

Table D.21: Pressure drop per unit pipe length, nominal mixture flow rate 19 [GPM]

Test No.	Oil Flow Rate [GPM]	Water Flow Rate [GPM]	$\frac{\Delta P}{\Delta L}$ $[\frac{Pa}{m}]$
198	8.586	10.454	41 754.70
199	9.564	9.555	46 703.70

Table D.22: Pressure drop across the safety screen assembly with the safety screen, nominal mixture flow rate 6 [GPM]

Test No.	Oil Flow Rate [GPM]	Water Flow Rate [GPM]	[Pa]
4	3.597	2.363	17 501.34
7	1.809	4.209	15 899.23
8	3.903	2.131	18 490.47
9	2.118	3.926	16 205.77
10	4.227	1.820	19 931.67
11	2.720	3.328	17 213.75
12	3.313	2.737	17 688.90
13	2.404	3.646	16 649.68
14	3.031	3.055	18 267.67

Table D.23: Pressure drop across the safety screen assembly with the safety screen, nominal mixture flow rate 7 [GPM]

Test No.	Oil Flow Rate [GPM]	Water Flow Rate [GPM]	[Pa]
16	2.453	4.554	19 396.77
17	4.899	2.112	23 930.00
18	2.803	4.212	20 129.62
19	1.754	5.267	19 129.32
20	3.872	3.157	22 377.45
21	4.200	2.830	23 047.58
22	4.550	2.481	23 693.44
23	3.501	3.534	21 733.60
24	3.157	3.884	20 900.18
25	5.256	1.786	25 905.47
26	2.086	4.974	19 589.08

Table D.24: Pressure drop across the safety screen assembly with the safety screen, nominal mixture flow rate 8 [GPM]

Test No.	Oil Flow Rate [GPM]	Water Flow Rate [GPM]	[Pa]
27	2.376	5.615	25 290.41
28	3.596	4.399	26 298.60
29	2.785	5.226	25 807.33
30	5.577	2.440	31 763.02
31	5.188	2.831	30 799.33
33	3.228	4.796	26 391.25
37	4.400	3.635	28 812.36
38	4.005	4.035	27 828.13
39	4.807	3.264	30 155.67
45	2.021	6.068	25 884.43
49	6.077	2.082	35 215.09

Table D.25: Pressure drop across the safety screen assembly with the safety screen, nominal mixture flow rate 9 [GPM]

Test No.	Oil Flow Rate [GPM]	Water Flow Rate [GPM]	[Pa]
50	4.045	4.931	32 669.80
51	5.824	3.160	37 349.62
52	3.156	5.837	31 161.96
53	2.233	6.763	30 898.45
55	4.505	4.508	34 017.41
56	4.950	4.079	35 445.99
57	3.593	5.441	31 713.87
58	2.754	6.320	31 855.84
59	6.748	2.335	41 111.38
60	1.854	7.232	31 391.43
61	7.217	1.876	42 918.51
62	5.450	3.644	37 229.96
64	6.394	2.717	39 973.56

Table D.26: Pressure drop across the safety screen assembly with the safety screen, nominal mixture flow rate 10 [GPM]

Test No.	Oil Flow Rate [GPM]	Water Flow Rate [GPM]	[Pa]
65	2.483	7.459	37 883.10
66	3.000	6.983	38 195.15
67	7.977	2.026	52 441.68
68	4.999	5.009	41 811.29
69	3.510	6.505	38 616.23
70	7.491	2.563	49 984.25
71	2.021	8.069	39 056.56
72	6.516	3.575	47 143.16
73	4.521	5.572	41 194.86
74	6.009	4.114	46 257.27
75	5.540	4.586	44 496.05
76	7.020	3.109	48 307.74
77	4.080	6.062	40 155.52

Table D.27: Pressure drop across the safety screen assembly with the safety screen, nominal mixture flow rate 11.2 [GPM]

Test No.	Oil Flow Rate [GPM]	Water Flow Rate [GPM]	[Pa]
78	3.367	7.790	47 363.02
79	2.818	8.348	46 752.12
81	3.931	7.249	48 190.72
82	4.457	6.731	48 771.73
83	1.662	9.530	47 116.97
88	9.493	1.727	65 560.30
89	7.808	3.416	59 058.64
90	6.720	4.514	56 722.41
95	2.260	8.982	47 830.90
96	6.133	5.110	54 707.35
98	7.311	3.941	58 178.10
100	5.085	6.186	51 116.34
103	8.984	2.296	64 376.51
105	8.438	2.894	60 499.71
106	5.641	5.699	52 859.73

Table D.28: Pressure drop across the safety screen assembly with the safety screen, nominal mixture flow rate 12.2 [GPM]

Test No.	Oil Flow Rate [GPM]	Water Flow Rate [GPM]	[Pa]
107	7.323	4.793	64 083.70
108	3.650	8.482	55 570.83
109	3.102	9.040	55 721.59
110	1.820	10.327	56 055.75
112	10.191	1.974	67 464.34
113	5.494	6.678	58 595.57
114	7.912	4.262	60 201.94
117	7.345	4.862	59 798.54
118	4.280	7.929	57 056.05
119	4.899	7.311	57 822.23
120	8.573	3.654	63 475.99
121	6.792	5.443	63 073.82
123	9.159	3.097	66 483.17
125	6.198	6.072	60 348.71
126	2.421	9.852	57 074.22
128	9.793	2.505	69 235.08

Table D.29: Pressure drop across the safety screen assembly with the safety screen, nominal mixture flow rate 13.2 [GPM]

Test No.	Oil Flow Rate [GPM]	Water Flow Rate [GPM]	[Pa]
129	9.228	3.879	81 227.43
131	9.223	3.924	75 018.29
134	5.949	7.246	65 177.50
135	7.258	5.937	70 836.10
136	2.645	10.555	63 798.94
137	4.626	8.578	64 404.94
138	3.301	9.905	64 247.02
139	5.299	7.918	64 953.03
140	3.968	9.250	64 573.61
141	7.923	5.302	73 823.31
147	8.618	4.643	76 476.47
150	9.940	3.342	81 601.45
151	6.662	6.638	68 992.41
153	6.664	6.667	68 738.87

Table D.30: Pressure drop across the safety screen assembly with the safety screen, nominal mixture flow rate 14.2 [GPM]

Test No.	Oil Flow Rate [GPM]	Water Flow Rate [GPM]	[Pa]
157	3.554	10.614	72 994.11
159	5.676	8.507	73 932.64
160	4.275	9.916	73 337.47
164	4.971	9.232	73 908.03
166	6.402	7.816	74 729.19
168	7.816	6.410	80 707.22
169	8.508	5.719	85 037.15
171	7.101	7.162	76 737.45
172	9.278	5.001	89 281.08
174	9.967	4.338	92 297.58

Table D.31: Pressure drop across the safety screen assembly with the safety screen, nominal mixture flow rate 15 [GPM]

Test No.	Oil Flow Rate [GPM]	Water Flow Rate [GPM]	[Pa]
176	5.249	9.726	80 984.12
177	6.753	8.253	82 897.90
178	8.247	6.771	87 270.03
179	4.544	10.484	81 419.39
180	7.537	7.491	85 763.11
181	3.772	11.271	81 894.20
182	9.810	5.235	97 555.58
183	9.060	6.017	93 756.36
184	6.077	9.015	82 147.43

Table D.32: Pressure drop across the safety screen assembly with the safety screen, nominal mixture flow rate 16 [GPM]

Test No.	Oil Flow Rate [GPM]	Water Flow Rate [GPM]	[Pa]
185	6.437	9.553	92 542.13
186	7.982	8.056	95 639.63
187	7.225	8.814	93 362.89
188	9.588	6.458	104 913.80
189	8.856	7.199	98 708.91
190	5.620	10.445	92 694.23

Table D.33: Pressure drop across the safety screen assembly with the safety screen, nominal mixture flow rate 17 [GPM]

Test No.	Oil Flow Rate [GPM]	Water Flow Rate [GPM]	[Pa]
191	7.638	9.346	104 803.52
192	9.368	7.687	111 508.39
193	8.542	8.531	109 262.72
194	6.848	10.262	104 425.86

Table D.34: Pressure drop across the safety screen assembly with the safety screen, nominal mixture flow rate 18 [GPM]

Test No.	Oil Flow Rate [GPM]	Water Flow Rate [GPM]	[Pa]
195	9.860	8.144	121 856.07
196	8.171	9.866	107 636.55
197	9.053	9.052	106 687.21

Table D.35: Pressure drop across the safety screen assembly with the safety screen, nominal mixture flow rate 19 [GPM]

Test No.	Oil Flow Rate [GPM]	Water Flow Rate [GPM]	[Pa]
198	8.586	10.454	119 950.87
199	9.564	9.555	125 764.16

Table D.36: Pressure drop across the safety screen assembly without the safety screen, nominal mixture flow rate 8 [GPM]

Test No.	Oil Flow Rate [GPM]	Water Flow Rate [GPM]	[Pa]
32	6.003	2.017	9 561.24
34	5.601	2.425	9 738.56
36	3.210	4.825	8 536.31
40	2.835	5.236	8 619.80
41	4.437	3.635	9 119.50
42	2.418	5.657	8 840.19
43	5.248	2.831	10 093.19
44	3.620	4.464	8 501.20
46	4.027	4.067	8 119.77
47	4.855	3.249	9 943.42
48	2.073	6.050	9 261.45

Table D.37: Pressure drop across the safety screen assembly without the safety screen, nominal mixture flow rate 11.2 [GPM]

Test No.	Oil Flow Rate [GPM]	Water Flow Rate [GPM]	[Pa]
80	2.218	8.955	17 921.45
84	7.241	3.963	18 780.94
85	5.612	5.596	16 073.21
86	3.903	7.311	17 014.64
87	6.177	5.038	17 784.17
91	6.718	4.517	19 261.86
92	2.801	8.438	17 718.13
93	3.390	7.850	17 348.86
94	4.477	6.765	16 620.04
97	8.982	2.269	16 626.62
99	1.716	9.543	18 310.22
101	7.848	3.426	18 902.04
102	5.075	6.200	16 495.90
104	8.432	2.850	16 192.07

Table D.38: Pressure drop across the safety screen assembly without the safety screen, nominal mixture flow rate 14.2 [GPM]

Test No.	Oil Flow Rate [GPM]	Water Flow Rate [GPM]	[Pa]
156	3.557	10.597	33 219.47
158	4.236	9.942	31 837.21
161	9.904	4.288	26 153.92
162	6.365	7.828	26 248.32
163	5.005	9.192	27 575.24
165	7.132	7.079	26 381.88
167	5.668	8.556	27 107.46
170	8.555	5.698	28 271.22
173	7.841	6.439	26 484.82
175	9.241	5.068	30 931.31